



# SCIENCE & ENGINEERING SYMPOSIUM PROCEEDINGS 16-19 OCTOBER



THEME: "Advanced Technologies — Key to  
Capabilities at Affordable Costs"

**DISTRIBUTION STATEMENT A**  
Approved for Public Release  
Distribution Unlimited

**VOL. I. AVIONICS**

**CO-SPONSORED BY  
NAVAL MATERIAL COMMAND  
AIR FORCE SYSTEMS COMMAND**



- Avionics
- Propulsion
- Flight Dynamics
- Basic Research

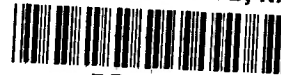
- Material
- Armament
- Human Resources

Reproduced From  
Best Available Copy

19991214 076

TL  
505  
.S45  
1978  
v.1

TECH LIBRARY KAFB, NM



0000893

PROCEEDINGS  
OF THE  
1978 SCIENCE AND ENGINEERING SYMPOSIUM

16 - 19 OCTOBER 1978

NAVAL AMPHIBIOUS BASE  
CORONADO, CALIFORNIA

VOLUME I

APPROVED FOR PUBLIC RELEASE;  
DISTRIBUTION UNLIMITED

U.S. Air Force  
**Air Force Weapons Laboratory**  
Technical Library

## SYMPOSIUM OFFICIALS

### CO-SPONSORS

NAVAL MATERIAL  
COMMAND

AIR FORCE SYSTEMS  
COMMAND

### HOSTS

NAVAL OCEAN SYSTEMS  
CENTER

WEST COAST COORDINATOR

NAVAL AMPHIBIOUS BASE

FACILITIES

### CO-CHAIRMEN

WILLIAM KOVEN  
Associate Technical Director  
Naval Air Research and  
Technology  
Naval Air Systems Command

DR. BERNARD KULP  
Chief Scientist  
Director of Science and  
Technology  
Air Force Systems Command

### DEPUTY CO-CHAIRMEN

JAMES MULQUIN  
Advanced Systems Technology  
Planning  
Naval Air Research and  
Technology  
Naval Air Systems Command

MAJOR LARRY FEHRENBACHER  
Assistant to Chief Scientist  
Director of Science and  
Technology  
Air Force Systems Command

TL  
505  
.S45  
1978  
v. 1

## PREFACE

The initial co-sponsored Air Force Systems Command/Naval Material Command Science and Engineering Symposium was held at the Naval Amphibious Base, Coronado on 16 - 19 October 1978. The theme of the 1978 Symposium was "Advanced Technologies - Key to Capabilities at Affordable Cost."

The objectives of this first joint Navy/Air Force Science and Engineering Symposium were to:

- . Provide a forum for military and civilian laboratory scientific and technical researchers to demonstrate the spectrum and nature of 1978 achievements by their services in the areas of
  - . Armament
  - . Avionics
  - . Basic Research
  - . Flight Dynamics
  - . Human Resources
  - . Materials
  - . Propulsion
- . Recognize outstanding technical achievement in each of these areas and select the outstanding technical paper within the Navy and the Air Force for 1978
- . Assist in placing the future Air Research and Development of both services in correct perspective and to promote the exchange of ideas between the Navy and Air Force Laboratories
- . Stress the need for imagination, vision and overall excellence within the technology community, assuring that the air systems of the future will not only be effective but affordable.

Based upon the success of the initial joint symposium (which was heretofore an Air Force event), future symposia are planned with joint Navy/Air Force participation.



# TABLE OF CONTENTS

## VOLUME I

### AVIONICS

R. S. VAUGHN, NADC

COL R. LOPINA, AFAL

#### CO-CHAIRMEN

The Airborne Electronic Terrain Map System (AETMS) Capt F. Barney, USAF and Dr. L. Tamburino, AFAL	1
The Assessment of GaAs Passivation and Its Applications Dr. F. Schuermeyer, J. Blassingame, AFAL and Dr. H. Hartnagel, Univ. of New Castle-Upon-Thames, England	17
Identification of Impurity Complexes in Gallium Arsenide Device Material by High Resolution Magneto-Photoluminescence G. McCoy, Maj R. Almassy, USAF, D. Reynolds and C. Litton, AFAL	50
Microcircuit Analysis Techniques Using Field-Effect Liquid Crystals D. J. Burns, RADC	69
Surface Acoustic Wave Frequency Synthesizer for JTIDS P. H. Carr, A. J. Budreau and A. J. Slovodnik, RADC	85
Enhanced Measurement Capability Using a Background Suppression Scheme G. A. Vanasse and E. R. Huppi, AFGL	110
Spectrum Estimation and Adaptive Controller for Long-Range Complex Scattering Targets R. F. Ogrodnik, RADC	122
Spatial and Temporal Coding of GaAs Lasers for a Laser Line Scan Sensor Capt R. S. Shinkle, USAF, ASD	149

## VOLUME II

### PROPULSION

#### AERO-PROPULSION

A. A. MARTINO, NAPC

COL G. STRAND, AFAPL

#### CO-CHAIRMEN

## ROCKET PROPULSION

B. W. HAYES, NWC

COL W. F. MORRIS, AFRPL

CO-CHAIRMEN

Airbreathing Propulsion Functional Area Review Col G. E. Strand, USAF, AFAPL	164
Rocket Propulsion Overview Col W. F. Morris, USAF, AFRPL	196
Role of Turbine Engine Technology on Life Cycle Cost R. F. Panella and R. G. McNally, AFAPL	212
VORBIX Augmentation - An Improved Performance Afterburner for Turbo Fan Engines W. W. Wagner, NAPC	247
A Retirement for Cause Study of an Engine Turbine Disk R. Hill, AFAPL, R. Reimann, AFML and L. Ogg, ASD	265
Payoffs of Variable Cycle Engines for Supersonic VSTOL Aircraft R. T. Lazarick and P. F. Piscopo, NAPC	296
The Coanda/Refraction Concept for Gasturbine Engine Exhaust Noise Suppression During Ground Testing D. Croce, NAEC	322
Expendable Design Concept Lt D. C. Hall, USAF, AFAPL and H. F. Due, Teledyne CAE	349
The Supersonic Expendable Turbine Engine Development Program T. E. Elsasser, NAPC	363
Unique Approach for Reducing Two Phase Flow Losses in Solid Rocket Motors Lt D. C. Ferguson, USAF, AFRPL	383
Missile System Propulsion Cook-Off R. F. Vetter, NWC	414
A Powerful New Tool for Solid Rocket Motor Design W. S. Woltoz, AFRPL	428
Quantification of the Thermal Environment for Air-Launched Weapons H. C. Schafer, NWC	453

A Study of Rocket-Propelled Stand-Off Missiles 470  
Lt L. K. Slimak, USAF, AFRPL

Prediction of Rocket Motor Exhaust Plume Effects on Missile Effectiveness 496  
A. C. Victor, NWC

## VOLUME III

### FLIGHT DYNAMICS

C. A. DeCRESCENTE, NADC COL G. CUDAHY, USAF, AFFDL  
CO-CHAIRMEN

Air Force Flight Dynamics Functional Area Review 521  
Col G. F. Cudahy, USAF, AFFDL

A Functional Area Review (FAR) of Navy Flight Dynamics 592  
C. A. DeCrescente, NADC

Aircraft Aft-Fuselage Sonic Damping 615  
G. Pigman, E. Roeser and M. Devine, NADC

Active Control Applications to Wing/Store Flutter Suppression 626  
L. J. Hutsell, T. E. Noll and D. E. Cooley, AFFDL

Maximum Performance Escape System (MPES) 657  
J. J. Tyburski, NADC and W. J. Stone, NWC

Status of Circulation Control Rotor and X-Wing VTOL Advanced Development Program 673  
T. M. Clancy, D. G. Kirkpatrick and R. M. Williams, DTNSRDC

AFFTC Parameter Identification Experience 697  
Lt D. P. Maunder, USAF, AFFTC

Developments in Flight Dynamics Technology for Navy V/STOL Aircraft 719  
J. W. Clark, Jr., and C. Henderson, NADC

Cost Effective Thrust Drag Accounting 750  
R. B. Sorrells, III, AEDC

Drag Prediction for Wing-Body-Nacelle Configurations 766  
T. C. Tai, DTNSRDC

Numerical Solution of the Supersonic and Hypersonic Viscous Flow Around Thin Delta Wings 793  
Maj G. S. Bluford, USAF and Dr. W. L. Hankey, AFFDL

Optimization of Airframe Structures: A Review and Some  
Recommendations 828  
V. B. Venkayya, AFFDL

Use of Full Mission Simulation for Aircraft Systems Evaluation 870  
K. A. Adams, AFFDL

## VOLUME IV

### BASIC RESEARCH

DR. E. H. WEINBERG, NAL DR. L. KRAVITZ, AFOSR  
CO-CHAIRMEN

The Electronic and Electro-Optic Future of III-V Semiconductor  
Compounds 885  
H. L. Lessoff, NRL and J. K. Kennedy, RADC

Collective Ion Acceleration and Intense Electron Beam Propagation 912  
Within an Evacuated Dielectric Tube  
Capt R. L. Gullickson, USAF, AFOSR, R. K. Parker and J. A.  
Pasour, NRL

High Spatial Resolution Optical Observations Through the 939  
Earth's Atmosphere  
Capt S. P. Worden, USAF, AFGL

High Burnout Schottky Barrier Mixer Diodes for X-Band and 954  
Millimeter Frequencies  
A. Christou, NRL

New Energetic Plasticizers: Synthesis, Characterization and 968  
Potential Applications  
Lt R. A. Hildreth, USAF, Lt S. L. Clift, USAF and Lt J. P.  
Smith, FJSRL

Improved Corrosion and Mechanical Behavior of Alloys by Means 981  
of Ion Implantation  
J. K. Hirvonen and J. Butler, NRL

Symmetric Body Vortex Wake Characteristics in Supersonic Flow 1000  
Dr. W. L. Oberkampf, Univ of Texas at Austin and Dr. D. C.  
Daniel, AFATL

Materials Effects in High Reflectance Coatings 1033  
H. E. Bennett, NWC

Improved Substrate Materials for Surface Acoustic Wave (SAW) Devices Capt R. M. O'Connell, USAF, RADC	1058
A Simple Prediction Method for Viscous Drag and Heating Rates T. F. Zien, NSWC	1075
Assessing the Impact of Air Force Operations on the Stratosphere Composition C. C. Gallagher and Capt R. V. Pieri, USAF, AFGL	1110
On the Modelling of Turbulence Near a Solid Wall K. Y. Chien, NSWC	1131
Atmospheric Electric Hazards to Aircraft L. H. Ruhnke, NRL	1146
Efficient Operation of a 100 Watt Transverse Flow Oxygen-Iodine Chemical Laser Maj W. E. McDermott, USAF, Capt N. R. Pchelkin, USAF, Dr. J. Bernard and Maj R. R. Bousek, USAF, AFWL	1161

## VOLUME V

### MATERIALS

F. S. WILLIAMS, NADC	COL P. O. BOUCHARD, USAF, AFML
CO-CHAIRMEN	
Advanced Materials Technologies - The Key to New Capabilities at Affordable Costs Col P. O. Bouchard, USAF, AFML	1173
Ceramics in Rolling Element Bearings C. F. Bersch, NAVAIR	1182
Group Technology Key to Manufacturing Process Integration Capt D. Shunk, USAF, AFML	1198
An Attempt to Predict the Effect of Moisture on Carbon Fiber Composites J. M. Augl, NSWC	1213
Evaluation of Spectrometric Oil Analysis Techniques for Jet Engine Condition Monitoring Lt T. J. Thomson, USAF and K. J. Eisentraut, AFML	1252

Characterization of Structural Polymers, Using Nuclear Magnetic Resonance Techniques W. B. Moniz, C. F. Poranski, Jr., A. N. Garroway and H. A. Resing, NRL	1287
On the Variation of Fatigue Crack Opening Load with Measurement Location D. E. Macha, D. M. Corbly, J. W. Jones, AFML	1308
Environmentally Induced Catastrophic Damage Phenomena and Control Dr. J. L. DeLuccia, NADC	1335
Improved High Temperature Capability of Titanium Alloys by Ion Implantation/Plating S. Fujishiro, AFML and E. Eylon, Univ of Cincinnati	1366
Measurement of the Physical Properties and Recombination Process in Bulk Silicon Materials Lt T. C. Chandler, USAF, AFML	1384
Deuterated Synthetic Hydrocarbon Lubricant A. A. Corte, NADC	1396
The Cordell Plot: Key to a Better Understanding of the Behavior of Fiber-Reinforced Composites T. M. Cordell, AFML	1410

## VOLUME VI

### ARMAMENT

DR. J. MAYERSAK, AFATL	R. M. HILLYER, NWC
CO-CHAIRMEN	
Armament Technology - Functional Overview Dr. J. R. Mayersak, AFATL	1434
The Digital Integrating Subsystem-Modularity, Flexibility and Standardization of Hardware and Software D. L. Gardner, AFATL	1449
Bank-To-Turn (BTT) Technology R. M. McGehee, AFATL	1490
Advances in Microwave Striplines with Applications J. A. Mosko, NWC	1507

Considerations for the Design of Microwave Solid-State Transmitters M. Afendykiew, Jon Bumgardner and Darry Kinman, NWC	1543
Strapdown Seeker Guidance for Air-to-Surface Tactical Weapons Capt T. R. Callen, USAF, AFATL	1590
Optimizing the Performance of Antennas Mounted on Complex Airframes Dr. C. L. Yu, NWC	1614

## VOLUME VII

### HUMAN RESOURCES

H. J. CLARK, AFHRL	DR. J. HARVEY, NTEC	
CO-CHAIRMEN		
Human Resources Research and Development H. J. Clark, AFHRL		1640
Human Resources in Naval Aviation Dr. J. Harvey, NTEC		1649
LCCIM: A Model for Analyzing the Impact of Design on Weapon System Support Requirements and LCC H. A. Baran, AFHRL, A. J. Czuchry and J. C. Goclowski, Dynamics Research Corp		1683
Pacts: Use of Individualized Automated Training Technology Dr. R. Breaux, NTEC		1703
Increasing the Affordability of I-Level Maintenance Training Through Simulation G. G. Miller, D. R. Baum and D. I. Downing, AFHRL		1711
Psychomotor/Perceptual Measures for the Selection of Pilot Trainees D. R. Hunter, AFHRL		1741
Modern Maintenance Training Technology and Our National Defense Posture Dr. W. J. King and Dr. P. E. Van Hemel, NTEC		1758
Prediction of System Performance and Cost Effectiveness Using Human Operator Modelling LCDR N. E. Lane, USN, W. Leyland, NADC and H. I. Strieb (Analytics)		1781

An Inflight Physiological Data Acquisition and Analysis System Capt J. T. Merrifield, USAF, T. P. Waddell, D. G. Powell, USAF/SAM and E. B. Croson, PMTC	1804
Synthetic Selection of Naval Aviators: A Novel Approach D. E. Norman, D. Wightman, NTEC and CDR L. Waldeisen, NAMRL	1821
Modeling: The Air Force Manpower and Personnel System for Policy Analysis Capt S. B. Polk, USAF, AFHRL	1831
Evoked Brain Potentials as Predictors of Performance: The Hemispheric Assymetry as Related to Pilot and Radar Intercept Officer Performance Dr. B. Rimland and Dr. G. W. Lewis, NPRDC	1841
Launch Opportunity for Air-to-Ground Visually Delivered Weapons R. A. Erickson and C. J. Burge, NWC	1863



## VOLUME VIII

### AVIONICS, PROPULSION, AND FLIGHT DYNAMICS (CLASSIFIED)

Functional Area Review of Avionics Col R. F. Lopina, USAF, AFAL	1
The MADAIR System J. A. Titus, NCSC	27
Electronically Agile Array for Long-Range Airborne Surveillance Radar Dr. J. K. Smith, NADC	89
Automatic Ship Classification System W. G. Hueber and Dr. L. A. Wilson, NWC	118
Reduction of False Alarm Rates in Aircraft Attack Warning Systems H. L. Jaeger, NWC	144
Impact of Focal Plane Array Technology on Airborne Forward Looking Infrared Sensors M. Hess and S. Campana, NADC	179
Advanced Sonobuoy Technology - ERAPS (Expendable Reliable Acoustic Path Sonobuoy) J. J. Stephenosky, NADC	200
NAVSTAR Global Positioning System Field Test Results Aboard Air Force and Navy Test Vehicles LCDR J. A. Strada, USN, SAMSO	220
An Overview of Soviet Propulsion Capabilities W. A. Zwart, FTD	240
Reduced Observables - An Approach for Providing More Effective and Affordable Combat Weapon Systems D. E. Fraga, AFFDL	273
Soviet Method of Calculating the Aerodynamic Characteristics of Wings Flying in Ground Effect Lt C. R. Gallaway, USAF, FTD	330

## VOLUME IX

### MATERIALS, ARMAMENT, AND HUMAN RESOURCES (CLASSIFIED)

Soviet Materials for Aircraft Engines R. F. Frontani, FTD	362
CCD Camera/Tracker Seeker Technology G. F. Teate, NWC	390
Warhead Designs for Wide Area Antiarmor Cluster Munitions Dr. J. C. Foster and Capt E. M. Cutler, USAF, AFATL	404
Active Moving Target Tracking Seeker Captive Flight Test A. N. DiSalvio, AFATL	427
Inter-Laboratory Air-to-Air Missile Technology - An Innovative Approach T. C. Aden, AFATL	449
Aimable Ordnance for Tactical Anti-Air and Anti-Surface Missiles T. R. Zulkoski and P. H. Amundson, NWC	485
Manned Threat Quantification Capt G. J. Valentino, USAF and Lt R. B. Kaplan, USAF, AMRL	549

THE AIRBORNE ELECTRONIC TERRAIN MAP SYSTEM (AETMS)

BY

LOUIS A. TAMBURINO, Ph.D.

FREDERICK G. BARNEY, CAPTAIN, USAF

System Avionics Division

Air Force Avionics Laboratory  
Air Force Wright Aeronautical Laboratories  
Air Force Systems Command  
Wright-Patterson Air Force Base, Ohio 45433

## A B S T R A C T

The Airborne Electronic Terrain Map System (AETMS) is a compact, low cost system capable of generating real-time displays. It couples directly to the aircraft's navigational computer and, in effect, automates the map reading process. It uses state-of-the-art components and Defense Mapping Agency data bases. The system architecture is quite general and can be adapted for different applications; its core elements can be easily shared in different user configurations.

The United States Air Force Avionics Laboratory (AFAL) has a program to develop a brassboard prototype of this system. The feasibility of the AETMS has already been partially established by simulation of the architecture on a general purpose computer at AFAL. This simulation has been extended to display terrain information in near-real-time on a CRT linked to the computer. The displays are generated from stored polynomial terrain models developed at the United States Army Engineer Topographic Laboratory.

The flexibility of electronic terrain maps, compared to paper and film maps, lends itself to many Air Force applications. Low-level terrain displays are the most obvious, while others include prediction of terrain problems beyond the immediate horizon, new methods of obtaining navigational fixes at low altitudes, and terrain navigational systems not constrained to fixed flight profiles.

## Introduction

The USAF Avionics Laboratory (AFAL) is currently developing an Airborne Electronic Terrain Map System (AETMS). This effort was originally motivated by the desire to reduce map reading chores during low level missions in single seat aircraft (Figure 1). In this highly dynamic environment, the task of correlating navigational data with paper maps in order to visualize terrain is more difficult than usual. This paper briefly describes the approaches, results, and status of our efforts toward automating the map reading process for pilots. (Reference 1 gives a more comprehensive discussion of AETMS.)

Our primary goal is to develop a black box which will contain a large area map along with specialized hardware and software for accessing the terrain data in real-time. Ground-based computers can fulfill this function, but no such system exists with the size, speed, and flexibility required for economical employment in the airborne environment.

Our second goal is to develop an airborne display system which will generate dynamic terrain displays using output data from the electronic map. Even though the electronic map can be used to generate a great variety of displays, the airborne display generator must, in order to keep complexity at a minimum, use simple algorithms to address the problem of real-time conversion of streams of elevation data into display signals. The results should not be expected to achieve state of the art realism in computer generated imagery; however, computer simulation tests have produced some remarkably good terrain displays with the fast, simple algorithms suitable for airborne systems.

## Terrain Modeling

The standard level 1 digitized terrain data base developed by the Defense Mapping Agency (DMA) is available and adequate for an airborne map system. The standard format is 600 elevation values, each comprised of 16 bits, to represent approximately one square mile (9600 bits per square mile). It is readily apparent that large areas require huge amounts of data. Attempts to reduce this amount by thinning out the matrix of elevation values result in increased errors.

As an alternate approach, elevation values are not stored directly; instead, locally valid analytic surface models, polynomials, are used. The polynomial modeling techniques developed at the Army Engineer Topographic Laboratories (ETL) use smoothly joining surface functions which reduce the DMA data without reducing data accuracy (Reference 2). In this approach, polynomial co-efficients are stored in a digital memory and these can then be used to compute the elevation of any point.

Imagine a two-dimensional coordinate grid covering a map surface and sectioning the surface into patches of approximately 0.2 by 0.2 miles. In other words, each square mile is covered by a set of 25 patches. The corners of these patches (or the intersections of grid lines) are called nodes. In the polynomial models, a set of co-efficients is associated with each node and characterizes a bivariate polynomial centered at the node. This bivariate polynomial has a domain of validity over the four adjacent patches having the node as a common corner.

Given a desired sample position within a patch, the data at its four nodes must be weighted. These weights are functions of the relative position (patch coordinates) of the sample with respect to each of the four nodes. The advantage in data reduction of using polynomials is paid for by an increase in computational complexity. For discrete values, the weighted average is equivalent to a bilinear interpolation. With polynomials, each of the four nodal polynomials must be evaluated at the sample point and then averaged to yield a valid elevation value.

Current working estimates for the airborne data base are:

- 25 patches per square mile.

- 34 bits per set of four polynomial co-efficients (a, b, c, d), where the bivariate polynomials have the form  $a + bx + cy + dxy$ .

- 6 bits per patch to encode cultural features.

This is equivalent to 1,000 bits per square mile, including cultural data. This is large, but significantly smaller than the standard density of 9,600 bits per square mile for encoding elevation data only. On-going studies at ETL suggest that even further reductions may be possible. DMA, ETL, and AFAL are cooperating in further improvements to the airborne data base.

#### Electronic Map Implementation

Memory technology provides a choice of high density memory packages in which to store the data base. Storage of a very large; i.e., global, terrain map may even require a combination of memories, such as a magnetic bubble memory backed up with archival data on magnetic tape. Bubble memory is particularly attractive because it is relatively inexpensive, rugged, and non-volatile. Current 16 megabit prototype packages, developed for AFAL by Texas Instruments, have storage capacity for a regional map of 16,384 square miles. Magnetic tape could be used to periodically update such a bubble memory. Programs are under way to significantly increase the packing density of the bubble memory in the early 1980's.

The airborne system is designed to achieve a sampling rate of one million elevation samples per second. This rate should be adequate for most real-time applications. Achievement of this rate in a compact, low cost, airborne system operating in a dynamic environment, however, presents several major difficulties.

To sample every microsecond, four polynomials need to be computed and averaged every microsecond. This is achievable only with a customized parallel processor known as a polynomial generator. The major problem here is the reconciliation of the slow access times inherent in mass memories with very fast parallel data transfer and processing (Figure 2). Block access time into bubble memories is one or two milliseconds, which is reasonably good time for mass memories, but too slow to drive the polynomial generator.

We can speedily access data, however, if it is temporarily stored in a dual port fast memory buffer with a parallel output data channel. This fast memory buffer acts as a dynamic window for the global model in mass memory and contains all relevant patch data in the immediate vicinity of the moving aircraft.

The design of this dynamic buffer involves the reconciliation of opposing goals and requirements; namely, (1) providing sufficient agility to enable the buffer to adapt and respond to signals describing curvilinear trajectories, (2) minimizing I/O interference between the updating and accessing processes, (3) keeping the buffer capacity within the minimum necessary to insure the containment of a preselected usable window area. Knowing the characteristics of trajectory dynamics, one can always select a buffer memory of sufficient size to insure fulfillment of (1) and (2).

To avoid significant and undesirable pauses (or down times) in data accessing, some excess buffer capacity is always required in a dynamic buffer. As an extreme measure, the buffer size can approach the size of the mass memory. The fast buffer memory system designed at AFAL represents a significant breakthrough for the airborne map and display system in Figure 3. The buffer's capacity can be minimized with respect to any given window size. In addition, it can be economically constructed with off-the-shelf components and with ordinary fabrication and packaging techniques.

The minicomputer executive depicted in Figure 3 is generally responsible for low frequency chores, such as external input to the mass memory, interaction with the navigational computer, tracking the dynamic window, and initializing the update and scan controllers. Once initialized, the update controller is responsible for refreshing the buffer memory due to shifts in the window position.

Each scan pattern generated by the electronic map consists of samples taken along a set of line segments which are specified by the mini-computer. The scan controller determines map coordinates for each sample, the buffer address, local patch coordinates, and weights for each node. For each sample point, it initiates transfer of buffered data over a parallel data channel directly to the parallel processor and also sends the patch coordinates and weights over separate data channels. Data at four neighboring nodes are sequentially accessed and processed in order to reduce the number of processing elements and size of data channels. (Presently, additional circuitry to generate samples along non-linear segments is not justified by any known requirements.)

Both the update controller and scan controller have special electronic circuits to perform their respective functions automatically, which greatly eliminates data management problems. Together, they handle the high frequency calculations for the system. The memory control system has been carefully integrated so that both controllers share continual access to the fast buffer memory and the scan controller can access all data at a grid node with a single buffer address.

The polynomial generator architecture, also designed at AFAL, can accept all data into its first level of processing elements and compute weighted averages in pipeline fashion. A stream of elevation values can be directed to various application modules, such as the display generator shown in Figure 3.

To achieve a one megahertz throughput rate, memory cycle and parallel multiply times of 250 nanoseconds are required. With faster components, throughput rates increase proportionally.

### Displays

Figure 4 illustrates two typical sampling patterns for display purposes. Sample spacing,  $\Delta\rho$ , need not be uniform as depicted in the diagrams. Position, orientation ( $\alpha_{nav}$ ), or type of pattern makes little difference to the data management techniques employed in the memory control system. In other words, the time necessary for completing a scanning pattern is proportional to the number of samples in the pattern.

Either the radial or the parallel scan format can be used to generate a moving contour display in which brightness or color varies with surface elevation (Figure 5). This contour display can be compared with sensor data and used to fill in the radar shadows. It enables the pilot to look ahead, "see" behind hills, and plan his maneuvers. Naturally, one can combine other information with this display, such as navigation and target cueing information.



The radial scan pattern has been used to generate perspective displays, which are more graphic than the contour display and also more difficult to generate in real-time. A simple masking algorithm can determine, by comparing successive samples along a radial, whether or not a sampled position is masked by intervening terrain. It can also flag points just on the verge of being masked. These points are used to depict the ridge lines in the upper diagram in Figure 6. This austere format is suitable for a heads-up display. Ridge lines above the airplane symbol are above the aircraft's altitude. In the bottom format, sky shading and visible range lines (contouring) provide additional information about the surface.

The dynamic contour and perspective formats are typical of the displays which have been explored at AFAL with computer simulations. Currently, software is successfully simulating some of the buffer management techniques intended for the airborne system on a general purpose PDP 11/45. This software enables us to continually access a DMA data base stored on a magnetic disk and generate near real-time dynamic displays whose altitude and heading are controlled interactively with a joy stick. With the current system configuration, the PDP 11/45 is computing display symbology at a faster rate than can be transmitted over the data channel to a RAMTEC 9300 display refresh memory. Plans are under way to improve our throughput processing rate with a specialized refresh memory system directly coupled to a peripheral MAP 200 Array Processor.

The airborne display generator will implement in hardware the real-time algorithms being developed at AFAL. Its design will be finalized after interactive (hands-on) simulation experiments, human factors analysis, and flight testing. The exploration of optimal display formats is being pursued in cooperation with ETL and the Air Force Aerospace Medical Research Laboratory.

DMA is providing a digital model of the moving terrain belt system being added to the avionics simulation complex at the Air Force Avionics Laboratory's System Avionics Division. This will provide a unique facility for testing pilot reactions to various display formats in a realistic cockpit simulator.

A major program is under way to design and build a brassboard prototype of the airborne system within the next two or three years. This will be evaluated at AFAL and then undergo limited flight testing.

### Conclusion

We have presented a brief survey of a versatile and economical Airborne Electronic Terrain Map System whose high speed omnidirectional sampling capability can support many different applications. Some

applications depend solely on navigational computer outputs, independent of externally radiating sensors aboard the aircraft, while others can combine or correlate information from onboard sensors such as radar with the terrain map information.

The use of the electronic map in two types of terrain avoidance displays, contour and true perspective, has been described. The true perspective display will give a pilot an immediate visual picture of the ground. True perspective plus additional flight symbology on a heads-up display would be a valuable aid in conditions of restricted visibility, especially in the absence of radar. The system can allow the pilot to disengage the navigational computer and input his choice of state vectors interactively; i.e., fly the display. The ability to preview a dynamic picture of the terrain, along with target cueing symbology, would be useful in planning low-level strikes called while in the air.

Improved synergistic systems combining the unique features of the electronic terrain map with various avionics sensors are foreseeable. This is particularly true in low-level environments where much of the terrain may be above the flight plane. An obvious, but useful, example is the combination of terrain avoidance radar with the contour display which could provide the missing information in areas of radar shadow. Terrain map data plus radar altimeter could provide improved algorithms for terrain following and contour navigation systems which are not constrained to pre-established ground tracks. Techniques for generating true perspective could be used to predict approximate radar images. These predicted images plus actual radar images plus pattern recognition techniques may enable radar navigational fixes to be automated.

What is applicable to piloted aircraft also applies to ground-based systems. RPV's can be adversely affected by poor visibility or loss of their video communication channels. The electronic terrain map can be used in the ways described above to enhance RPV control and guidance while providing a ready back-up for the video link. In flight simulators, the electronic map can help reduce the equipment cost of generating terrain displays. Exploration of these and other applications has been initiated.

In terms of circuit simplicity, speed, and cost, the AETMS achieves near-optimal efficiency. Although discussion has focused on avionics applications, many other systems can profitably utilize the technology described herein.

## REFERENCES

1. Tamburino, Louis A., "Airborne Electronic Terrain Map and Display System," Final Technical Report AFAL-TR-77-232, for Air Force Avionics Laboratory, Wright-Patterson Air Force Base, Ohio, PE-62204F, AFAL 2003-06-35, December 1977, 36 pages.
2. Jancaitus, James R., and Junkins, J. L., "Mathematical Techniques for Automated Cartography," Final Technical Report ETL-CR-73-4, for the United States Army Engineer Topographic Laboratories, Fort Belvoir, Virginia, on Contract DAAK02-72-C-0256, February 1973, 108 pages.

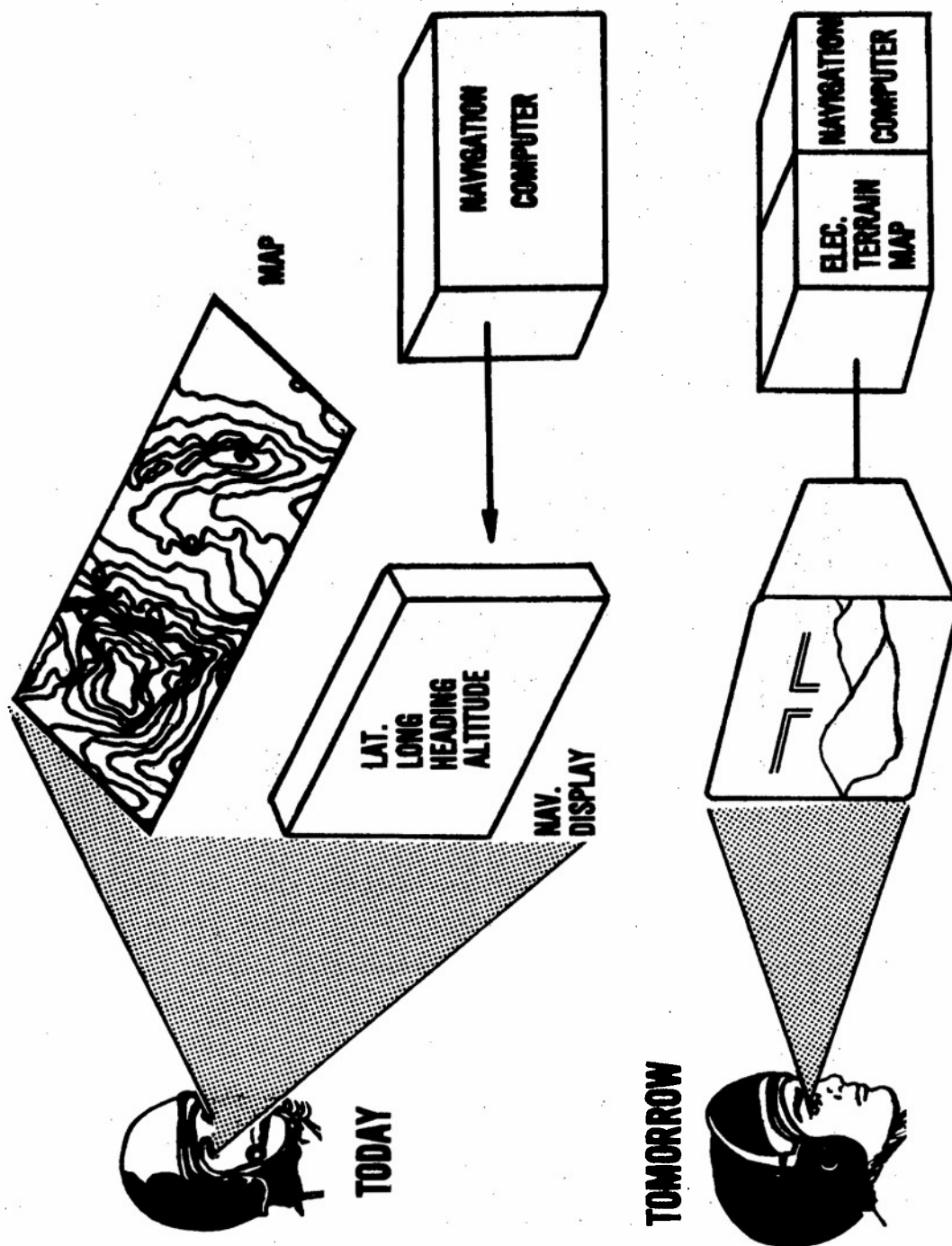
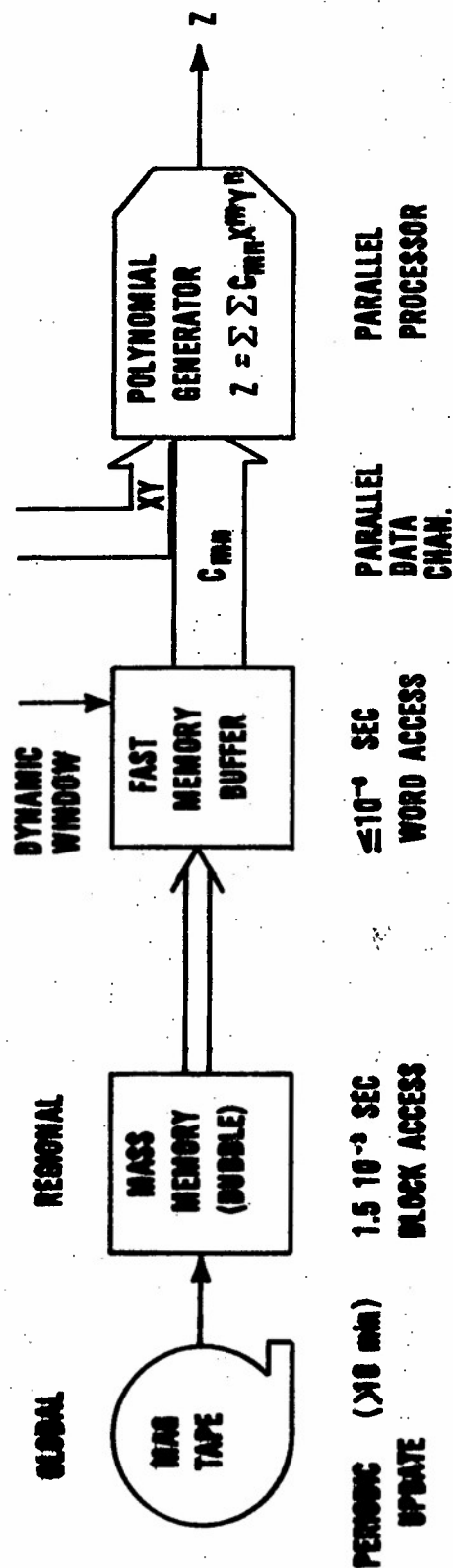


Figure 1. Automating the Map Reading Process

# MEMORY HIERARCHY AND DATA FLOW



GOAL: ONE MILLION ELEV. VALUES (Z) PER SECOND

Figure 2. Memory Hierarchy and Data Flow

# AIRBORNE TERRAIN MAP AND DISPLAY SYSTEM

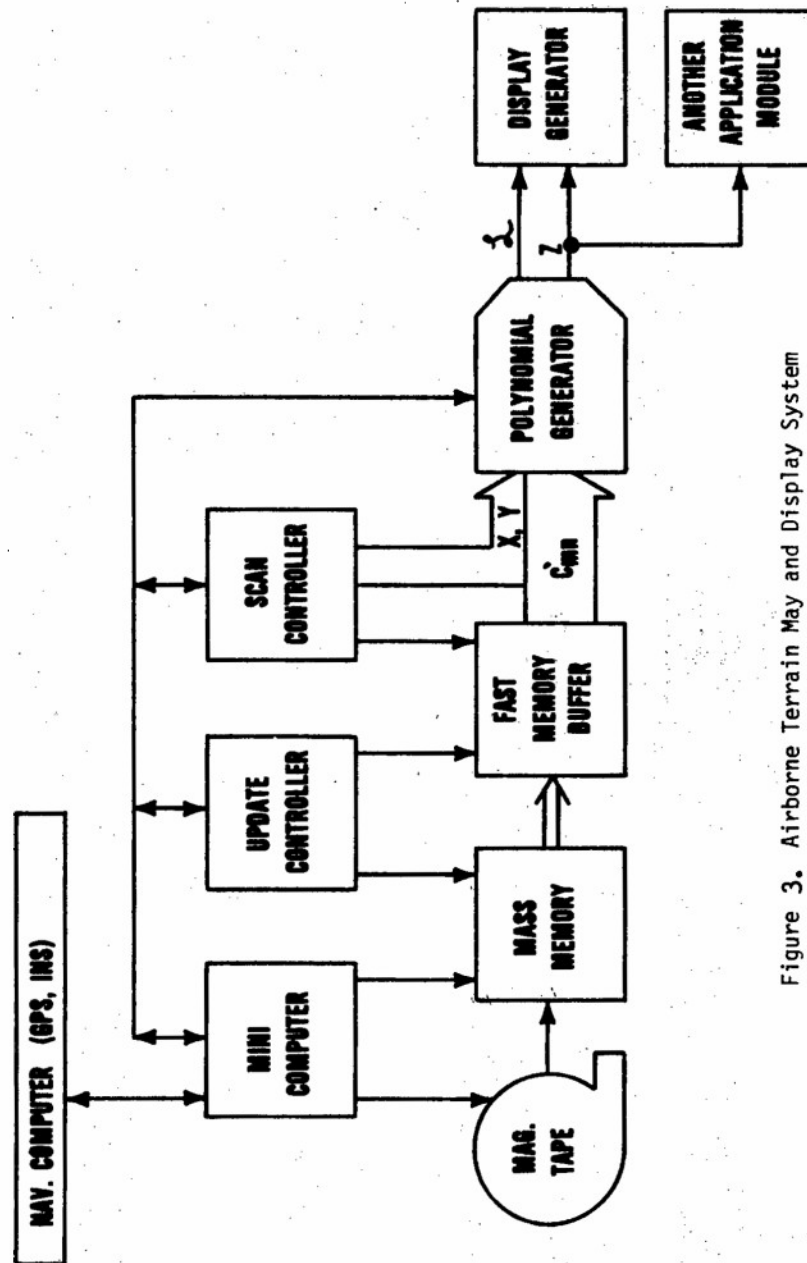


Figure 3. Airborne Terrain Map and Display System

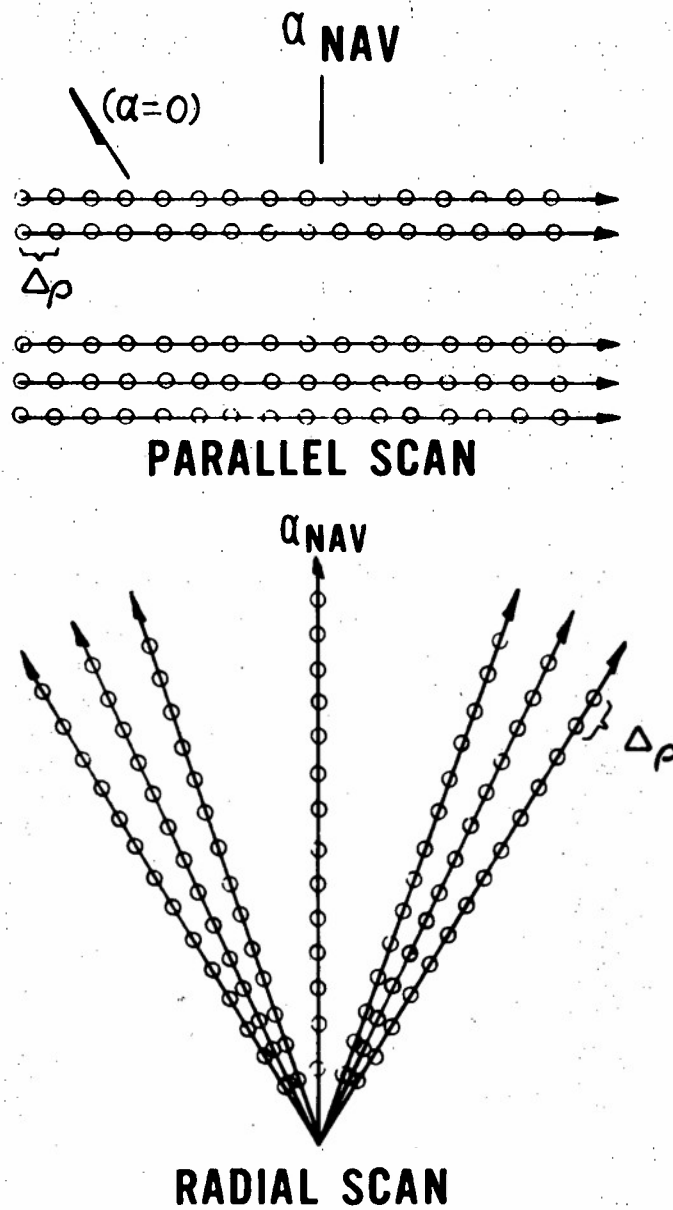
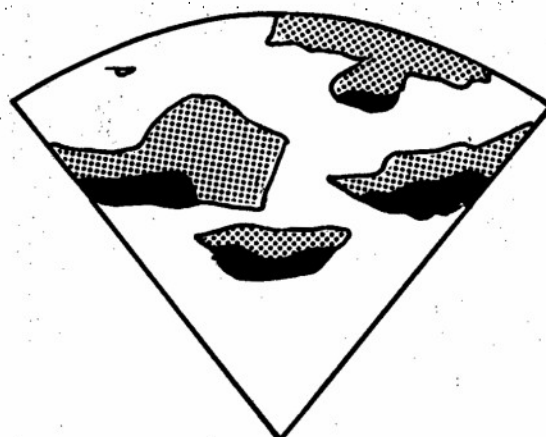
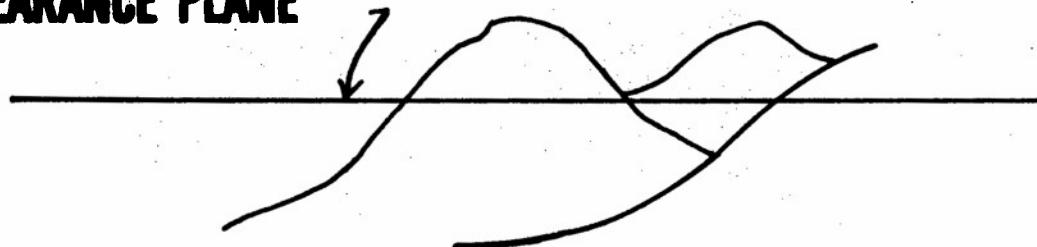


Figure 4. Sampling Patterns

# MOVING CONTOUR TERRAIN AVOIDANCE

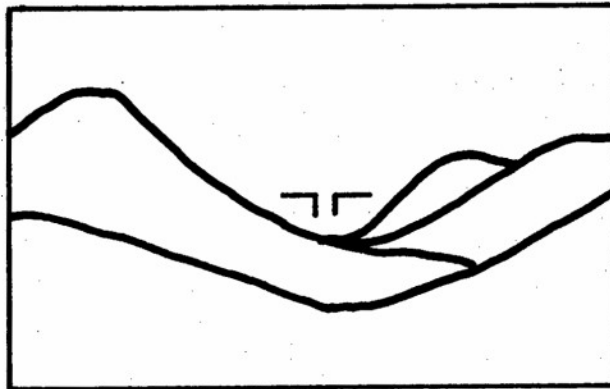
**CLEARANCE PLANE**



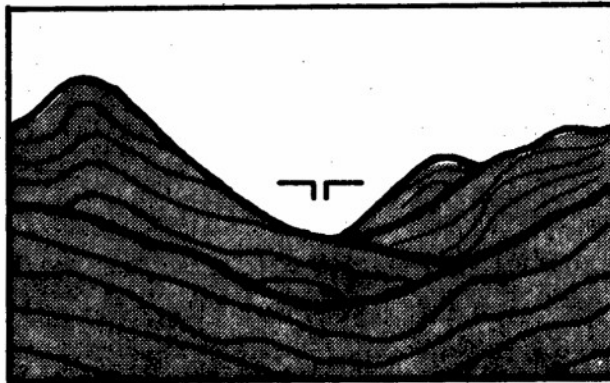
**RADAR RETURNS FROM TERRAIN ABOVE CLEARANCE PLANE** ■ (R)  
**TERRAIN ABOVE CLEARANCE PLANE IN RADAR SHADOW** ▨ (S)  
**ELECTRONIC TERRAIN MAP WILL DISPLAY (R) AND (S)**

Figure 5. Moving Contour Terrain Avoidance Display





11a.



11b.

Figure 6. True-Perspective Graphics

## B I O G R A P H I C A L   S K E T C H E S

Dr. Louis A. Tamburino received his B.S. from Carnegie-Mellon Institute of Technology, 1957, and a Ph.D. in physics from the University of Pittsburgh, 1962. In 1962 - 1963, as a first lieutenant, he was stationed at the United States Army Electronic Proving Grounds, Arizona, where he evaluated navigational systems. His early work at the University of Pittsburgh, Syracuse University (Post-Doctoral Associate, 1963 - 1964), and at the Aerospace Research Laboratories, Wright-Patterson Air Force Base (1964 - 1972) was concerned with gravitational field theory. This led to some new and exact solutions to the Einstein field equations, and a new version of the initial-value problem with novel invariant definitions of energy and momentum. While at Aerospace Research Laboratories, he also worked on computer models for finite plasmas, the inverse optical scattering problem relating intensity to unknown spacecraft geometries, and tactical prediction techniques for air-to-air combat.

Since joining the System Avionics Division of the Air Force Avionics Laboratory, Wright-Patterson Air Force Base, in 1972, Dr. Tamburino has worked in the areas of image processing and integrated avionics display studies. His image processing work involved evaluating and developing adaptive video-bandwidth reduction techniques for future RPV systems. Since 1976, his primary interests have been directed toward the development of an Airborne Electronic Terrain Map System capable of generating real-time displays for the pilot.

Dr. Tamburino belongs to the American Physical Society, Sigma Xi, the Association for Computing Machinery, and IEEE. He holds a Commercial Pilot license.

He is married to the former Linda Sue Quinlivan. They have one daughter, Linda Athena, and reside in Kettering, Ohio.

Frederick Graham Barney was born on 28 March 1947, in Chicago, Illinois. He graduated from Arlington Heights High School in 1965 and attended Colorado State University, where he received a Bachelor of Science in Biological Science in 1969. He then received a commission in the United States Air Force and entered active duty in July 1969. In 1974, he entered the Air Force Institute of Technology and graduated with a Master of Science Degree in Electrical Engineering in 1976. Since his arrival at the Air Force Avionics Laboratory, he has worked on the development of the Electronic Terrain Map System Computer Simulation. He is a member of Eta Kappa Nu, Tau Beta Pi, and the IEEE. He is married to the former Betty Lee Berger. They have two children, John David and Karen Louise, and reside in Dayton, Ohio.

(U) ASSESSMENT OF GaAs PASSIVATION AND ITS APPLICATIONS

BY

Fritz L. Schuermeyer

Hans L. Hartnagel

John M. Blasingame

Electronic Technology Division  
Air Force Avionics Laboratory  
Wright-Patterson AFB, Ohio

(U) ASSESSMENT OF GaAs PASSIVATION AND ITS APPLICATIONS

Abstract

Within the Air Force, there is a need for a digital processing capability requiring clock rates greatly exceeding those possible with even the most advanced silicon technology. Projected 1980 to 1985 requirements for electronic warfare, telemetry and digital communications cover the 1 to 10 GHz clock frequency range. Progress is being made in fabricating GaAs MESFETs for analog applications and in developing GaAs digital MESFET integrated circuits.

One area of great importance to this technology is in passivating the surface of the GaAs structure in order to: (a) mechanically and chemically protect the device, (b) electrically control generation and recombination of charge carriers at the surface, and (c) improve the breakdown voltage and the leakage current of diodes. Whereas in the silicon technology,  $\text{SiO}_2$  provides an excellent passivation layer, no adequate passivation layer exists presently for GaAs devices. Consequently, surface passivation of GaAs is an area of active research.

AFAL has been working in-house on GaAs passivation using wet anodized films. These films are being investigated chemically with Auger and ESCA techniques. Electrical measurements are performed to evaluate capacitance-voltage characteristics. A transient photo-charge measurement technique was developed to evaluate band bending at the semiconductor surface and to determine the oxide capacitance. These measurements also allow quantitative determination of charge injection into the insulator.

A major effort will be devoted to the application of this passivation technology to active GaAs devices, especially to GaAs MESFETs.

## I. INTRODUCTION:

Today's military electronic systems use Si integrated circuits as the predominate active component due to the advanced status of development of this technology. However, the speed and the frequency of operation of these devices is limited (Figure 1). There exist many applications within Air Force systems, where higher speed or higher frequency of operation of electronic circuits would significantly improve the performance of those systems (Figure 2). One example is: radar signal processing, where higher resolution is proportional to processing speed. Consequently, DOD and especially AFAL are developing GaAs technology for high speed applications.

GaAs is a semiconductor much like silicon. However, the electron mobility of GaAs is approximately 5000 and whereas Si is only 1000  $\text{cm}^2/\text{volt sec}$ , or in other words the GaAs mobility is approximately five times that of Si (Figure 3). This advantage in electron mobility is directly reflected in the speed of operation of GaAs devices. There exist many different semiconductors with equal or even better electron mobilities (Figure 4). However, GaAs technology has received a large amount of development for different applications, such as: lasers, detectors, LED's, and microwave devices. For these reasons, much interest and funding are expended in further developing GaAs technology and it is, therefore, much further ahead of other compound semiconductors.

Due to the different material properties of Si and GaAs, different types of transistors are utilized (Figure 5). In Si technology, mainly bipolar transistors and insulated gate field effect transistors are utilized. Due to the short lifetime of minority carriers (in the order of picoseconds), bipolar transistors cannot be built in GaAs. Furthermore, no insulated gate field effect transistors of operational quality are being fabricated due to limitations in the insulator. The main technology of GaAs circuits is based on Schottky barriers or Metal-Semiconductor-Field-Effect-Transistors (MESFETS).

As indicated in Figure 5, MESFETS are formed utilizing semiconducting GaAs islands on semi-insulating GaAs substrates. The islands are formed either by epitaxial growth or by ion implantation of suitable dopants into semi-insulating GaAs. In operation, the gate voltage controls the conductivity of the gate area. Typically, n-type GaAs islands are used, i.e.: the mobile charge carriers are electrons. With zero volts applied to the gate with respect to the source, the transistor

conducts current between drain and source. However, when a negative potential of minus three volts is applied to the gate, the gate area is depleted or in other words, the electrons are repelled from the gate area. Under this condition, no conductance exists between drain and source. This example illustrates how the drain to source conductance can be controlled by the gate voltage. The gate represents a Schottky diode which is blocking with negative applied voltages; hence, no gate current flows under normal operation of the device.

Considerable work is in progress to build integrated circuits in GaAs, utilizing MESFET technology. At present, medium scale integrated circuits are being fabricated, consisting of up to 100 gates. A typical circuit is a "divide-by-eight counter" (Figure 6), which operates with input frequencies from d.c. to 8 GHz.<sup>2</sup> Work is in progress to improve manufacturability, reliability, performance and density of these circuits.

One main problem with the GaAs technology is the absence of a suitable insulator technology for surface passivation. The main reason for the fast development of Si integrated circuits lays on the existence of an almost ideal Si based insulator technology, namely: Silicon Dioxide ( $\text{SiO}_2$ ). This insulator can be grown by thermal oxidation of the Si substrate in an oxidizing atmosphere, such as dry oxygen (Figure 7). The Si- $\text{SiO}_2$  interfaces can be prepared to be almost perfect, i.e.; they contain only minute ( $10^{10}/\text{cm}^2$ ) surface state densities (Figure 8). These insulators can be advantageously employed in insulated gate field effect transistors and charge coupled devices. Furthermore, this insulator can be used to passivate Si surfaces (Figure 9). One example is the passivation of surfaces over p-n junctions to minimize surface leakage currents and to maximize breakdown voltages. Also,  $\text{SiO}_2$  can be utilized to passivate Si surfaces from chemical attack due to gases and vapors. Finally,  $\text{SiO}_2$  can be used as a doping barrier during doping of special areas of the device, such as: source and drain in a MOSFET.

Much work has been devoted towards establishment of an acceptable insulator for GaAs devices. From these studies we realize, that it is very unlikely that an universal insulator technology will be found for GaAs which will be similar in all or most respects to  $\text{SiO}_2$  on Si (Figure 10). Hence work is underway to develop specific insulators for specific requirements in GaAs device technology. One area of critical importance is the passivation of the area between drain and gate and

between source and gate in GaAs MESFETs. The surfaces contain large surface state densities which change their charge with the change in potential in the specific area. This charging results in a reduction of amplification in these transistors, especially at high frequencies.

Consequently, AFAL is working on developing a passivation technology for GaAs MESFET application. Due to the complexity of the problem, a number of insulator technologies have been evaluated and new analytical techniques have been studied which are described in the following sections.

## II. INSULATOR FORMATION TECHNIQUES:

### 1. Deposited Films:

Deposited films of silicon oxide, silicon nitride, silicon oxynitride and germanium nitride have all been studied. In these experiments, a main concern is the compatibility of the insulating film with the GaAs substrate. First of all, the adherence of the film to the substrate must be sufficient to allow processing of the structure without liftoff of the insulating film. Furthermore, the thermal expansion coefficients must be sufficiently matched; problems in this area cause breakage of the GaAs substrate since GaAs is more brittle than Si. In this respect, it is desirable to deposit these films at not too high temperatures (say 250°C instead of 750°C) to minimize damaging effects due to mismatch in the expansion coefficients. Advanced deposition techniques, such as: plasma-enhanced deposition or photo-enhanced deposition techniques are being used. Of main interest is the establishment of an insulator-semiconductor interface with sufficiently low surface state density.

### 2. Thermal Oxidation:

Another approach being actively pursued is the formation of a thermal oxide but not necessarily gallium or arsenic oxide. The oxidation of GaAs requires temperatures of approximately 500°C. At these temperatures,  $\text{As}_2\text{O}_3$  is volatile, leaving  $\text{Ga}_2\text{O}_3$ , which appears as a polycrystalline, conductive film rather than an amorphous, insulating film. The reason for this is due to the fact that Ga is a conditional rather than a primary glass former and requires another element to form glassy material. Experiments on thermal oxidation of  $\text{GaAs}_{1-x}\text{P}_x$  indicate that the thermally formed oxides are glassy and insulating. One approach therefore, is to form a

GaAs  $P_{1-x}$  surface layer on GaAs by ion implantation of p and subsequently to thermally oxidize this structure. The advantage of this approach is that the semiconductor-insulator interface is formed within the GaAs substrate and consequently, this interface was at no time exposed and/or contaminated by the atmosphere. In contrast, one of the main concerns with deposited films is that the semiconductor surfaces become the interfaces and consequently are contaminated to some extent.

A further approach for formation of insulating films utilizes the anodic process; at present, most of our insulating films are prepared by wet anodization.<sup>4</sup>

### 3. Aqueous Anodic Oxidation:

When the semiconductor is inserted into an aqueous solution with its high dielectric constant, the surface atoms of the semiconducting material are dissolved into the liquid as their ionic bonds are weakened. The atoms enter the liquid as multiple positively ionized species, such as  $Ga^{+++}$  or  $As^{+++}$ , leaving on the semiconductor surface an immobile negative charge which has to be neutralized by mobile holes from the bulk of the semiconductor. After a second electrode is placed as cathode electrode into the solution, the semiconductor can be employed as anode with a positive potential which aids the hole flow to the semiconductor surface so that more ions can be released. These ions travel towards the cathode.

If sufficient ions are released they form a dense ionic cloud in front of the anode. This is particularly easy if either the solubility or the diffusion coefficient of these ions is reduced by the introduction of a suitable liquid into the aqueous solution. It was found that some liquids are particularly effective, such as glycol.

The ions in this cloud will capture  $OH^-$  ions of the aqueous solution, and with the simultaneous formation of  $H_2O$ , are oxidized. It is likely that most of them will form well-known oxides such as  $Ga_2O_3$  or  $As_2O_3$ , which will exceed a density saturation level in this cloud so that they begin to precipitate against the semiconductor. An oxide layer begins to get deposited thus.

Further growth is now only possible if ionic transport takes place across the oxide. Each of the ionic species has a threshold field for drift and a specific value of mobility. With normal current densities applied across the semiconductor surface which is immersed into the electrolyte, the fields



across the oxide and its interfaces are sufficiently high for the motion of all ions, namely  $\text{OH}^-$  and the positively ionized components of the semiconductor. However as the mobility of  $\text{OH}^-$  is much smaller than that of the multiply ionized components, the primary growth occurs at or near the electrolyte-oxide interface. Unfortunately, the current density cannot be reduced beyond a minimum value which is different for each material. This value has sometimes been called the dissolution current as it seems to agree with the equivalent cation current due to the dissolution of the oxide in the electrolyte when no external current is applied. It can be understood as the flow of those cations which, after dissolution from the oxide, successfully leave the anode region. Only when this minimum current density is exceeded, can growth take place. This means that with the electrolytes known so far, native oxides on most III-V Compound Semiconductors such as GaAs, can only be produced after exceeding the drift threshold for all the ionic species involved.

However, Al and some other metals have a very small dissolution current. After depositing a layer of such a metal by evaporation on top of the semiconductor, this metal will first be oxidized in the electrolyte. After it has been completely transformed, the oxidation of the semiconductor begins. For a high current density, the semiconductor components drift as cations across the  $\text{Al}_2\text{O}_3$  and native oxide of the semiconductor appears to top of the  $\text{Al}_2\text{O}_3$ . On the other hand, for a low current density the semiconductor components cannot become mobile, and it is only  $\text{OH}^-$  which crosses the  $\text{Al}_2\text{O}_3$ . Correspondingly, native oxide of the semiconductor appears only between  $\text{Al}_2\text{O}_3$  and the semiconductor. It is therefore possible to produce various types of layered structures. It is useful to consider this now systematically for various types of device applications.

The oxide growth can be undertaken either with a constant-current source or with a constant-voltage supply in series with a sufficiently high series resistance in order to limit the initial current density. A voltage supply without such a limiting resistance is not advisable as the initial current density can easily become so high that hot spots and other detrimental effects can occur during the initial stage of growth so that a deterioration of the oxide quality appears. A constant-current case would require a voltage measurement between cathode and anode in order to monitor the growth procedure. A voltage and series-resistance agreement can enable one to monitor the growth by measuring the current flowing

across the electrolytic cell. For the relatively high final growth voltages involved across most of the oxides of device interest, it is not required to undertake the more refined electrochemical potential measurements as these would then be normally a negligible fraction of the applied voltage.

It is possible to model the growth behavior relatively satisfactorily by a simple treatment, provided that precautions are taken for a uniform current density across the semiconductor surface which is exposed to the electrolyte. By way of example, this is to be outlined here for the constant-voltage plus series-resistance arrangement. The treatment of the other case of growth is very similar.

The general current functions measured are shown in Figure 11.<sup>5</sup> A typical experimental set up is given in Figure 12, where it is also indicated that a light source is needed in order to have sufficient holes available for the neutralization of the negative surface charge created by the removal of positive cations. This illumination is particularly important for n-type material where practically no holes would be present otherwise. Failing to provide a sufficient supply of holes means that the space charge layer set up by the negative surface charge caused by the departing cations absorbs a substantial part, if not all, of the externally applied voltage so that the oxide thickness will be much smaller than that predicted by the model.

Recent experiments were performed also utilizing non-aqueous anodic growth (rather than the above described aqueous anodic growth), utilizing an ammonium pentaborate solution in ethylene glycol. Superior results were obtained when Al films on GaAs were anodized in this solution.

#### 4. Plasma Anodization:

We are now in the process of establishing a plasma anodization growth facility. The plasma anodization will result in less contaminated films than the wet anodized films since gases are obtainable with less contamination content than liquids. The attached Figure 13 indicates the setup for plasma anodic growth.<sup>6</sup> An R.F. discharge creates an oxygen plasma and oxygen ions or excited neutral oxygen atoms reach the surface of the sample to be anodized. A voltage applied to the sample creates an electric field in the growing insulator of approximately  $10^6$  V/cm which assists in the migration of the ions, namely O, Ga, As, and Al. Superior films have been reported when Al films on GaAs were formed.

### III. ANALYTICAL TECHNIQUES:

The insulating films on GaAs and their interfaces are evaluated analytically for their mechanical stability, for their chemical characteristics and composition and for their electrical behavior.

The insulating films have to have adequate adherence to the substrate. The films have to appear uniform on inspection with a microscope, and liftoff, peeling of the film or rupture of the substrate is not acceptable, since the films have to stand further processing such as heat treatment and immersion into liquids, care must be taken that these processes don't damage the films.

In recent years, instrumental techniques for chemical analysis of thin layers have been greatly improved. A survey of these techniques was recently presented by G. R. Larrabee.<sup>7</sup> We have utilized optical characterization, X-ray Photoelectron Spectroscopy (or ESCA), Secondary Ion Mass Spectroscopy (SIMS) and Auger Electron Spectroscopy (AES). To detail these techniques and describe all of our results would be beyond the scope of this presentation. However, to give an example of the work involved, we describe here the AES experiment performed in an ultra-high vacuum system (Fig 14). The sample is bombarded with electrons of several thousand electron volts (keV) energy. These high energy electrons are able to ionize atoms in the sample by knocking out electrons from inner shells. Now electrons with higher energy can relax into the empty state, thereby releasing a characteristic energy. This energy is transferred to another electron which subsequently is emitted into vacuum where it is detected and its energy measured and related to specific atoms. The attached Figure 15 indicates the results obtained showing the derivative  $dN/dE$  signal vs. energy  $E$ . Two different traces are shown indicating different surface conditions. Simultaneous to the electron bombardment, the samples are bombarded with argon ions with energies of several keV. These argon ions sputter off the surface of the sample thereby profiling the film composition. Figure 16 presents such a profile of an anodized film of Al on GaAs. On the abscissa the sputter time is presented which relates to the distance from the film surface and on the ordinate, the AES signal strength for the important species are presented namely O, Al, Ga and As. These data let us understand the chemical composition of the film at different locations and especially allow us to evaluate the chemical composition in the insulator-semiconductor transition region.

The most important studies evaluate the electronic behavior of these films and their interfaces since adequate electronic characteristics are required for proper device performance. The most common technique is to measure capacitance as a function of voltage (C-V) for metal-insulator-semiconductor structures.<sup>8</sup> In general the sample is first biased to attract semiconductor charges to the interface or to put the interface into accumulation (positive voltage for n-type semiconductor). The capacitance measured then is that of the insulator. Now the voltage is altered to a reverse position (negative voltage for n-type semiconductor), causing depletion of carriers under the metal electrode. Hence the insulating structure now consists of the depleted semiconductor and the insulating oxide film, thereby decreasing the capacitance. Figure 17 demonstrates a typical C-V characteristic for anodized GaAs structures. Difficulties have been encountered in interpreting these capacitance characteristics, since charge apparently is injected into the insulator and this charge influences the capacitance values measured. In order to better evaluate these measurements, we incorporated a photopulse technique. In a pulse setup, we first put the metal-insulator-semiconductor structure into depletion and measure within 10 milliseconds the capacitance of the structure; we then shine a strong photopulse of approximately 4 milliseconds duration onto the sample, which causes the depletion region to collapse and the generation of a voltage pulse of the size of the surface potential. This method then allows direct evaluation of the capacitance as a function of surface potential, thereby eliminating the influence of the unquantified charging of the insulator. These data can then be analyzed theoretically to obtain information on doping concentration. These transient-photo-measurement results can then be applied to the C-V results to evaluate charging of the films. We also measure the charging and discharging of the sample under the above conditions to obtain direct information on the capacitance of these structures.

#### IV. DEVICE APPLICATIONS:

A large amount of our future work will be concerned with applying this passivation technology to GaAs MESFETs and GaAs MESFET integrated circuits. Our first concern will be to apply this technology to the areas between gate and drain and between gate and source of MESFETs. Further use will be concerned with dielectric isolation of these MESFETs to simplify processing and to improve density and performance of these circuits. We will keep an open mind to consider at intervals

the applicability of these passivation layers to depletion type insulated gate FETs as well as to GaAs Charge Coupled Devices (CCDs).

Due to the very high speed of GaAs MESFET circuits primary applications will be in very high speed logic (i.e.: 10-18 GB/S) for radar signal processing, ECM, satellite communications and computer applications. A major impact will be from the fabrication of very high speed A/D converters. Since GaAs integrated circuits will be premium cost circuits, their use will be restricted to the highest speed parts of the system or to special applications where silicon circuits will not function.

If the development of this insulator technology progresses far enough, MOSFET type devices may become feasible in GaAs and these could be produced at lower cost due to their higher density and lower power dissipation. It is unlikely, however, that these GaAs MOSFET integrated circuits would ever be cost competitive with silicon circuits at speeds where silicon can be used.

Transferred electron devices are essentially ultra-high speed switching devices which operate at picosecond speeds with power dissipations of about 60 mW/gate and very high field strengths to initiate a "high field domain" which propagates down the device at about  $10^7$  cm/sec. Gate areas are typically about 20 mil<sup>2</sup> whereas TTL gates are typically about 110 mil<sup>2</sup>, Schottky TTL gates about 126 mil<sup>2</sup>, and ECL gates about 120 mil<sup>2</sup>. The transferred electron effect occurs in several III-V semiconductor materials (i.e.: GaAs and InP) due to a bulk negative differential mobility caused by the transfer of electrons from a high mobility band to a low mobility band. Since TEDs are high field devices, achievement of high fields with low leakage demands high quality insulators for passivation of the surface in planar processes. Likewise, the achievement of low noise at high fields is critically dependent on low leakage insulators and passivation.

One of the major applications of GaAs TEDs will be in A/D converters. The performance of analog to digital converters for ELINT applications is limited by the sampling aperture width. GaAs TEDs will permit a 5 picosecond sampling aperture

with TED comparators which would allow frequency components up to 500 MHz with 6 bit resolution. Competitive tunnel diode sample and hold circuits are limited to about 16 ps or greater aperture. TEDs provide a 220% improvement in bandwidth. A noise threshold of 50-100 mV requires each level of an A/D converter to be 200 mV or more, therefore, for 63 levels, this means at least 12.6 V input is required into the digital converter. This in turn requires high voltage amplifiers with wide bandwidth (which are not currently available). Suitable passivation should be able to cut down this noise level and make these devices much more practical. In general, the most fruitful applications for GaAs TEDs are probably in the following areas: A/D and D/A converters, frequency dividers, latches, special purpose gates, shift register memories, counters, and decoders.

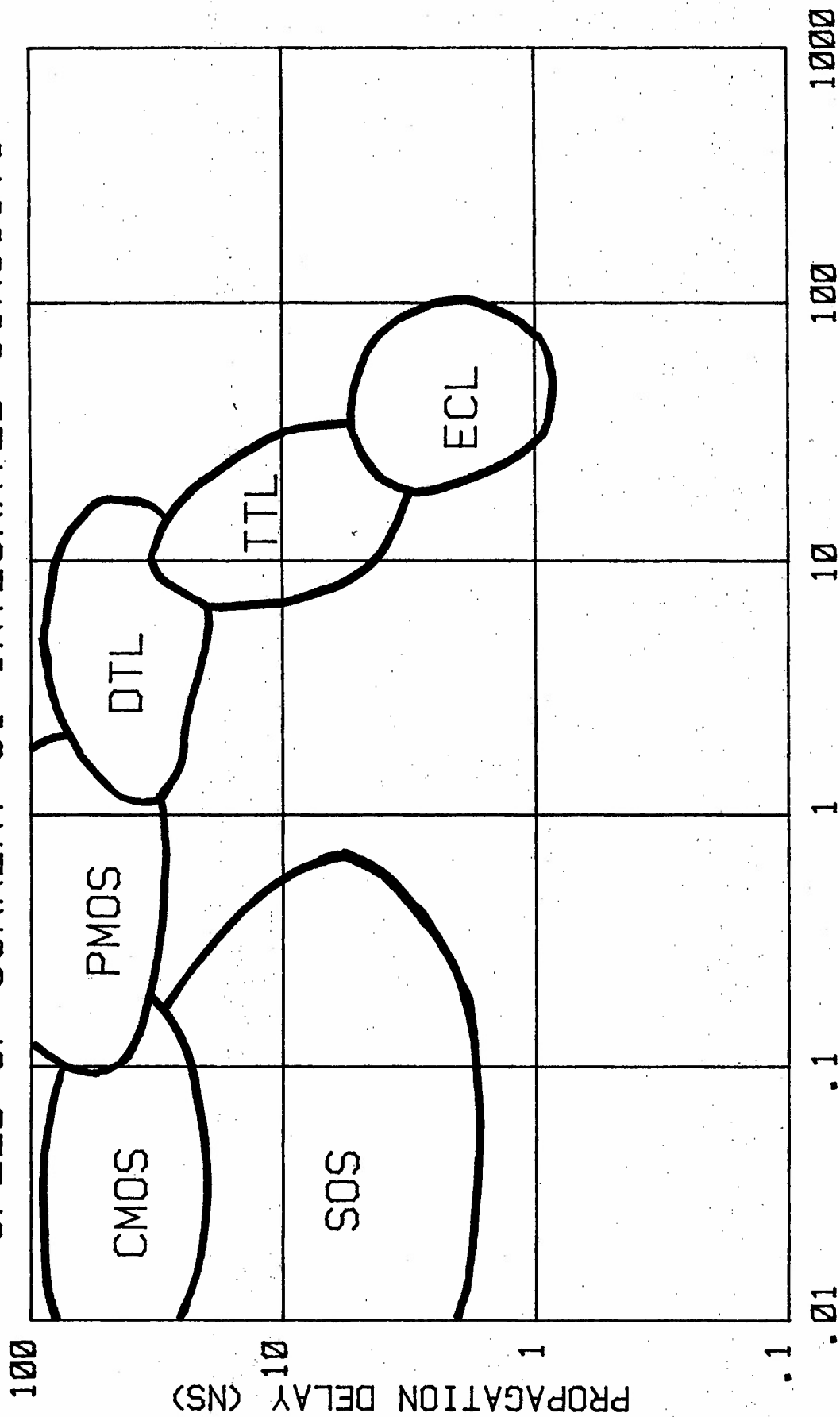
GaAs CCDs show great potential for use in high speed image sensors in the IR and visible regions of the spectrum. Since good detector devices can be built in GaAs - the problem of high speed image scanning could be solved with a minimum of hardware, interconnects, and with high reliability at low cost --- if an adequate CCD device with high transfer efficiency and low leakage can be fabricated. The dielectric films for isolation and passivation of this device are a key technology for the success of this new device. Planar, Schottky gate, buried channel CCDs require very narrow gaps between the metal Schottky gates resulting in a configuration with relatively large areas of metal separated by narrow gaps and substantially long lengths of the gap per transfer stage. This configuration contrasts with MESFETs where narrow stripes of metal are surrounded by large clear areas. Two level metallizations with a large number of cross overs per device require a deposited insulator with very low pin-hole density and excellent step coverage as well as good adhesion and dielectric strength. Currently a plasma-enhanced, deposited glassy dielectric of proprietary composition is being used to fabricate early experimental GaAs CCDs (Figure 18).

In summary, the passivation of GaAs surfaces with a suitable high quality insulator is necessary to achieve low surface state density, low leakage, and low noise in a number of advanced new devices (such as: MESFETs, MOSFETs, TEDs, and CCDs). Air Force applications of these new devices will be primarily in premium cost, high speed circuits where performance at above 10 GB/S is of paramount importance. Many such applications exist within the Air Force in the areas of radar, ECM, satellite communications, high speed computers and image sensors. Application of this advanced technology can reduce the cost of critical parts of systems where a large premium is paid for high performance.

### REFERENCES

1. Sze, S.M., "Physics of Semiconductor Devices", John Wiley and Sons, New York, 1969.
2. Tuyl, Rory L. Van, Charles A. Liechti, and Charles A. Stolte, "Gallium Arsenide Digital Integrated Circuits", AFAL-TR-76-264, Contract F33615-73-C-1242, Air Force Avionics Laboratory, Wright-Patterson AFB, Ohio, 45433, April 1977.
3. Nicollian, E.H., "Surface Passivation of Semiconductors", J. Vac. Sci. and Tech., Vol. 8, No. 5, P. 539-540.
4. Hasegawa, H., and H.L. Hartnagel, J. Electrochem. Soc., 123, P. 731, 1976.
5. Bayraktaroglu, B., S.J. Hannah, and H.L. Hartnagel, Electronics Lett., 13, 45, 1977.
6. Chang, R.P.H., and A.K. Sinka, "Plasma Oxidation of GaAs", Appl. Phys. Lett., Vol. 29, No. 1, P. 56-57, July 1976.
7. Larrabee, G.R., "Characteristics of Solid Surfaces", Scanning Electron Microscopy, Vol. I, P. 639-650, 1977.
8. Zaininger, K.H., and F.P. Heiman, "The C-V Technique as an Analytical Tool", Solid State Technology, Vol. 13:5-6, May/June 1970.
9. Clark, M.D., C.L. Anderson, R.A. Jullens, and G.S. Kamath, "GaAs Charge Coupled Devices", Interim Report No. I, 1 Aug. 77 - 31 Jan. 78, Contract No. F33615-77-C-1082, Air Force Avionics Laboratory, Wright-Patterson AFB, Ohio, 45433, Mar. 1976.
10. Krueger, C.H., J.W. Sarver, et al, "The Impact of Transferred Electron Devices on Electronic Warfare Systems", AFAL-TR-75-40, Air Force Avionics Laboratory, Wright-Patterson AFB, Ohio, 45433, Mar. 1976.

# SPEED OF CURRENT Si INTEGRATED CIRCUITS



POWER DISSIPATION (MW/GATE)

Figure 1



# AIR FORCE APPLICATIONS FOR HIGHER SPEED CIRCUITS

- \* Wideband Direct Frequency Counters (ECM)
- \* Fast Phase-Lock-Loop Frequency Synthesizers
- \* Spread Spectrum Communication With High Symbol Rate
- \* Real-Time Radar Data (Fast Fourier Transformations)
- \* High-Speed Analog-to-Digital Converters

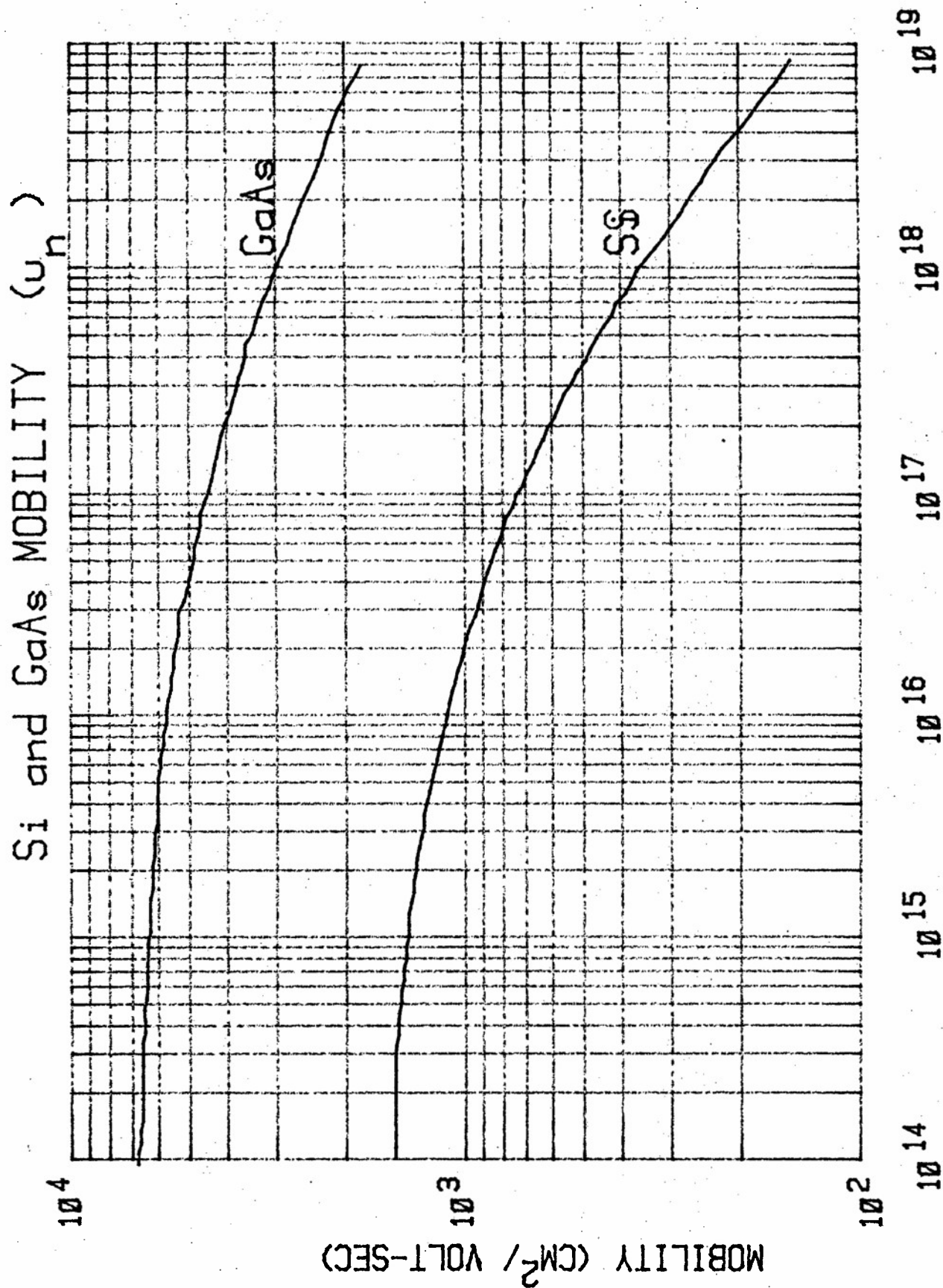


Figure 3

# MOBILITY OF VARIOUS SEMICONDUCTORS

	<u>Electron</u> <u>Mobility</u>	<u>Hole</u> <u>Mobility</u>	<u>Band</u> <u>Gap</u>
	78,000cm <sup>2</sup> /vsec	750cm <sup>2</sup> /vsec	0.16 eV
InSb	33,000	460	0.33
InAs	8,500	400	1.43
GaAs	6,000	4,000	0.32
PbTe	4,600	150	1.29
GaSb	4,000	1,400	0.67
Ge	3,900	1,900	0.80
C-Diamond II	1,800	1,600	5.47
Si	1,500	600	1.12
CdSe	800		1.70
PbS	600	700	0.41
PbS	600	700	0.41

Figure 4

# DIFFERENT TYPES OF TRANSISTORS

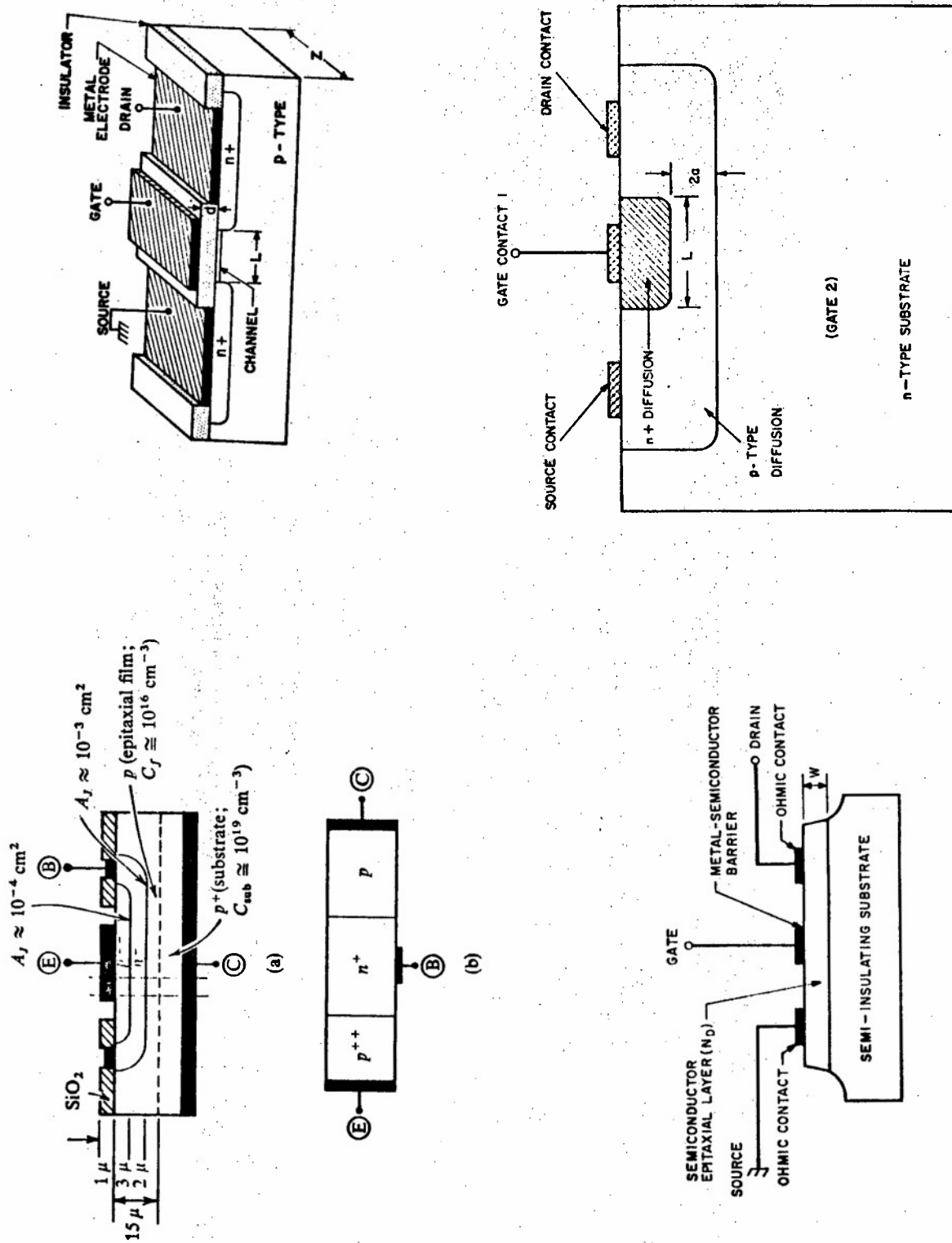


Figure 5

# GaAs DIVIDE BY 8 COUNTER

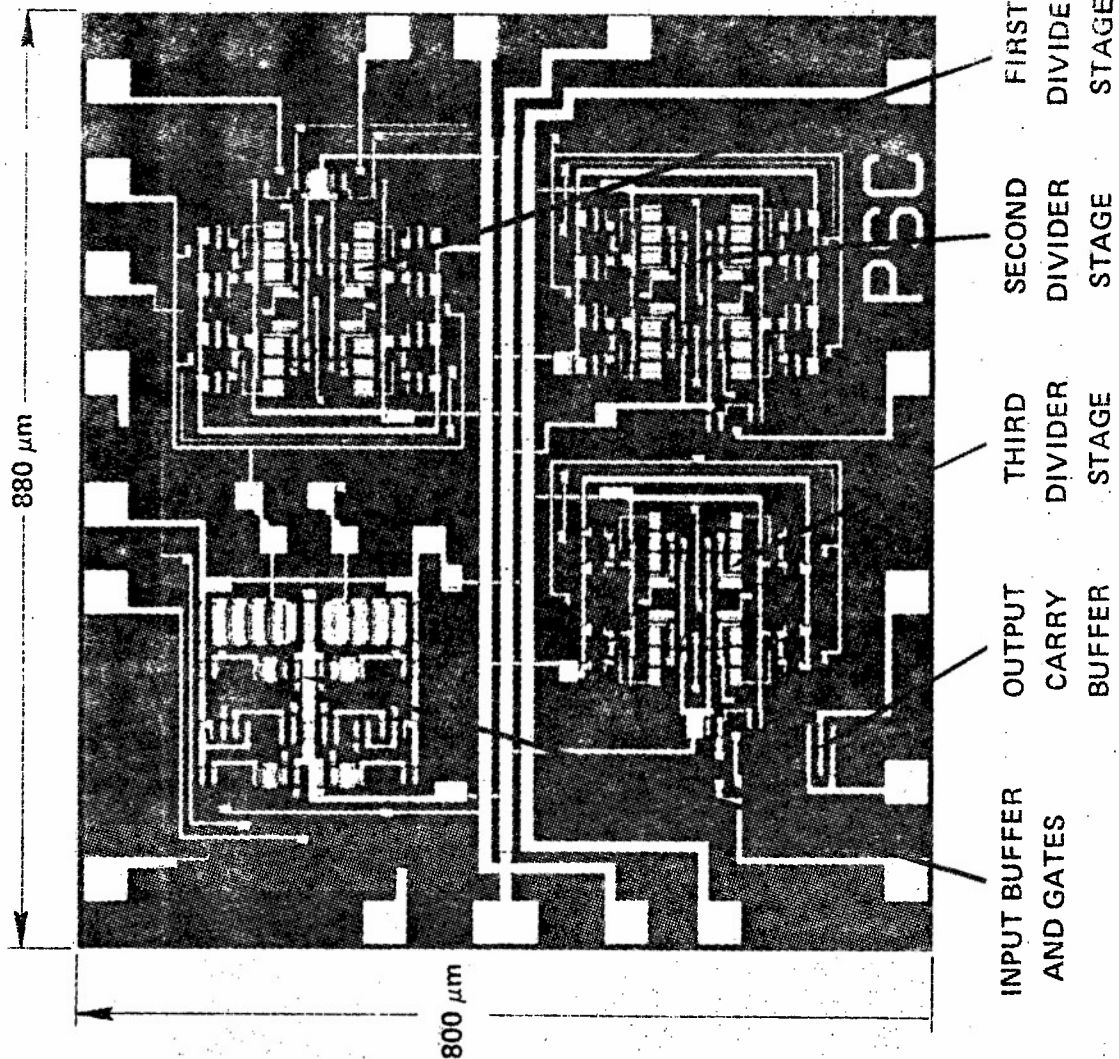


Figure 6

# THERMAL OXIDATION OF Si

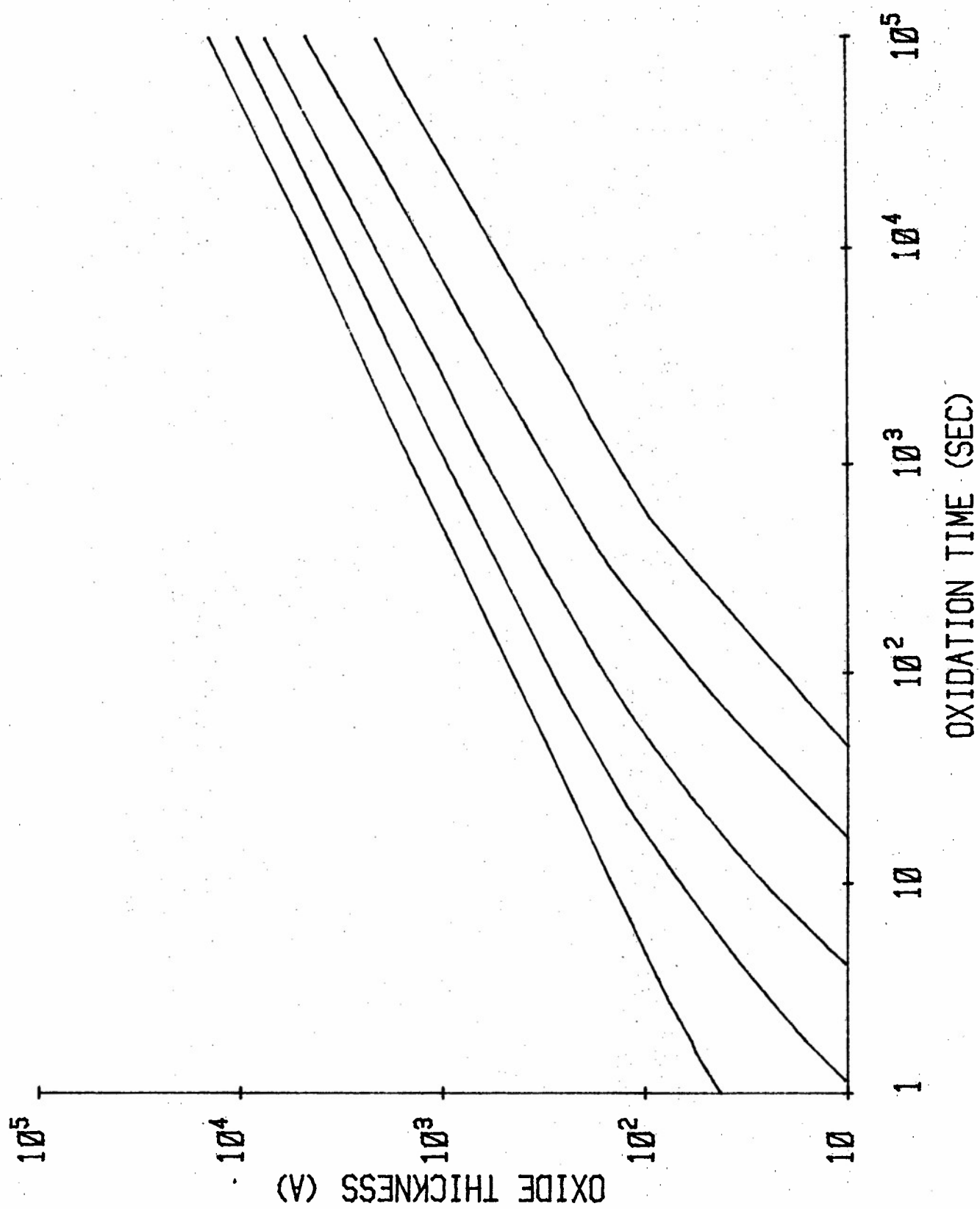


Figure 7

# Si - SiO<sub>2</sub> INTERFACE

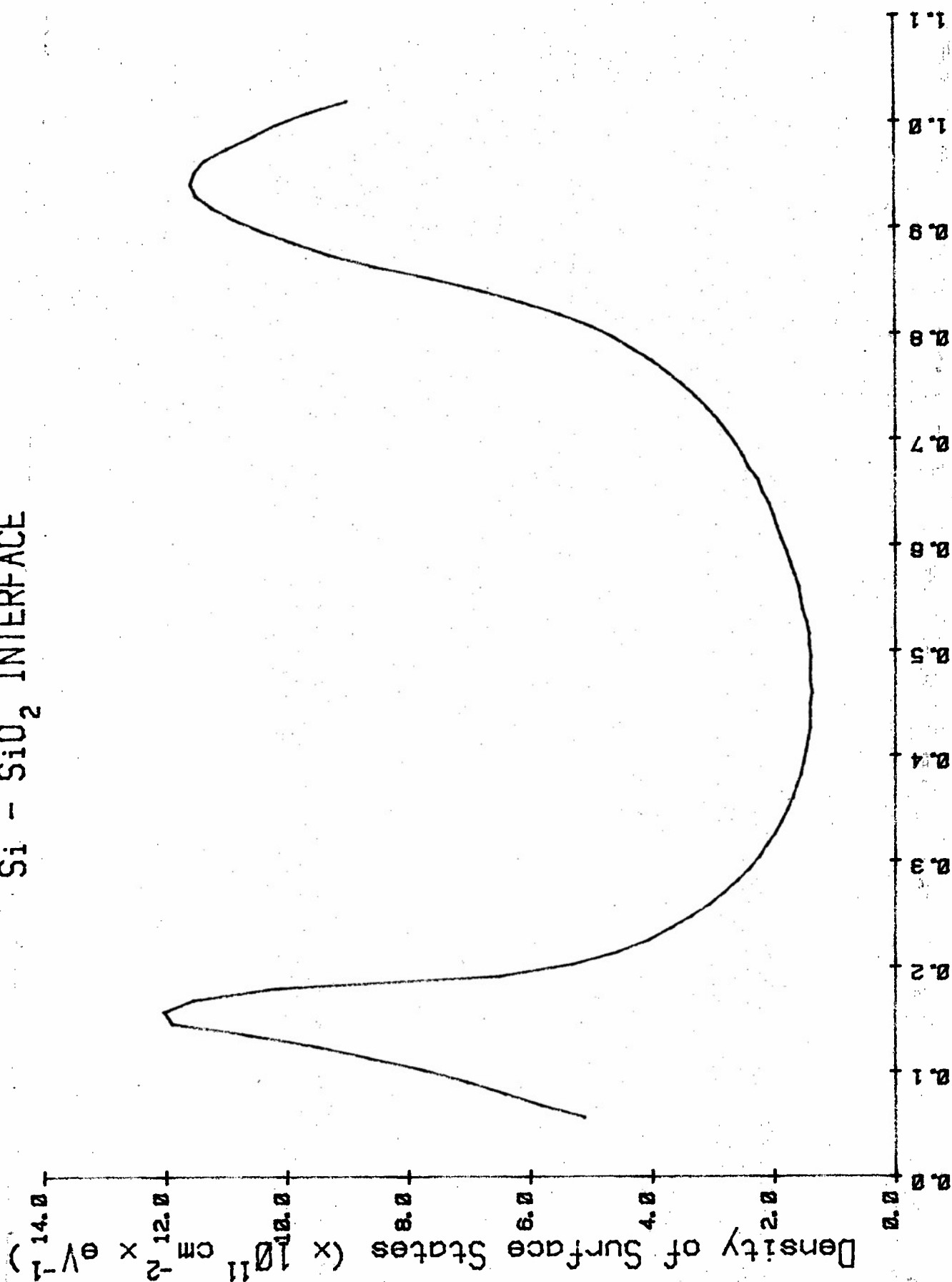
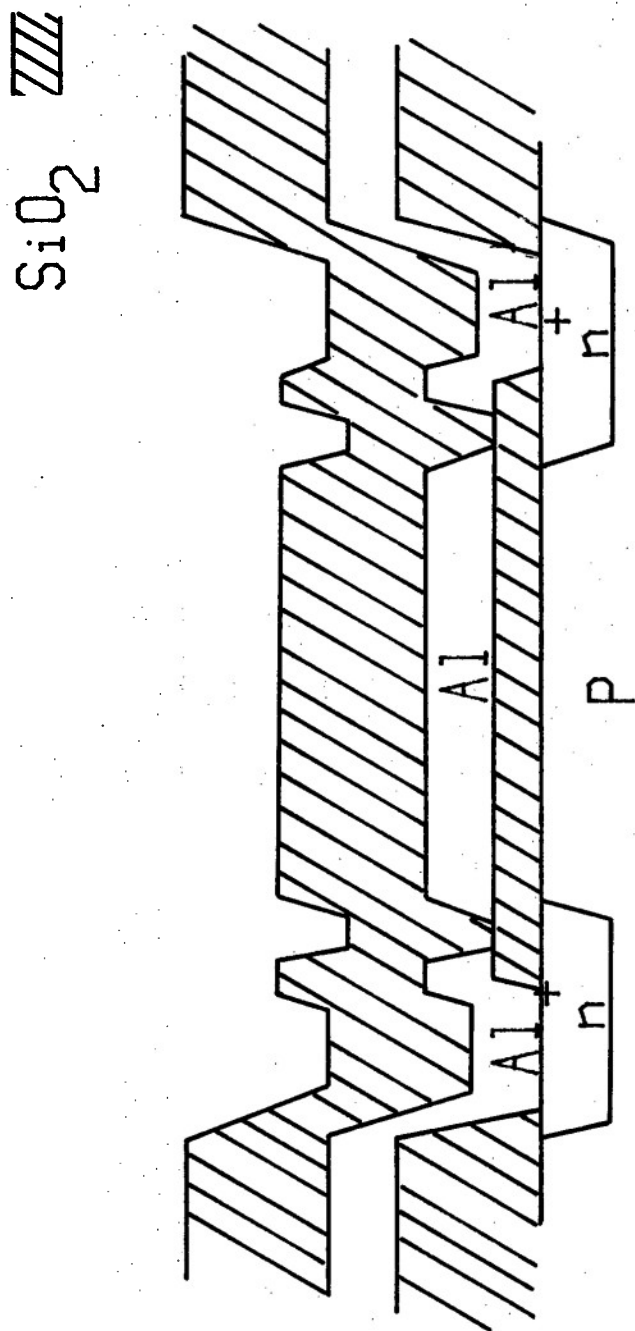


Figure 8

# PASSIVATED SILICON SURFACE



Silicon

Figure 9



# SiO<sub>2</sub> - THE UNIVERSAL INSULATOR

- \* Diffusion Barrier
- \* Control of Surface Leakage Currents
- \* Control of Junction Breakdown Voltage
- \* Electrical Insulation of Metallization
- \* Gate Insulator
- \* Scratch Protection
- \* Chemical Protection

# ANODIZATION CURRENT DENSITY VS TIME

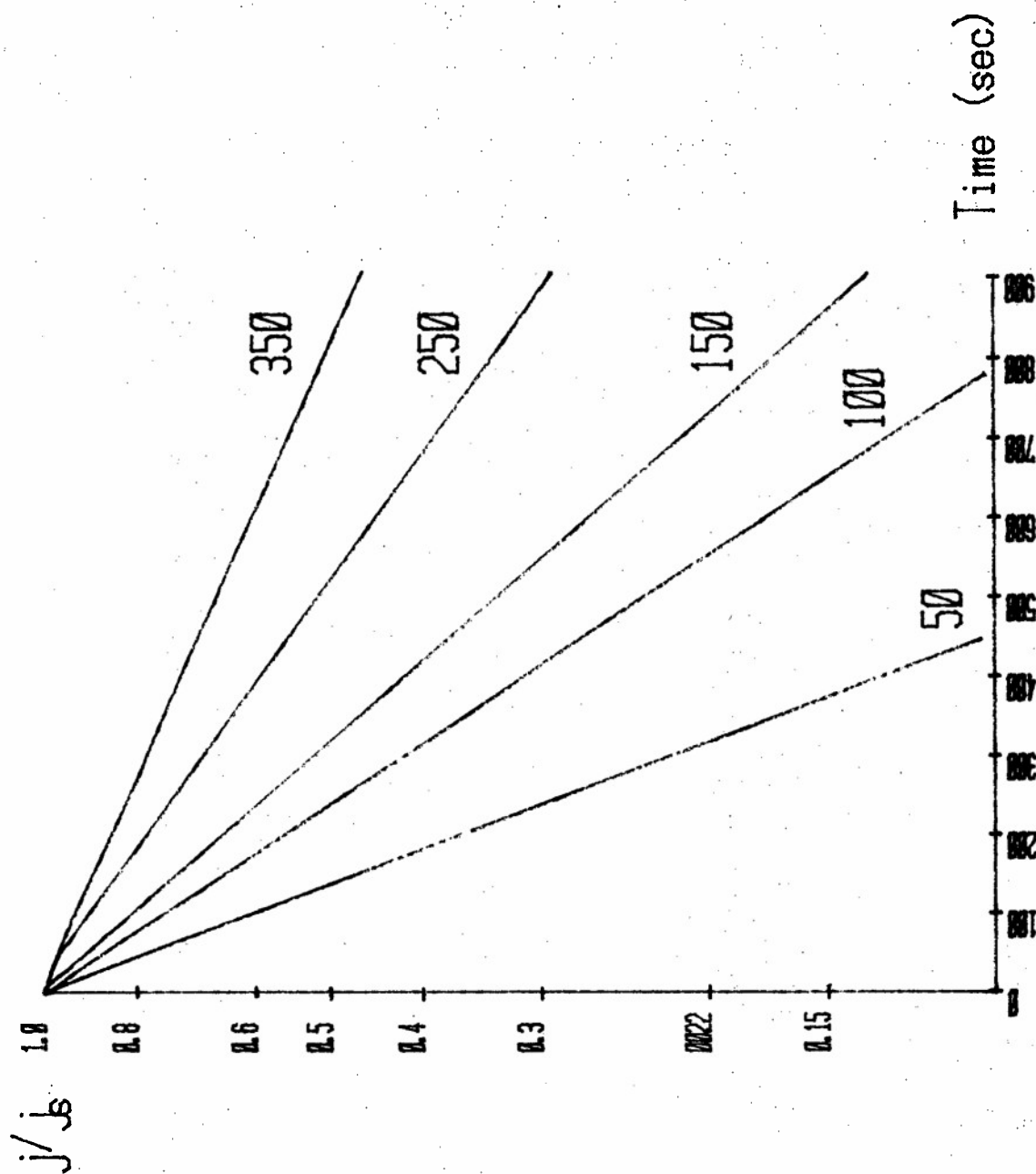


Figure 11

# EXPERIMENTAL SET UP FOR ANODIC OXIDATION

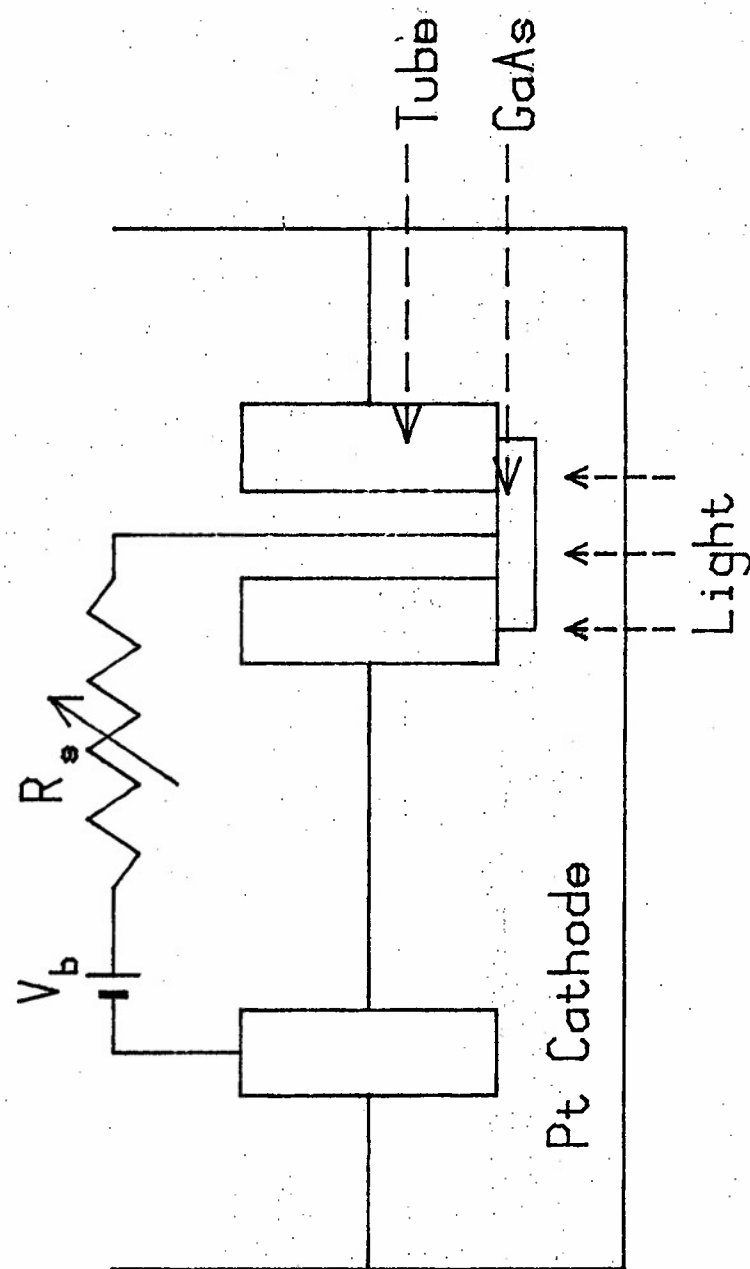


Figure 12

# PLASMA ANODIZATION SYSTEM

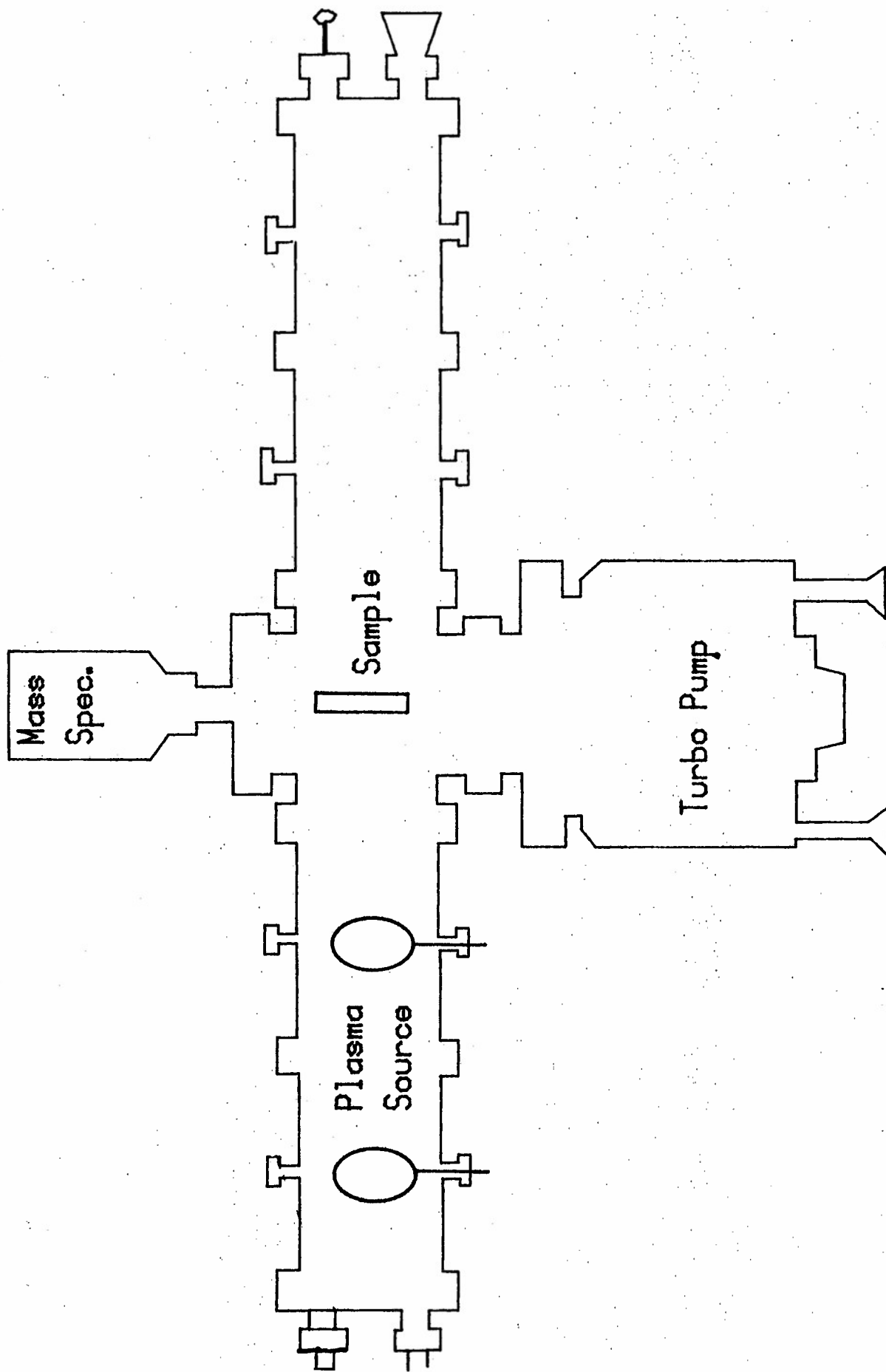


Figure 13

# AUGER ELECTRON SPECTROMETER

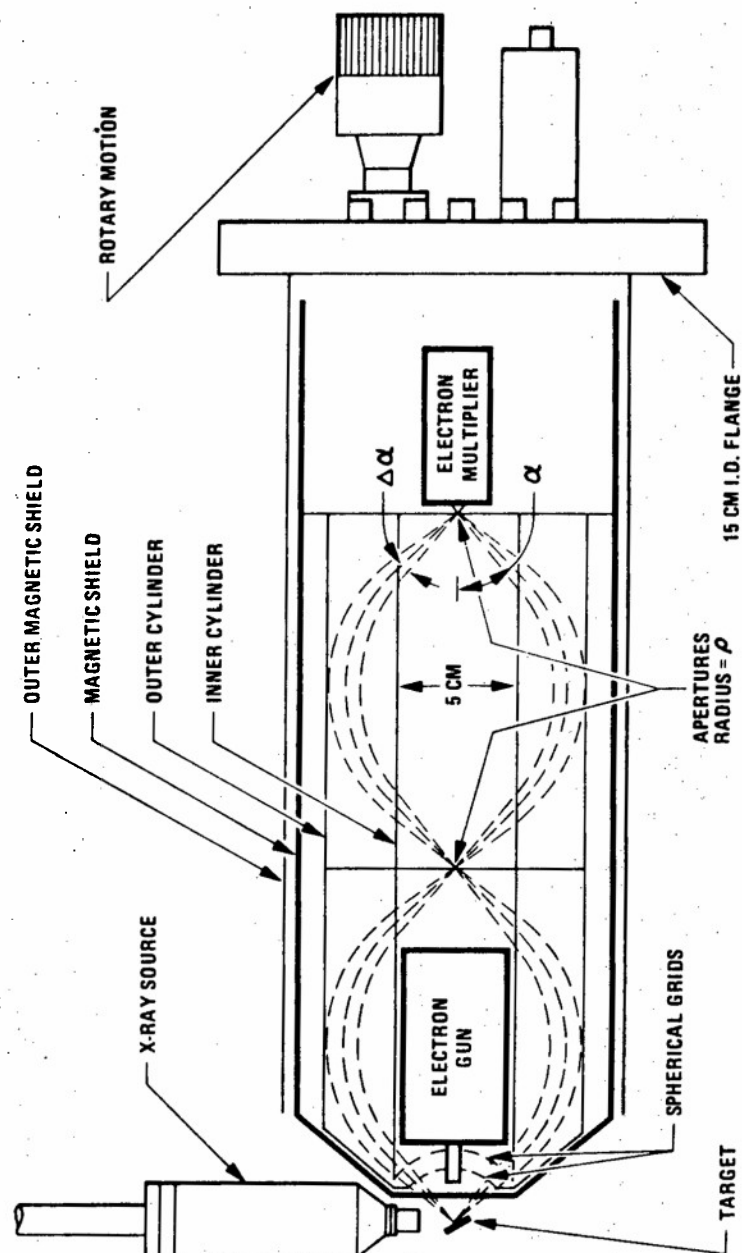


Figure 14

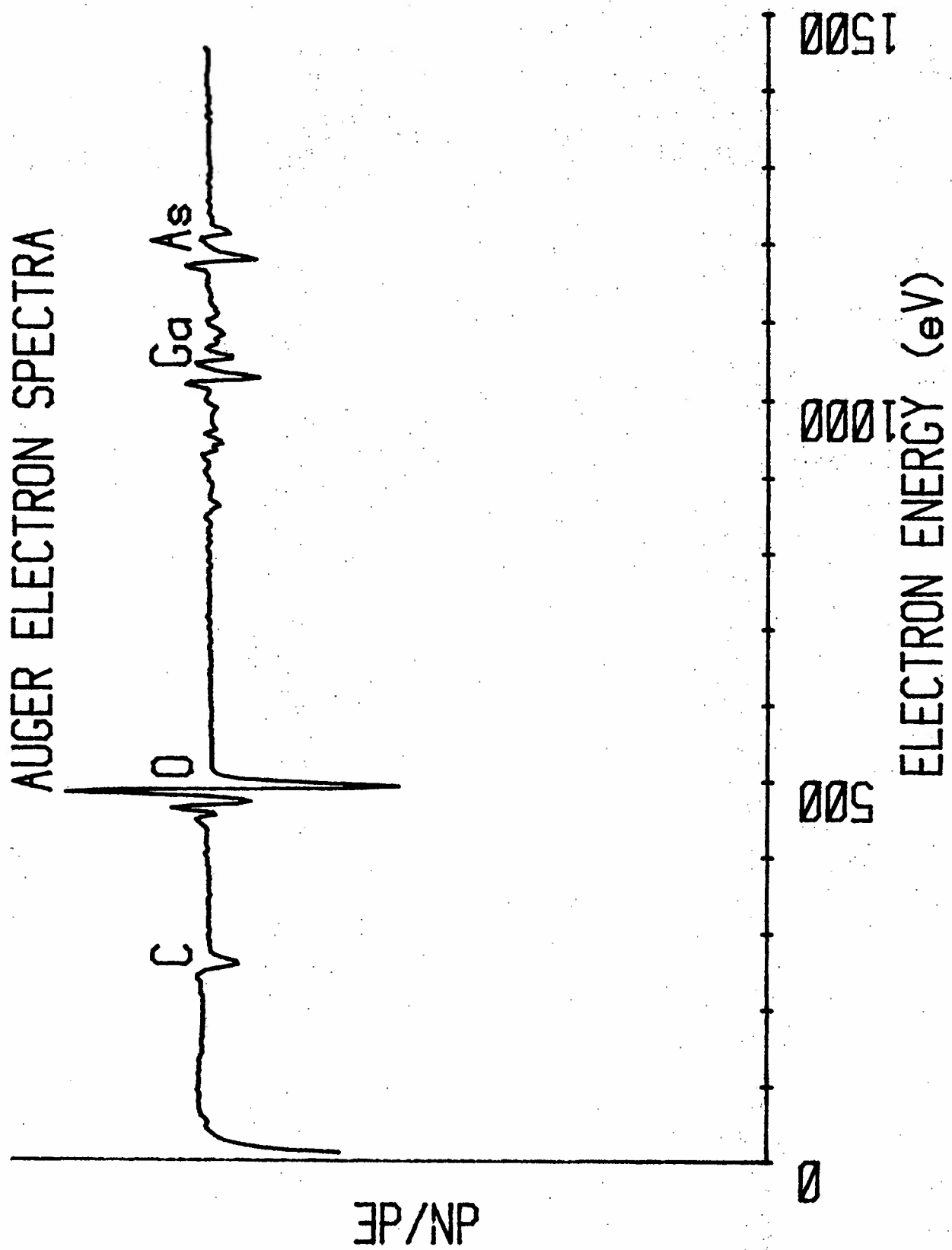


Figure 15

# PROFILE OF ANODIZED Al ON GaAs

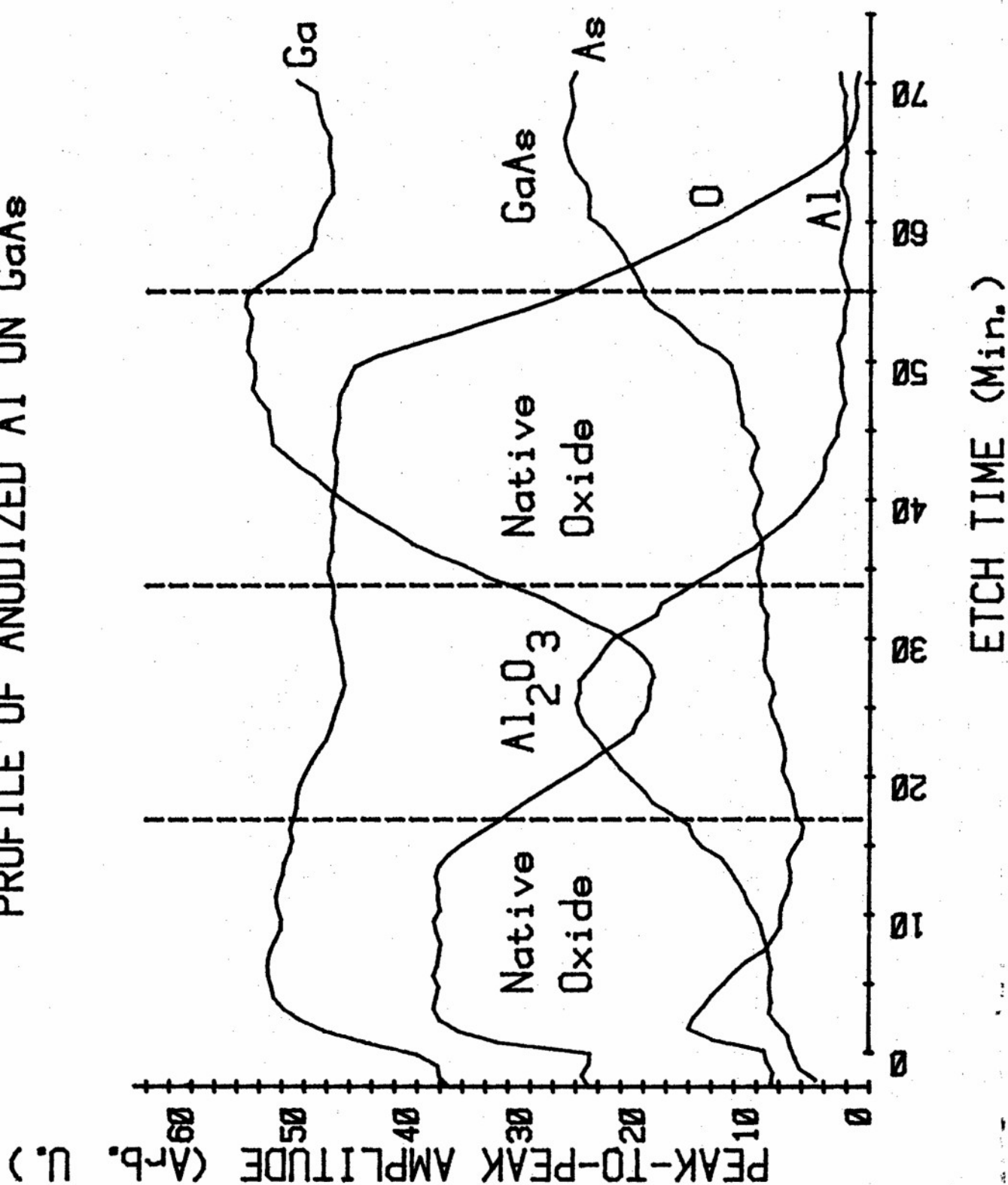


Figure 16

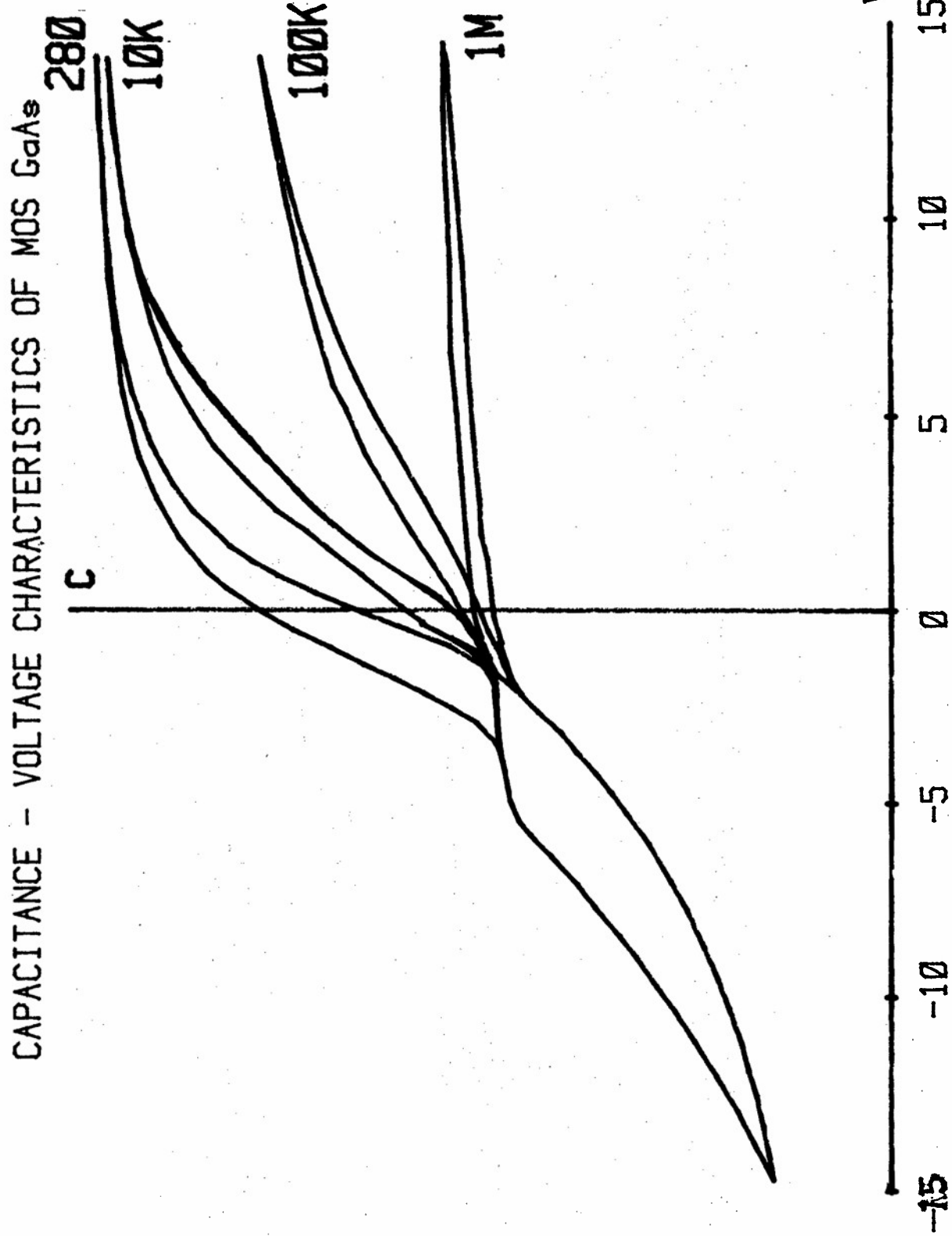


Figure 17



# GaAs SCHOTTKY BARRIER CCD

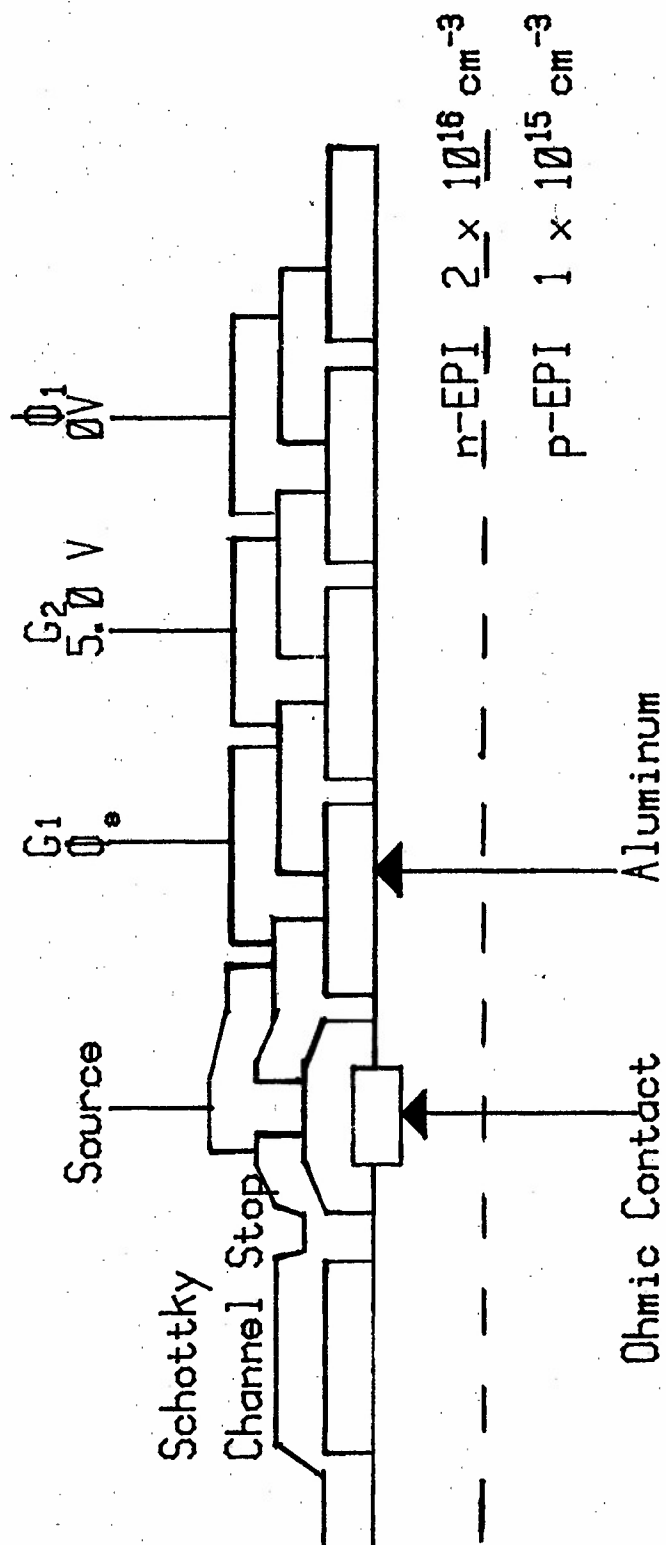


Figure 18

# TRANSFERRED ELECTRON DEVICE

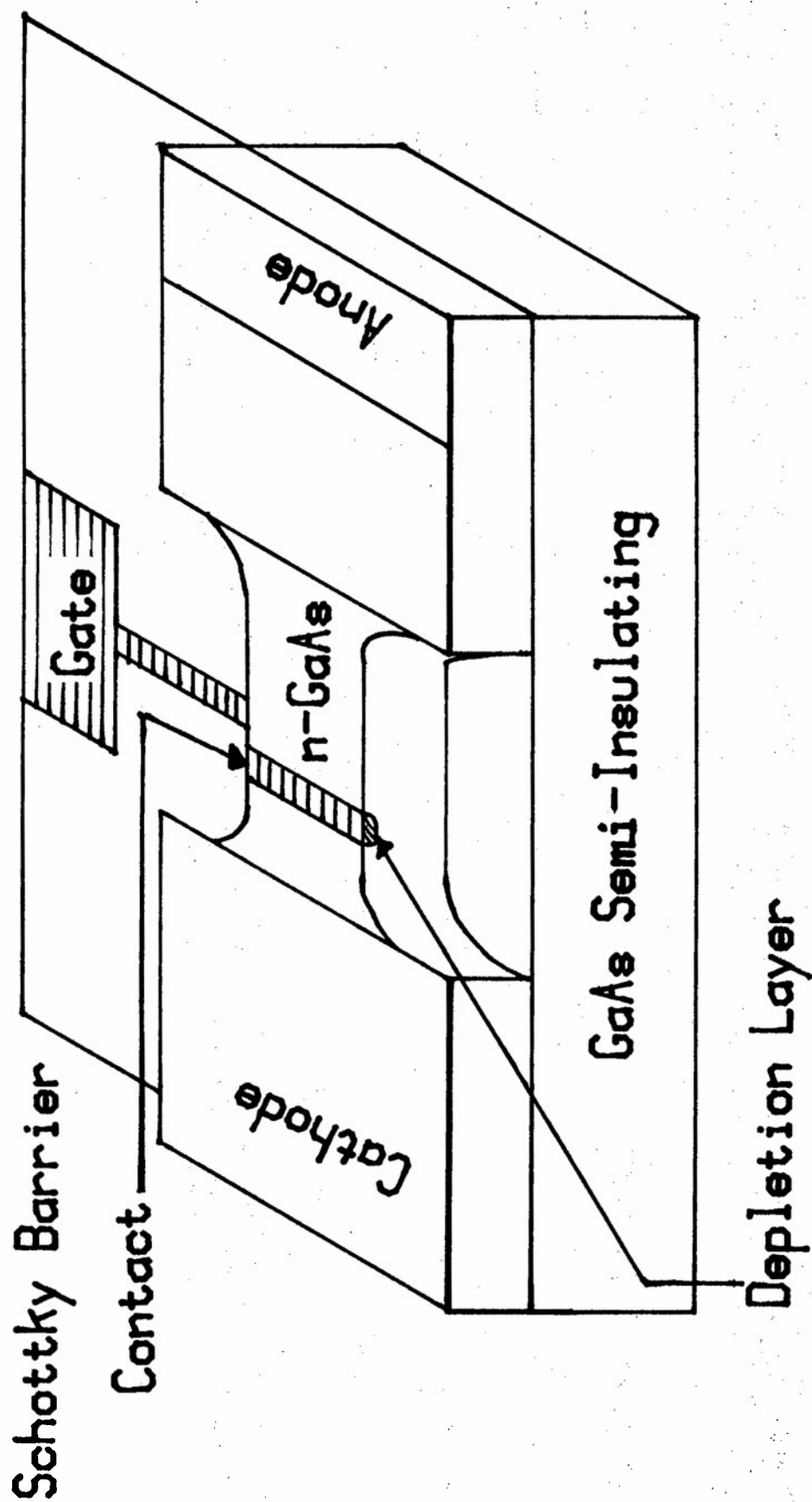


Figure 19

### Biographical Sketch

Fritz L. Schuermeyer was born in Munich, Germany on March 1, 1935. He received the M.S. and Ph.D. degrees in physics from the Technical University, Munich, Germany, in 1959 and 1961, respectively. Since 1963, he has been with the Air Force Avionics Laboratory at Wright-Patterson AFB, Ohio, performing work in the areas of thin films, MNOS devices, and on the passivation of GaAs surfaces. He has published and presented many papers and holds four patents.

Hans L. Hartnagel was born in Geldern, Germany, on January 9, 1934. He obtained his Dipl. Eng. degree from the Technical University of Aachen, Germany and his Ph.D. and D. Eng. from Sheffield University in England. Since January 1971 he has held the Chair of Electronic Engineering at the University of Newcastle upon Tyne, England. He served as a consultant in India for UNESCO and with the Japanese Government in Japan. Recently, he served as a Visiting Scientist with the Air Force Avionics Laboratory at Wright-Patterson AFB, Ohio, where he consulted on the GaAs Passivation program. He has published extensively in many international journals.

John M. Blasingame was born in Raleigh, North Carolina, on June 27, 1930. He graduated from Vanderbilt University in 1952, receiving a B.A. degree in chemistry. He did graduate work in physics at Vanderbilt and Ohio State University. In 1955 he joined the Semiconductor Research Section, Electronic Components Laboratory, Wright-Patterson AFB, Ohio. He became Technical Manager of the Thin Film Phenomena Group in 1963 and Chief, Memory Technology Group in 1971. He conducted basic research on GaAs surface passivation, electron beam memory devices, and magnetic bubbles from 1975 until September 1978, when he became Project Manager for Very High Speed Integrated Circuits in the Microelectronics Branch of the Avionics

**(U) IDENTIFICATION OF IMPURITY COMPLEXES IN GALLIUM ARSENIDE  
DEVICE MATERIAL BY HIGH RESOLUTION MAGNETO-PHOTOLUMINESCENCE**

**BY**

**Robert J. Almassy, Maj, USAF**

**Donald C. Reynolds**

**Gary L. McCoy**

**Cole W. Litton**

**Air Force Avionics Laboratory  
Wright-Patterson AFB, Ohio**

Identification of Impurity Complexes in Gallium Arsenide  
Device Material by High Resolution Magneto-Photoluminescence

Abstract

Advanced avionics systems under development or proposed for future applications rely heavily on the capabilities of gallium arsenide (GaAs) as an electromagnetic material. Many of the characterization techniques applicable to silicon have required considerable refinement for GaAs and other more complicated compound semiconductors. One such technique is laser-pumped photoluminescence with and without applied external magnetic and stress fields. This measurement involves exciting electrons in the material using low power laser radiation and observing the light emitted by the electrons as they relax. This emission can be used to characterize impurities and defects since both create distinguishable electronic states. Many impurity states in GaAs have been investigated in depth and are well understood.

This study concerns five less understood transitions which we have investigated. These systems are not identifiable with any simple impurity transitions having similar binding energies. When perturbing fields are applied, differences in the behavior of these transitions and simple impurity transitions are observed. Based on these effects, models have been developed to explain the sources of these transitions. The model currently proposed involves a complicated molecule-like arrangement of an anti-site defect and nearby impurities. This measurement is the first experimental verification of the existence of such defects.

The development of high frequency or high power devices could be limited by these inherent defects which cannot be eliminated by further purification processes. Our research effort is motivated by the need to understand and eliminate or control such defects in the demanding environment of advanced Air Force avionics devices.

## Introduction

The feasibility and economic attractiveness of many future Air Force Avionics and ground-based electronics systems require the development of new, smaller, lighter, more inexpensive, and longer lived electronic devices. Other systems, less critically dependent on the development of new devices, will derive tremendous cost and performance benefits from such developments. Phased array radar systems, for example, offer vast improvements in performance over conventional radar systems, but their implementation is generally limited to frequencies below about 8 GHz primarily because of a lack of suitable microwave power devices. Developments leading to improved power and efficiency of devices for use in phased array radar systems would also have a revolutionary impact on other systems, such as satellite communication transmitters, for example. Similar developments would also address the far-reaching requirements for electromagnetic warfare systems, whose designs encompass digital information processing speeds currently impossible to achieve and even beyond the projected optimum capabilities of silicon technology.

In each of these specific systems, it has been the potential performance of gallium arsenide devices which has permitted the prediction of solutions for critical design problems. Laboratory feasibility experiments on the performance of GaAs field effect transistors have indicated that this device is one likely solution to technological roadblocks limiting incorporation into our inventory of many of the advanced electronic systems discussed. Such experimentation has also demonstrated that the ultimate performance of FET's, and of other new devices being developed, depends directly on the success with which materials can be produced in a carefully controlled and reproducible manner.

## Materials for Device Technology

The establishment of a sound technology base allowing reliable and reproducible material synthesis requires a basic understanding of the material physics, including the effects of foreign impurities, host defects and complexes involving both impurities and defects. Native defects, or crystalline lattice imperfections, can interact with intentionally introduced dopants to form neutral centers. It is also possible for unintentional residual acceptors to compensate intentionally added donors. In either case, the resulting electrical performance of the material will differ from the

desired design parameters and will adversely affect device performance.

A major thrust of our research effort is the characterization of such residual compensating centers, either defects or impurities. Great care both in sample growth and preparation and in the application of sophisticated measurement techniques is required to complete this thrust.

The effective-mass-like donors in III-V binary and in several of the III-V ternary systems are very weakly bound. The chemical shifts and central cell corrections which allow various impurities and defects to be differentiated in terms of their characteristic energy separations are small. This requires low residual concentrations to prevent concentration broadening and merging of the impurity levels. Sophisticated crystal growth procedures are required to control the residual impurities and defects at an acceptably low level to permit effective controlled doping. Parameters, such as the purity of growth materials, temperature gradients within the growth regions, growth rates, dopant diffusion coefficients, and perhaps many not yet identified, affect the success of such crystal growth efforts. Once the residual impurities and defects have been controlled at an acceptably low level, dopants can be added to the growing system intentionally to obtain uncompensated and uniformly doped material. Controlled doping experiments with known donors must also be in the low concentration range ( $N_D < 5 \times 10^{14} \text{cm}^{-3}$ ) to permit identification of specific donors; this represents a maximum of one dopant atom for each  $10^{10}$  host atoms.

Our characterization measurements strive to gain an understanding of the detailed nature of defects, impurities, and their interactions, so that this information can be used by growers to determine the optimized conditions for production of material with desired characteristics.

### Characterization Techniques

The electrical properties of semiconductors have a long history of extensive investigation. Many of the basic properties of these device materials were determined from electrical measurements. As the investigations of semiconductors were extended to some of the larger band gap materials electrical measurements were not as readily applicable. This, coupled with the understanding of excitons and their contribution to the elucidation of material properties in the 1960's, led to a wide application of optical studies to

semiconductor materials. It was found that these materials reflect, absorb, disperse, scatter and radiate light and in general, interact strongly with the electromagnetic radiation field. Because of this strong interaction many of the fundamental properties of these materials, such as their energy band gaps, activation energies of defects and foreign impurities, effective mass parameters, refractive indices, dielectric functions, exciton binding energies and lattice vibration frequencies, can be determined from optical experiments. These experiments cover the electromagnetic spectrum, ranging from the vacuum ultraviolet to the far infrared. Over the past two decades, optical spectroscopy has been increasingly employed for the study and measurement of semiconductor properties and has ultimately become a very powerful experimental tool.

Intense photoluminescence is observed in many semiconductors at low temperatures. When analyzed spectrally, this photoluminescence provides an extensive source of experimental data which contributes to the ultimate identification of the electronic states of impurities and defects in these semiconductors. Many sharp lines appear in such spectra, particularly from bound excitons, which provide a "finger print" of the impurities and defects which are present in the semiconductor lattice.

The technique of high resolution optical absorption, reflection and photoluminescence spectroscopy has been extensively used to analyse the intrinsic energy band parameters of semiconductors, as well as their impurity and defect states. Intrinsic or free exciton formation is observed in most well formed crystal structures when optically excited with the proper energy and at cryogenic temperatures. Examination of the behavior of free excitons in such crystals has led to a great deal of success in understanding the intrinsic band structure of semiconductors. Bound excitons have been applied equally successfully in probing the impurity and defect structure of many of these same materials.

With the advent of the laser as an exciting source, optical studies have become even more rewarding, particularly when non-linear effects are being investigated. They are also invaluable as exciting sources for high resolution photoluminescence studies.

Our experimental apparatus for high resolution spectroscopy is shown in Fig 1. In these experiments the sample is mounted in a liquid helium Dewar attached to a vacuum pumping system



permitting temperatures near  $1^{\circ}\text{K}$  to be realized. The Dewar may also be placed between the poles of a magnet permitting magneto-optical studies to be made. The optical source is tailored to the specific materials being investigated. For our photoluminescence measurements, we employ a 200 mW krypton ion laser with principal laser radiation at 647.1 nm. The transmitted, reflected, or emitted light may then be analyzed with a high resolution spectrograph. The heart of the spectrograph is the reflection grating selected to give optimum data for the particular material under investigation. The specific design parameters for our spectrograph have been optimized for investigating GaAs. The spectrograph has a four meter focal length and employs a 4 inch square grating with 2160 grooves/mm blazed at  $32.7^{\circ}$ . This design gives a dispersion of approximately 0.54Å/mm in first order in the free exciton spectral region of GaAs. Theoretical spectral energy resolution of  $0.3\text{ cm}^{-1}$  is achievable with this instrument. It may be employed with either photographic recording or electronic recording of the optical data.

### Photoluminescence Spectra

The photoluminescence process in the intrinsic region is difficult to quantitatively analyze. In the case of absorption and reflection experiments broad band illumination is used generally at relatively low intensities. This maintains the crystal in thermal equilibrium. The complications in the theory result from uncertainty in the proper model for the dielectric function and the proper surface boundary conditions. These same problems are present in the photoluminescent process with a number of additional problems. Exciting intensities are usually greater in the case of photoluminescence studies with laser excitation most generally used. As a result the crystal may not be in thermal equilibrium.

Surface recombination as well as bulk and surface scattering have great influence on the photoluminescent results and for the most part are not quantitatively known. The interpretation of intrinsic photoluminescent spectra is in need of quantitative theory to yield as much reliable information as is obtained from absorption and reflection spectra.

These difficulties notwithstanding, considerable progress has been, and is being, made in the identification of luminescence centers in gallium arsenide. The work described in this paper represents one part of our total effort to develop photoluminescence measurement techniques for use in GaAs characterization.

During the past four years, over 800 samples of GaAs have been characterized in our facility. We have focussed our attention on the identification of shallow, or loosely bound, impurities or defects with energy levels lying close to either the valence or conduction bands in the material. These levels can be detected when electrons experience relaxation transitions involving the levels and the opposite energy band. For example when an electron, previously pumped by the laser radiation from an acceptor impurity level up to the conduction band, relaxes back down to the impurity level it emits a photon with an energy equal to the difference between its initial and final states. A similar emission can be observed when an electron relaxes from a donor level down to the valence band. The typical emission seen when this transition takes place is labeled in Figure 2. The line is typically broad, which reflects the energy uncertainty associated with an electron in the valence band of a semiconductor. A second, and much sharper, set of lines results from transitions involving excitons bound to shallow impurities. In this context, an exciton is a hydrogen-like molecule formed by the coulombic interaction between a free electron and a "hole". When this system is formed in the presence of an impurity, the allowed electron energy levels become very sharp with widths typically on the order of  $0.1\text{cm}^{-1}$ . The bulk of our research effort has involved the measurement of these very sharp-line transitions. Typical donor and acceptor bound exciton lines are also indicated in the data of Figure 2. Our work in this area has been described in several previous publications and symposia presentations (References 1-16).

#### Impurity Complexes

Most recently, we have been investigating the behavior of five transitions noticeably different from the simpler transitions discussed earlier. The five lines are marked A through E in Figure 2, and the measured energy of each transition is also noted. As can be seen in that figure, the transitions appear to have energy widths similar to bound excitons and considerably narrower than the transitions involving band states. It can also be observed that the energies of the transitions seem to indicate rather loosely bound levels.

Greater insight into the nature of the states involved in these transitions can be gained by observing their behavior in the presence of external perturbing fields. Our facility permits the application of well controlled magnetic fields up to 45,000 gauss, and recently, we have begun exploiting

stress fields of up to  $400 \text{ g/mm}^2$  which can be created during sample growth or mounting. Interactions between the mobile charge carriers (electrons and holes) and the magnetic field causes measurable changes in the energies of initial and final states involved in the transitions. Similarly lattice perturbations due to applied stresses similarly create fields which alter the energies of initial and final transition states. The result of perturbations in the energies of the carrier states is reflected by changes, generally encompassing energy shifts and line splitting, in the luminescence spectra. The behavior of the five specified lines in the presence of magnetic fields is indicated in Figure 3. The shift in the "center of mass" of transitions has been removed in order to emphasize the nature of splitting as a function of applied magnetic fields. As can be observed the splitting over this range of fields is linear (Zeeman effect); while the diamagnetic shift not shown here is generally proportional to higher order terms (principally field intensity squared) and is usually observed as an increase in the mean transition energy with applied field.

Our analysis of the multiplicity of the lines in magnetic fields, of the symmetry of the splitting patterns, of the relative amplitudes of the single lines in each pattern, and of the magnitudes of the energy splittings has identified the source of each of these observations as a transition between a state involving an unpaired electron with one involving an unpaired hole. Available data on complexes A, C, and E is relatively complete. Complexes B and D, however, have been observed less frequently and neither is as intense as the others, hence conclusions about these lines are more tentative. Calculation of the effective Lande splitting factors for these complexes has determined that in all cases the electrons involved behave comparably to those observed with the normal bound exciton transitions which have been well studied ( $g_e = -0.5$ ). For complexes A, E, and probably B, effective Lande factors determined for the associated holes are also similar to those measured for other excitonic systems,  $\kappa = +.5$ . For complexes C and probably D, however, a considerably larger hole splitting factor is required to explain the observed splitting; the value for complex C being  $\kappa = +2.0$ .

The behavior of these complexes in the presence of an applied stress is shown in Figure 4. Also included in Figure 4, for reference, is the observed stress field behavior of the shallow impurity bound excitons. Applied stress generally results in a strain splitting of the valence band

(hole) states. In the exciton systems for both acceptors and donors, the magnitude of this splitting is seen to be relatively large. For the five complexes being investigated, such splitting is non-existent in C, D and E (behavior of complex D is less certain) and only about half as large in A and B. This observation requires explanations which do not involve hole states such as would be present in bound exciton or shallow acceptor impurities.

In our analysis of the body of data available concerning the five transitions of interest, we have applied a process of elimination to arrive at the model we feel most likely accounts for our observations. Simple impurity-to-band transitions have been eliminated due to the narrow energy widths of the observed lines. Impurity bound excitons have been eliminated due to well-documented identification of such transitions for all available impurity species (References 16 and 17, for example) and by the unusual behavior of the lines in strain field environments. The next simplest complexes which can be imagined in a semiconductor are indicated schematically in Figure 5. Of these three possibilities the neutral donor-neutral acceptor complex (Figure 5c) is considered least likely since more complicated splitting behavior would be expected in a strain field and since splitting in zero field environments due to exchange interactions between initial states might reasonably be expected. The double acceptor-neutral donor complex (Figure 5a) is also less likely since the observed magnetic field behavior is much less complex than what would reasonably be expected due to the complicated initial state of the transition.

The double donor-neutral acceptor complex (Figure 5b) can be employed to explain all aspects of the data we have collected, with the single stipulation that the acceptor involved is a relatively tightly bound impurity. Our observation is further supported by recent theoretical work reported by Dr. Van Vechten at IBM (Reference 18) in which he has predicted that complexes involving anti-site defects should be relatively common due to the growth conditions for GaAs. Anti-site defects are crystalline imperfections in which one specie of the compound material occupies a lattice position in which the other atomic specie should normally be found. In gallium arsenide, arsenic atoms sitting on gallium sites constitute anti-site defects which would behave like double donor impurities. Our observation of photoluminescence transitions which support this prediction are the first experimental verification of their existence in GaAs.

### Implications for Device Development

The development of non-destructive characterization techniques and their application to the understanding of materials for advanced device applications are important contributions to the technology base from which future systems will evolve. Identification and understanding of defect states in gallium arsenide provide important information affecting decisions concerning the directions of device development efforts. As control of unwanted impurities in gallium arsenide becomes increasingly well-established, ultimate performance characteristics for GaAs devices will become more dependent upon inherent defects in the material. The understanding of such defects which evolves from the present work will provide the basis for extension of future technology to meet the ever increasing demands confronting Air Force electronic systems.

### References

1. D. C. Reynolds, C. W. Litton, T. C. Collins, S. B. Nam, and C. M. Wolfe, Phys Rev B12, 5723 (1975).
2. S. B. Nam, D. C. Reynolds, and C. W. Litton, Proc 1975 International Conf of Luminescence, North Holland Publishing Co., 1976.
3. D. C. Reynolds, C. W. Litton, R. J. Almassy, S. B. Nam, and P. J. Dean, Phys Rev B13, 2507 (1976).
4. S. B. Nam, D. C. Reynolds, C. W. Litton, T. C. Collins, and P. J. Dean, Phys Rev B13, 1643 (1976).
5. S. B. Nam, D. C. Reynolds, C. W. Litton, R. J. Almassy, T. C. Collins, and C. M. Wolfe, Phys Rev B13, 761 (1976).
6. R. J. Almassy, D. C. Reynolds, C. W. Litton, K. K. Bajaj, and D. C. Look, J. Elec. Matls 7:2, 263 (1978).
7. D. Kniola, T. C. Collins, S. B. Nam, D. C. Reynolds, C. W. Litton, and C. M. Wolfe, Bulletin Amer Phys Soc 20:3, 362 (1975).
8. T. C. Collins, D. Kniola, S. B. Nam, D. C. Reynolds, C. W. Litton, and P.J. Dean, Bulletin Amer Phys Soc 20:3, 362 (1975).
9. D. C. Reynolds, C. W. Litton, T. C. Collins, S. B. Nam, and C. M. Wolfe, Bulletin Amer Phys Soc 20:3, 362 (1975).
10. C. W. Litton, D. C. Reynolds, J. H. Gorrell, T. C. Collins, and C. M. Wolfe, Bulletin Amer Phys Soc 20:3, 362 (1975).
11. S. B. Nam, D. C. Reynolds, C. W. Litton, R. J. Almassy, and C. M. Wolfe, Bulletin Amer Phys Soc 21:3, 253 (1976).
12. R. J. Almassy, D. C. Reynolds, C. W. Litton, S. B. Nam, and C. M. Wolfe, Bulletin Amer Phys Soc 21:3, 253 (1976).
13. C. W. Litton, R. J. Almassy, D. C. Reynolds, S. B. Nam, and C. M. Wolfe, Bulletin Amer Phys Soc 21:3, 253 (1976).
14. D. C. Reynolds, R. J. Almassy, C. W. Litton and K. K. Bajaj, Bulletin Amer Phys Soc 22:3, 201 (1977).

15. R. J. Almassy, D. C. Reynolds, C. W. Litton, and K. K. Bajaj, Bulletin Amer Phys Soc 23:3, 201 (1978).
16. Y. S. Park, D. C. Reynolds, R. J. Almassy, and G. L. McCoy, Bulletin Amer Phys Soc 23:3, 224 (1978).
17. D. J. Asken, P. J. Dean, P. T. J. Hurle, T. B. Mullins, A. M. White, and P. D. Greene, J. Phys Chem Solids 36, 104 (1975).
18. J. A. Van Vechten, J. Electrochem Soc 122, 423 (1975).

1. Liquid helium dewar with immersed sample.
2. 45 kG DC Electromagnet.
3. Light-gathering optics.
4. Light-positioning optics.
5. Spectrometer entrance slit.
6. Zirconium Arc Lamp (reflection).
7. Krypton laser (luminescence).

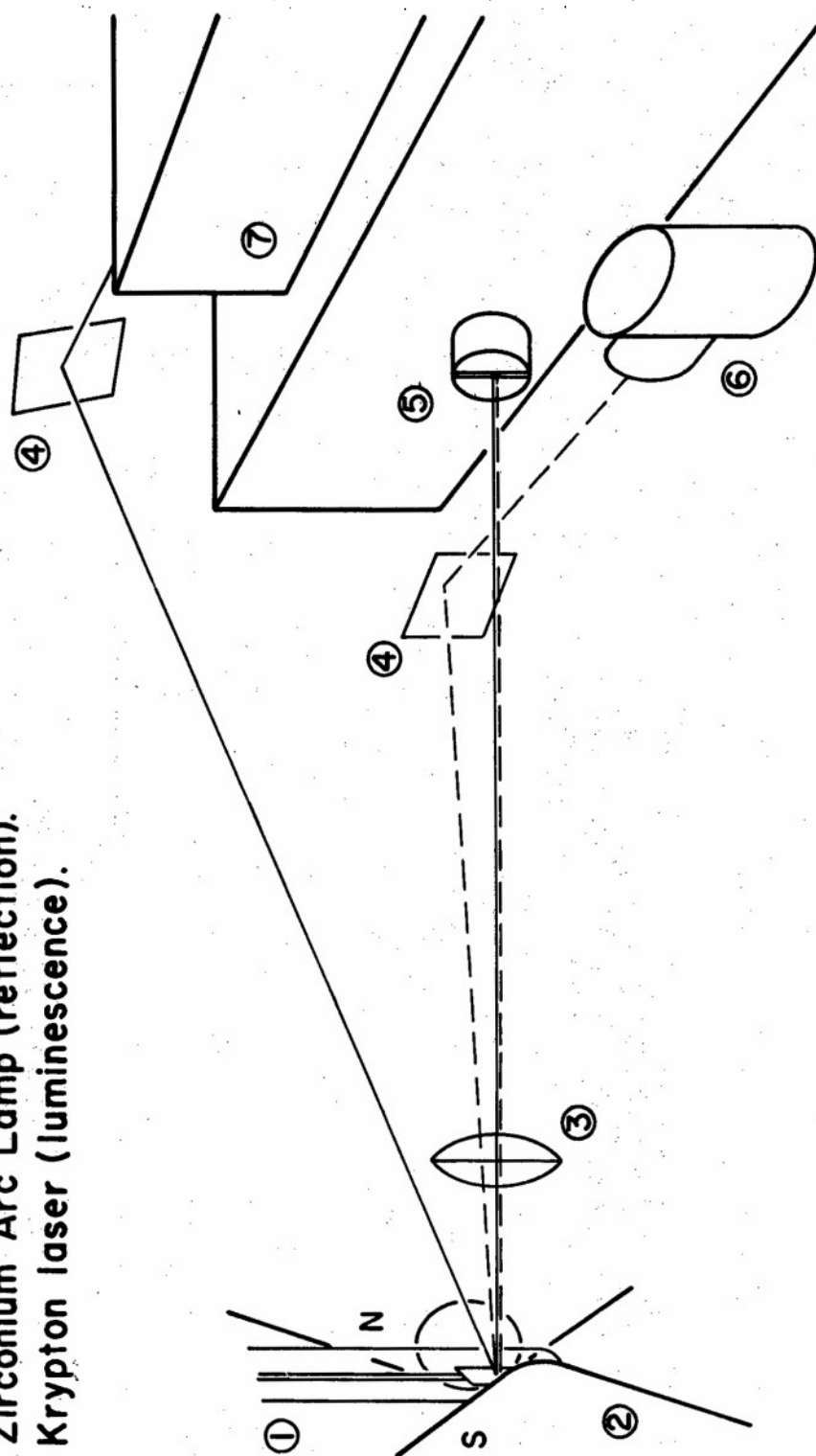


FIGURE 1



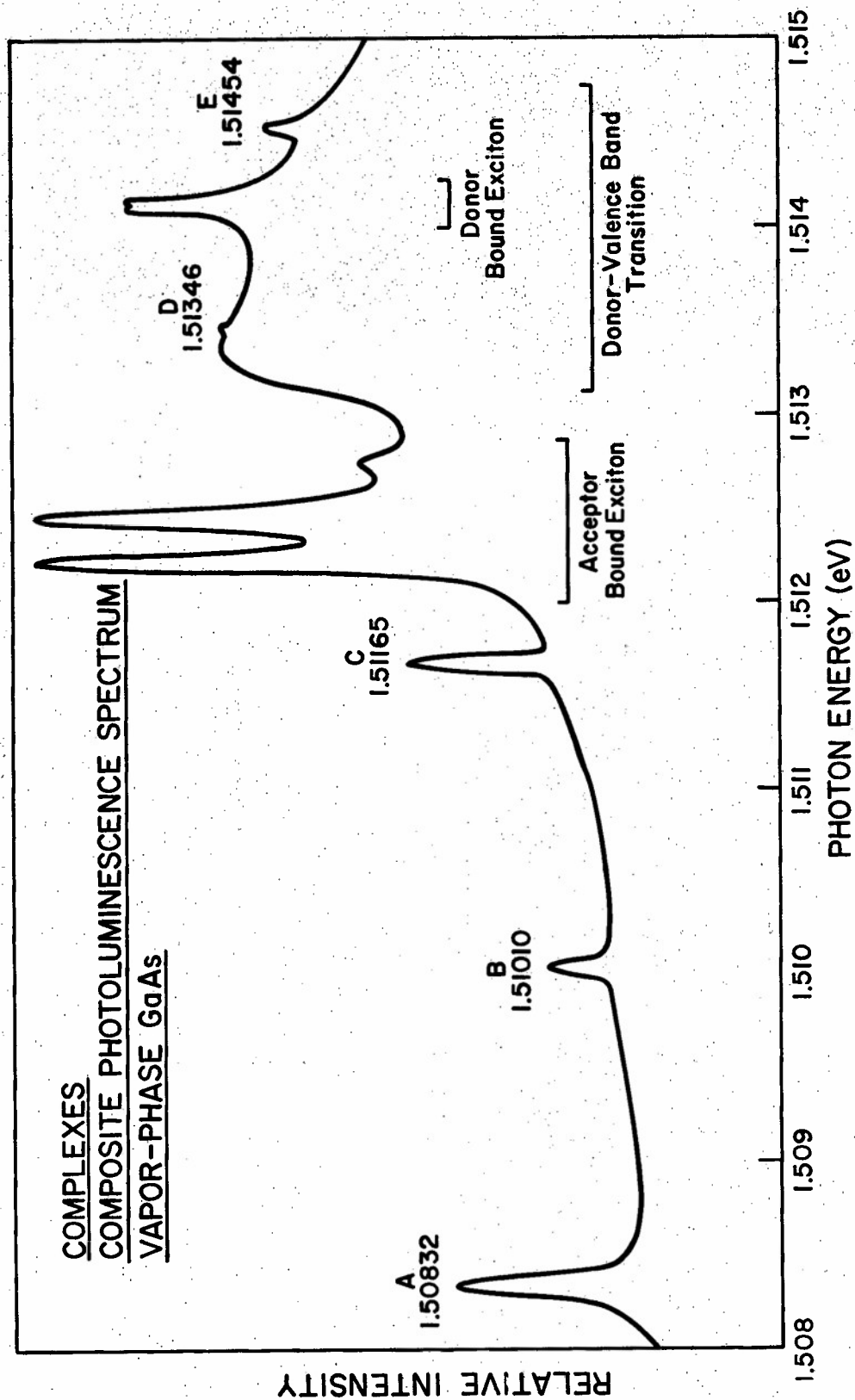
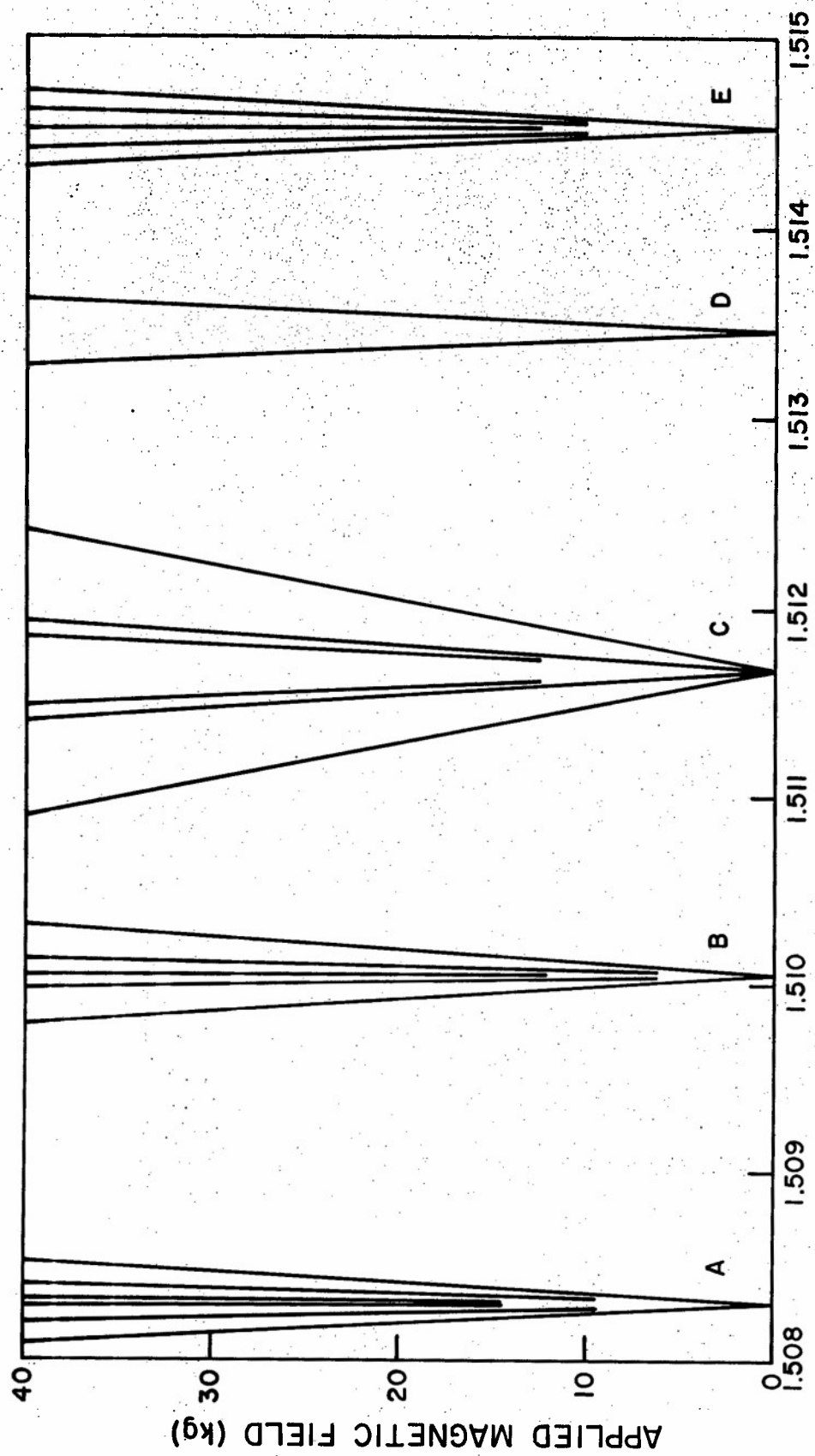
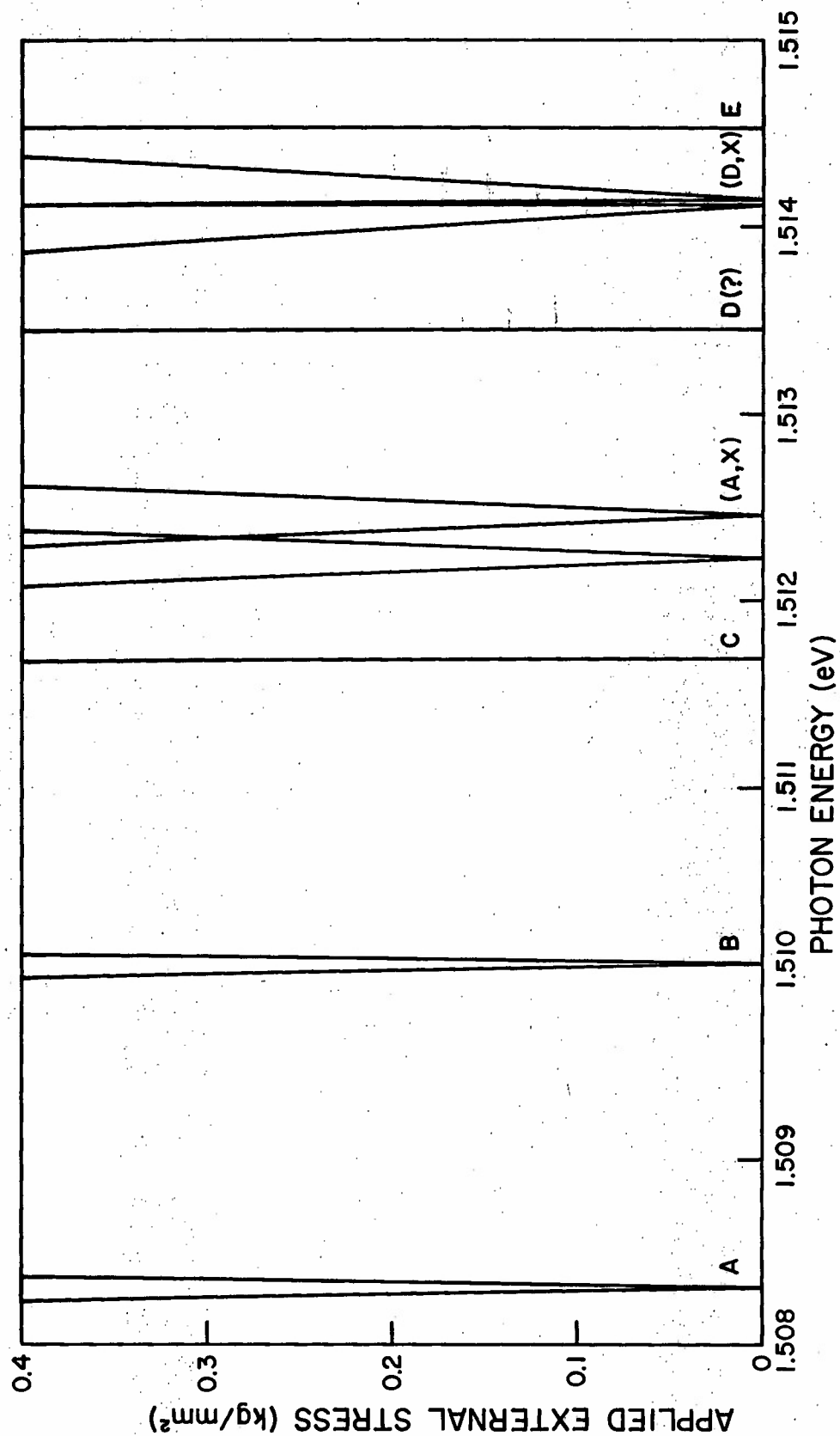


FIGURE 2



GaAs COMPLEXES, LINEAR MAGNETIC FIELD SPLITTING (Diamagnetic shift removed)

FIGURE 3



GaAs COMPLEXES, STRAIN FIELD SPLITTING

FIGURE 4

Double Acceptor Donor	Double Donor Acceptor	Donor Acceptor
<u>Initial state</u> $\begin{array}{c} \text{---} J = \frac{1}{2} \\ + \text{---} J = \frac{3}{2} \\ \ominus \text{---} J = \frac{5}{2} \\ \oplus \end{array}$	<u>Initial state</u> $\begin{array}{c} \text{---} J = \frac{3}{2} \\ \oplus \text{---} \\ \oplus \ominus \end{array}$	<u>Initial state</u> $\begin{array}{c} \text{---} J = 2 \\ \oplus \text{---} \\ \oplus \text{---} J = 1 \\ \ominus \end{array}$
<u>Final state</u> $\begin{array}{c} + \text{---} J = \frac{3}{2} \\ \ominus \oplus \end{array}$	<u>Final state</u> $\begin{array}{c} \text{---} J = \frac{1}{2} \\ \oplus \text{---} \\ \oplus \ominus \end{array}$	<u>Final state</u> $\begin{array}{c} \text{---} J = 0 \\ \oplus \ominus \end{array}$

(a)
(b)
(c)

FIGURE 5

### Biographical Sketch

Major Robert J. Almassy was born in Flint, Michigan on September 20, 1942. He graduated from the United States Military Academy, West Point, New York, in 1964, and was commissioned in the US Air Force. He completed graduate studies at the Air Force Institute of Technology Resident School of Engineering, where he received a Master's Degree with distinction in Nuclear Engineering in 1969 and completed academic requirements for the Ph.D. Degree in Aerospace (Electrical) Engineering in 1975. He is currently completing thesis research requirements for award of that degree. His professional education includes graduation from the Armed Forces Air Intelligence Training Center (with honors), Squadron Officers' School, Air Force Command and Staff College, and the Industrial College of the Armed Forces.

His tours of duty have included assignments as intelligence officer, 15th Air Force Recon and Technical Squadron (SAC), 1965-1967; Assistant Professor of Physics, USAF Academy, 1969-1973; and Deputy Branch Chief, Electronics Research Branch, Air Force Avionics Laboratory, since 1975. His research interests have included solid state physics, laser optics, and currently, physics of electromagnetic materials. He has published 15 papers in these fields since 1970. He has received the Air Force Commendation Medal and is a member of the Optical Society of America, the American Institute of Physics, and Tau Beta Pi.

Mr. Donald C. Reynolds was born in Sioux City, Iowa on July 28, 1920. He graduated from Morningside College with a B. S. Degree in Physics in 1943. He served in the Army Air Corps during World War II as a Communications Officer. He received a M.S. Degree in physics from the University of Iowa in 1948.

In 1948 he joined the research staff at Battelle Memorial Institute where he spent four years. In 1952 he went to the Aerospace Research Laboratories at WPAFB where he became Director of the Solid State Research Laboratory. In 1975 he joined the Air Force Avionics Laboratory as a Senior Scientist. He has ten patents and 82 published papers. He is a member of Sigma Pi Sigma, Sigma Xi and a Fellow of the American Physical Society.

Gary L. McCoy was born in Lovington, Illinois on May 8, 1943. He graduated with honors from the University of Illinois College of Liberal Arts and Sciences in 1965, receiving a B.S. Degree in physics.

In August, 1967 he was employed by the Air Force Avionics Laboratory, where he became involved with the solid state microwave device technology in general and the epitaxial growth of gallium arsenide in particular. While in this position he attended graduate courses in physics and electronics from Ohio State University. He served as Chief of the Microwave Sources Group from Nov 1973 to Dec 1975, where he was responsible for contractual and in-house research and development in the area of solid state and thermionic microwave power sources. In December 1975 he joined the Electronic Technology Branch where he has since been active in research on epitaxial growth techniques for gallium arsenide compounds.

Cole W. Litton was born on September 29, 1932, in Memphis, Tennessee. He received his undergraduate and part of his graduate education in physics at the University of Tennessee and continued graduate education in Theoretical Physics (Solid State and Molecular Quantum Mechanics) at Uppsala University in Sweden (1958-1959) and at Reading University, Reading, England, where he completed academic and thesis research requirements for the Ph.D. in physics (1968-1969). He is currently completing dissertation requirements for that degree.

He joined the Aerospace Research Laboratories in 1957, after Air Force military assignments in Rocket and Ballistic Research and Electronic Analog Computer Research at Wright-Patterson AFB, Ohio. From 1971 to 1975 he served as Group Leader, Solid State Research Laboratory. Since 1975 he has been assigned as a Research Physicist, Electronic Research Branch, Air Force Avionics Laboratory. He is involved in materials research aimed at improving semiconductor materials for microwave and opto-electronic device applications. He has published more than 75 scientific papers in the field of semiconductor materials. He is a Fellow of the American and British Physical Societies, a Senior Member of the Optical Society of America, and a member of Sigma Pi Sigma and Sigma Xi.

MICROCIRCUIT ANALYSIS TECHNIQUES USING FIELD EFFECT LIQUID CRYSTALS

BY

Daniel J. Burns, USAF

Reliability and Compatability Division

Rome Air Development Center  
Griffiss Air Force Base , NY

## Microcircuit Analysis Techniques Using Field Effect Liquid Crystals

### Abstract

Recent advances of microelectronics technology have resulted in the availability of extremely sophisticated and complex devices. Large scale integration (LSI) circuits achieve a higher functional density with better performance and potentially much lower costs. The reliability of these devices is a key factor in their widespread implementation in military systems. However, the complexity of these parts makes reliability analysis of these devices very difficult. New techniques are required for product evaluation, electrical characterization, failure analysis and reliability assurance.

The new analysis techniques described in this paper promise to greatly reduce the time and effort required to pinpoint the cause of failure in LSI devices which have failed in application or in laboratory testing. These techniques use liquid crystal display technology to allow the analyst to observe with a standard optical microscope the flow of data in a complex circuit as it operates.

One method produces an optical display of selected parts of a complex circuit by controlling the electric fields produced in a layer of liquid crystal on the circuit. This is accomplished by special modification of the external control inputs to the circuit as the circuit is operated. The method is useful in design analysis and chip mapping where functional blocks and individual cells must be physically located in a large circuit. Another method uses this modified timing and an externally applied, synchronous electric field to produce a static display of dynamic logic levels present at internal circuit nodes as the device is operated at a high clock rate. This method is useful for nondestructive testing of internal circuit paths and for analysis of low voltage technologies.

Many microcircuit manufacturers and major users who maintain microcircuit reliability analysis laboratories are now implementing and evaluating these analysis techniques. They are being used at RADC in the reliability assessment of new and advanced microcircuit technologies.



## Introduction

The availability of high reliability microcircuits to the military electronics systems designer is assured through a system of procurement specification documents and by rigorous reliability evaluations of new technologies as they emerge. Innovations in integrated circuit manufacturing methods and improvements in process controls have resulted in microcircuits which contain literally thousands of active elements on silicon chips measuring less than a centimeter on a side. A key task in the reliability assessment of these complex large scale integration (LSI) devices is the development of techniques which allow in-depth design analysis and accurate failure analysis of parts which have failed during laboratory testing or in field use. The identification of contributing failure mechanisms is necessary in order to recommend device changes, process changes or special screen tests which will eliminate the specific problem in future devices.

Highly complex devices pose a major problem to the analyst in failure verification and design analysis. Established techniques rely on external parametric measurements and internal electrical measurements made in conjunction with an analysis of the schematic diagram and physical layout of the circuit. Circuit diagrams have generally been available for small scale integration chips, and can be easily verified by optical inspection of the silicon chip. The number of active elements for these types of circuits is typically less than a couple hundred. Electrical die probing with micromanipulators and scanning electron microscope or optical inspection techniques are used routinely to isolate the cause of failure in such circuits. However, these techniques alone are not adequate or practical for circuits ranging up to 5,000 active elements. Circuit diagrams for these complex circuits are not generally available (or up to date) and even the correlation of circuit function to physical location on these devices becomes a formidable task. Such information as well as other details of circuit implementation may not be available to the analyst. Under these conditions, the only practical approach to a meaningful analysis is with a combination of software fault isolation techniques and circuit component level analysis carried out in a relatively small portion of the circuit. First the malfunction must be isolated to a particular part of the circuit and then that part must be analyzed in detail using techniques similar to those used now as well as new techniques which are especially suited for nondestructive testing of complex, densely packed LSI

circuits.

The analysis techniques described in this paper represent new improvements to a novel analysis technique originally described by D. Channin<sup>1</sup> for observing the operation of integrated circuits using field effect liquid crystals and an optical microscope. Channin's technique is capable of detecting localized heating, logical "stuck at" faults, and for observing data propagating through operating circuits at low frequencies (approximately 5 Hz).

The present work was undertaken to apply the basic technique to the problem of determining the logic levels present at the internal circuit nodes of a complex LSI device during selected digital states as the device under test (DUT) is operated at a high clock rate in some predetermined test sequence. The resulting techniques take advantage of the RMS threshold voltage dependence of the electro-optic effect in the liquid crystal to produce a display which is similar to that obtained using scanning electron microscope (SEM) techniques with beam strobing or synchronous DUT bias.<sup>2,3,4</sup>

These techniques are capable of gate and transistor level analysis and can aid in fault isolation and failure analysis. They are relatively simple and inexpensive to implement and have been used as an alternative to destructive mechanical die probing and as a complementary technique to SEM voltage contrast methods for observing device operation and determining the physical location of various circuit functional blocks. They do not require complex raster scanning or sample and hold electronics as do some SEM and laser photostan analysis techniques.

A description of chip display cell preparation is given and methods for generating the required DUT control are discussed. A versatile microcomputer based system for DUT control has been implemented and used for these LCD investigations as well as synchronous bias SEM analyses.<sup>5</sup> Typical results are shown which illustrate applications including visual determination of metallization discontinuities, observation of data associated with selected digital states and memory chip mapping.

#### Display Cell Preparation

These LCD techniques employ an electro-optic display effect<sup>6</sup> which depends on localized changes in the refractive index of a thin layer of liquid crystals. The integrated circuit display cell described by Channin<sup>1</sup> uses the DUT

surface with scratch protection layer intact and a thin glass coverplate to confine a thin layer of nematic liquid crystal material such as MBBA<sup>7</sup> as shown in the cross-section in Figure 1. The required vertical molecular orientation can be promoted in the liquid crystal by first treating the surfaces with a surfactant solution. Excellent results have also been obtained using a surface treatment described by Janning<sup>8</sup> for the coverplate which uses a thin, transparent Au layer which is sputtered onto the coverplate surface. The coverplate must be cut with a wafer scribe to fit within the perimeter defined by the bonding wires so that it does not interfere with the electrical connections to the device. A drop of liquid crystal is then placed on the device surface. The coverplate is then floated on the drop of liquid crystal. A typical prepared cell is shown in Figure 2.

The device is then fixtured under a standard microscope and viewed with vertical illumination. A polarizer is placed in the light path and another is placed in the viewing path and oriented at 90° to the first. The display effect cannot be observed without vertical illumination and properly oriented polarizers. After an analysis is completed, the liquid crystal can be removed by cleaning the device with acetone and the lecithin coating can be removed with Uresolve Plus<sup>R</sup>.

#### Display Cell Characteristics

The display cell formed as above is a field effect display, in contrast to the dynamic scattering display described by Salvo<sup>9</sup> for detecting defects in insulating films. When the scratch protection glass is left intact the cell shows no display effect for dc voltages as a result of surface charging (with a time constant of about 0.1 sec) within the display cell which reduces the vertical component of electric field in the liquid crystal below the threshold level. (When the glass is removed, dc voltages can be observed). When viewed through crossed polarizers, the device appears dark if no electrical bias is applied, as shown in Figure 3. Note that dust particles in the cell cause bright spots. These spots can be distinguished from active circuit elements since they do not change with the removal and application of bias. When bias is applied and the device is operated there is a bright display over those conductors carrying sufficiently high RMS voltages (4.5v RMS). The display is continuous for frequencies above 500 Hz to greater than 10 MHz. Figure 4 shows the display for a 14 stage binary counter (CMOS,  $V_{DD} = +10$  V)

clocked at a 10 MHz rate. The 14 D-type flip-flop stages are all toggling with a 50% duty cycle at different frequencies. The voltage waveforms carried by the signal conductors in each of the stages have the same RMS value (7.07 V) and are all displayed.

#### Device Control For A Selective Display

The display produced by the counter circuit shown in Figure 4 does not give information about the logic levels present on various conductor lines during a given digital state. The RMS voltage values are the result of an effective integration of the logic levels present during the period of a complete cycle through all of the 16384 individual digital states. The display is continuous because the complete cycle is repeated every 1.6+ ms for the 10 MHz clock rate used in this example. It is desirable, however, to produce a display which does give information about the logic levels present during individual digital states in the test cycle and also about the physical location of various circuit functional blocks, such as single flip-flops or clock bus lines.

A display which does provide the desired information is shown in Figure 5. The circuit is operated in quite a different manner to produce the selective display. The timing of state transitions in the test cycle has been modified such that the circuit "pauses" in two preselected states for a time much greater than the duration of any of the other states in the cycle. This modified timing effectively increases the duty cycles of two states in the test cycle and reduces the duty cycles of all the remaining states in the test cycle. As a result, the RMS voltage values on the conductors on the chip become largely a function of the logic levels present only during the two preselected states. The display contains a bright response only over those conductors which assume different logic levels in the two chosen states. This special test cycle timing is illustrated in Figure 6. In this manner a "reference" state (e.g. binary 0000) and a "selected" state (e.g. binary 1000) can be designated, and the logic levels present during any single selected state in the test cycle can be directly compared to those present during the reference state. The display in Figure 5 allows the analyst to easily determine the location of the fourth flip-flop cell and also to verify the correct logical content of the flip-flop during the selected state.

It is interesting to note that information very similar to SEM methods is obtained without a busy background of dc level information unrelated to the features of interest. This can simplify interpretation of the display for low magnification searching such as that required for chip mapping of a memory array or for circuit conductor tracing when the conductor path is distributed throughout large and widely separated areas on the chip.

The technique described above can be used to investigate a variety of circuit functions; shift registers, control logic and any circuitry which can be controlled in the required manner. The basic idea is to accentuate certain information by causing selected conductors to change logic levels at a near 50% duty cycle and to suppress other information by decreasing the duty cycle (and RMS value) of the logic levels associated with those states not to be displayed.

The control signals for producing the pauses in the periodic test cycle can be generated in a variety of ways. Analog delay circuits (e.g. one shots) or digital delays (e.g. counters) can be used to gate a clock input for many circuit functions. These approaches have the disadvantage that they require hardwired circuits which are unique for each circuit function and number of states in the test cycle and are not easily implemented when more than one control line is required. A more versatile approach which incorporates a small, one board microprocessor system to generate DUT control signals. The DUT timing diagram signals are converted to a sequence of bytes which are stored in the microcomputer's memory and outputted under software control. The appropriate pauses are thus easily programmed into the cycle and can be changed by the programmer or automatically by the program. Applications which use this additional capability will now be discussed. (The microcomputer used for this work was based on the 1802 CMOS device, with only 512 bytes of program storage. Total cost of the system was less than \$400.00).

### Applications and Results

A simple but very useful application of the LCD technique is to solve the problem of verifying continuity of conductor lines at internal nodes of small geometry LSI devices where mechanical die probing would be difficult at best. Figure 7 shows a display which identifies the exact location of electrical opens which were the result of corrosion. This device was a field failure. The circuit is

a 1024 bit PMOS static shift register. The opens occurred on clock bus lines and resulted in catastrophic failure. The portions of the conductor lines which are dark in Figure 7 are electrically not connected to the 1KHz input clock or the other two clock phases which are internally generated. Destructive mechanical die probing was not necessary in this case to identify the fail sites.

A task which occurs frequently in the analysis of LSI devices is chip mapping. For the case of a memory circuit, the binary address corresponding to each bit stored must be correlated to a physical memory cell location on the chip. This usually requires that the address decode circuitry be completely traced to identify cell locations. Low magnification searching with optical or SEM techniques can be tedious and time consuming. The task can be simplified considerably by using the LCD technique with the DUT under automatic control. Figure 8 illustrates the static display obtained by writing an alternate pattern of 1/0 into two bit locations; the binary "0" address as a reference and one other selected cell which is then easily identified. The memory array is easily mapped as the DUT controller is sequenced from one selected address to the next. The device shown is a CMOS 256 bit memory. Similar results have been obtained for an UV erasable ROM (2708, 8K bit) and other memory arrays.

Recent efforts have been directed at applying these LCD techniques to the analysis of a microprocessor device. The device selected was the 1802 device which is a CMOS circuit which can be operated on a single supply and could be easily tested in the same microcomputer system which was used for controlling other devices analyzed with these techniques. Much information can be generated by simply observing the LCD display as the microprocessor executes test programs which execute certain functions on the chip. However, it is desirable to inspect the data flow in the circuits throughout the chip during the intermediate steps in the machine cycles which time the execution of each instruction in the test software. This required the use of a second microcomputer system to synthesize the master clock and control signal inputs for the microcomputer containing the device being tested with a LCD display cell. Those control signals had to be specially timed to allow the reference state to selected state comparison which was used previously for smaller circuits.

Videotape recording is used to capture the displays

resulting from the execution of a test program which exercises certain portions of the device with different data and instructions. The controlling microcomputer can be programmed to dwell at one particular instruction in the test program or to sequence from one to the next, so that one state can be inspected for a long time or a long series of states can be recorded.

The following motion picture shows the display obtained for some typical test programs which exercise the microprocessor's machine cycle counter and decoder, a program counter register (R0), and finally the DATA (or accumulator) register.

( Motion picture running time approximately 5 minutes).

Detailed comparisons can be made of two states of the device and correlated to the execution of various instructions and physical locations on the chip. For example, a photomicrograph may be produced by making an exposure filtered in green and an exposure filtered in red, each with a different selected state. Those conductors which assume different logic levels during both of these selected states than the logic levels assumed during the reference state show in a third color. Thus data which changes from state to state as instruction execution proceeds can be highlighted. Those conductors which do not change from their initial values in the reference state do not light and thus do not interfere with the interpretation of the active portions of the display.

These techniques allow the analyst to correlate circuit function to physical location on the chip without the aid of a complete chip map and circuit schematic. The contents of internal registers and bus lines can be inspected for different states of the circuit. Improper operation can be detected by comparison between the displays for different states or by comparison to the display of a similar good device.

#### Biased Coverplate Method

Preliminary results have been obtained which have proven the feasibility of depositing a conductive layer of Au on the lower surface of the coverplate and making electrical contact to it to form a field plate. The field plate voltage can then be used to directly control the digital state selected for display. The advantages of this approach are that the weaker electric fields available on devices with small voltage swings can be aided by pulsing

the field plate. For example, a simple NAND gate device may be biased with a 4v square wave on one input. The conductive coverplate is biased with a 4v square wave 180 degrees out of phase with the input waveform. In the resulting display those conductors which carry logic levels out of phase with the fieldplate are imaged. This method also allows display of only the logic 0 conductors or only the logic 1 conductors for the selected state. The phase of the field plate waveform determines which logic level is displayed. Experiments to date have used a conductive epoxy to establish contact to the field plate on the lower surface of the coverplate. The epoxy is attacked by the liquid crystal and contact is eventually lost. Presently, experiments are being made with a fired on Au layer which provides a metal path around the edge of the coverplate to the top surface which can then be contacted from above with a micromanipulator probe. This biased coverplate method extends the technique to the lower voltage technologies such as NMOS and TTL.

### Conclusions

The LCD analysis techniques described give the analyst another tool which can be used routinely in addition to the many available techniques already being applied to the problems encountered in the analysis of complex digital devices. The materials required are commercially available and the equipment needed is likely to be present in the analysis laboratory or available at relatively low cost. The techniques are nondestructive and the analyst can easily remove the LCD cell after use and proceed to other steps such as die probing or SEM analysis.

The results which are obtained with these techniques are similar to those for SEM and laser photoexcitation techniques<sup>10</sup> which require beam modulation, T.V. raster scanning, and complex display electronics. Those latter techniques may represent a prohibitively high initial investment cost to the smaller laboratory and also require specially trained personnel to operate and maintain the required equipment.

The LCD display can be made to respond only to ac voltages when the chip overcoat glassivation is left intact, in contrast to SEM techniques which also image dc voltages. This feature is used to simplify the interpretation of the LCD display, especially when searching for small features at low magnification. The actual active display areas are high contrast, light on



dark and are confined to the immediate area above conductor lines on the surface of the circuit. This type of display is quite different from that obtained with photoexcitation and electron beam induced current (EBIC) techniques<sup>11</sup> which are used primarily to image p-n junctions. The LCD technique does not give structural information and cannot be used to identify the location of an inversion region, for example, as can some of the previously mentioned techniques. However, the display is easily correlated to the optical image of the circuit by simply rotating (uncrossing) one of the polarizers in the optical viewing system.

Finally, the implementation and interpretation of these LCD techniques are easily within the capabilities and constraints of the modestly equipped microcircuit analysis facility.

#### Acknowledgements

The author wishes to thank J. Bart, E. Doyle, Dr. M. W. Levi and C. Salvo for their many helpful discussions. Mr. B. Moore produced the Au sputtered coverplates used in this work. Mr. M. Wangler, Mr. G. Jakobcic and Mr. G. Sweet provided valuable assistance in debugging the microcomputer software and producing the photomicrograph illustrations in this paper. All of the above are with the Reliability Branch, RADC, Griffiss AFB, NY.

## References

1. D.J. Channin, "Liquid-Crystal Technique for Observing Integrated Circuit Operation," IEEE Transactions on Electron Devices, Oct 1974, pgs. 650-652.
2. D.L. Crosthwait and F.W. Ivy, "Voltage Contrast Methods for Semiconductor Device Failure Analysis," Scanning Electron Microscopy/1974 Proceedings of the Workshop on Failure Analysis and the SEM, IITRI, 1974.
3. B. Piwczyk and W. Siu, "Specialized Scanning Electron Microscopy Voltage Contrast Techniques for LSI Failure Analysis," Proceedings of the 1974 IEEE Reliability Physics Symposium, pgs. 49-53.
4. S.K. Behera and D.P. Speer, "A Procedure for the Evaluation and Failure Analysis of MOS Memory Circuits Using the Scanning Electron Microscope in Potential Contrast Mode," Proceedings of 1972 IEEE Reliability Physics Symposium, pgs. 5-11.
5. J. Bart, "Scanning Electron Microscopy for Complex Microcircuit Analysis," 1978 IEEE Reliability Physics Symposium Proceedings.
6. M.F. Schiekkel and K. Fahrenschon, "Deformation of Nematic Liquid Crystal Layers with Vertical Orientation in Electrical Fields," Appl. Phys. Lett., Vol. 19, No. 10, 15 Nov 71, pgs. 391-393.
7. Available from 3M Company, Visual Products Division, St. Paul MN and others.
8. J. L. Janning, "Surface Orientation for Liquid Crystals," Appl. Phys. Lett., Vol. 21, No. 4, 15 Aug 72, pgs. 173-174.
9. C.J. Salvo, "An Improved Approach to Locating Pinhole Defects in MOS and Bipolar Integrated Circuits Using Liquid Crystals," Proceedings of 1976 IEEE Reliability Physics Symposium, pgs. 263-274.
10. M. L. Levi, "An Investigation of Flaws in Complex CMOS Devices by a Scanning Photoexcitation Technique,"

Proceedings of 1977 Reliability Physics Symposium, pgs. 44-53.

11. J. R. Beal and L. Hamiter, Jr., "EBIC - A Valuable Tool for Semiconductor Evaluation and Failure Analysis," Proceedings of 1977 IEEE Reliability Physics Symposium, pgs. 61-69.

# INTEGRATED CIRCUIT LIQUID CRYSTAL DISPLAY

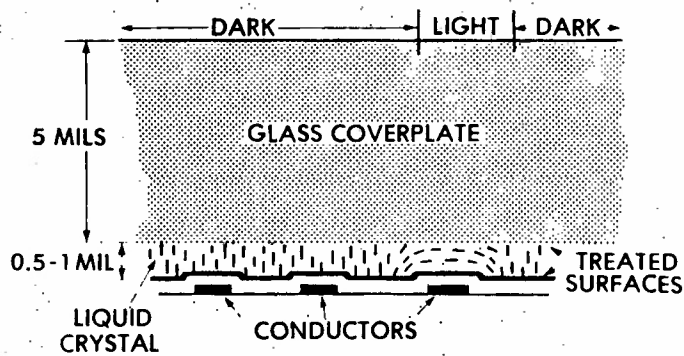


Figure 1

Cross-section of a display cell. The horizontal alignment in the liquid crystal above the third conductor on the right is in response to fringing fields from the underlying conductor.

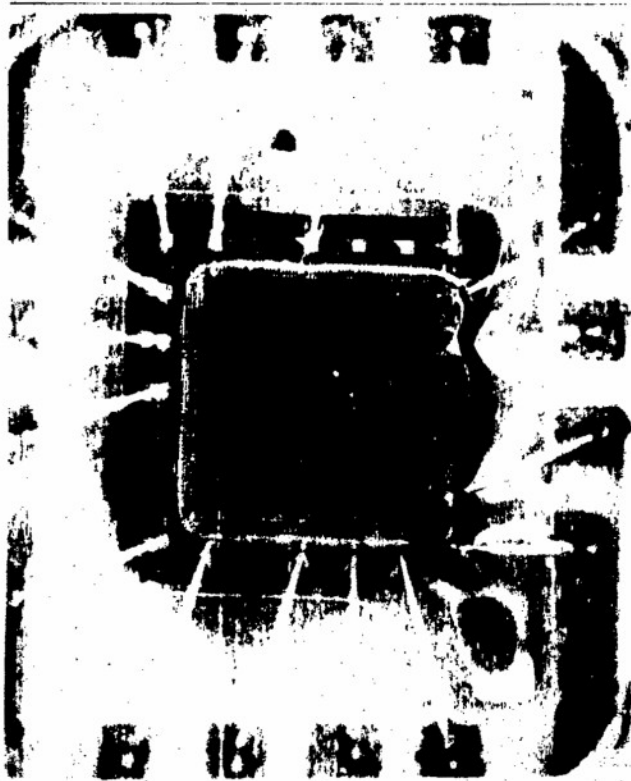


Figure 2

Display cell prepared on a CMOS binary counter. (4020).

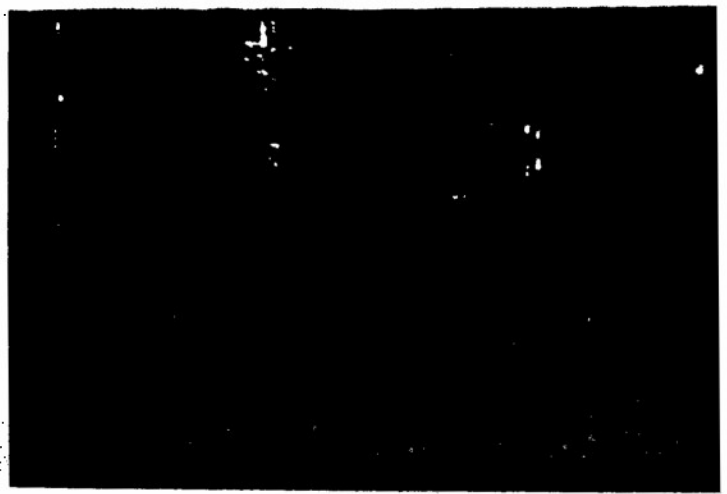


Figure 3

Cell appears dark with only dc bias (Vertical illumination).

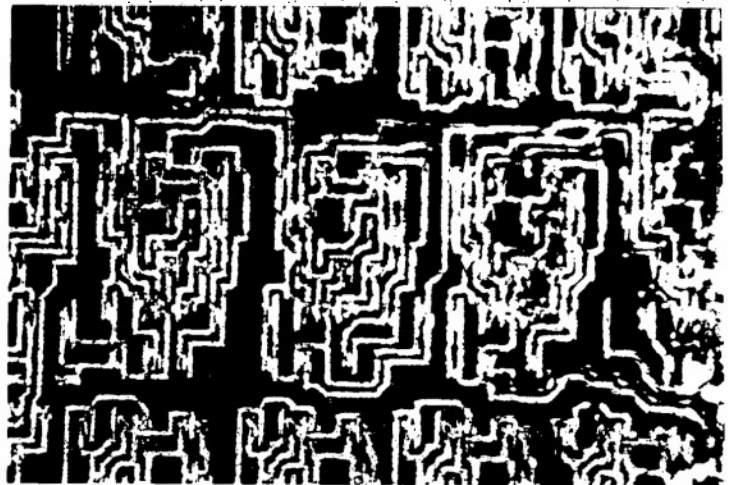


Figure 4

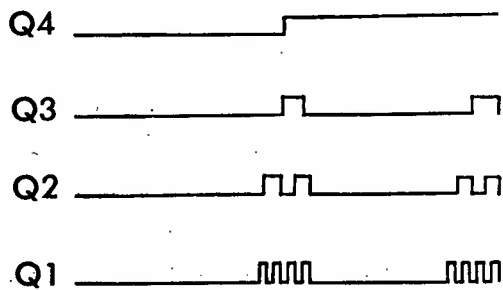
CMOS binary counter with 10MHz input clock frequency. All stages are displayed.



Figure 5

Selective display of seventh stage by comparing states "0" and "64".

## BINARY COUNTER WAVEFORMS MODIFIED STATE TIMING



DIGITAL STATE      0      1-7      8      9-15

CYCLE TIME ←----- 64T ----->

Figure 6

Control cycle timing for a selective display of fourth stage by comparing states "0" and "8".



Figure 7

Electrical opens on clock lines of this 1024 bit PMOS static shift register are identified by the discontinuous displays.

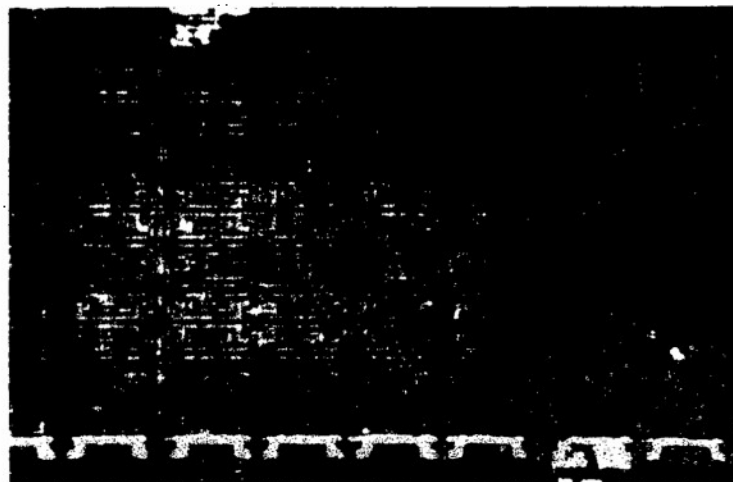


Figure 8

Reference memory cell location "0" is at lower right. Selected cell "81" is at upper left.

### Biographical Sketch

Daniel J. Burns was born in Grand Rapids, Michigan on April 7, 1950. He received a BEE degree from the University of Detroit, Detroit, MI in 1973 and the MSEE degree from Syracuse University, Syracuse, NY in 1978.

Since 1973 he has been with the Reliability Branch at Rome Air Development Center, Griffiss AFB, NY where his primary work involves microcircuit analysis in support of DOD systems. He has also worked on reliability evaluations of advanced microcircuit technologies and on specifications for microcircuit electrical overstress tolerance. He is currently engaged in development of techniques for analysis of complex devices using liquid crystals.

**SURFACE ACOUSTIC WAVE FREQUENCY SYNTHESIZER FOR JTIDS**

**BY**

**ALAN J. BUDREAU, ANDREW J. SLOBODNIK, JR., and PAUL H. CARR**

**Electromagnetic Sciences Division**

**Rome Air Development Center  
Deputy for Electronic Technology  
Hanscom AFB, Massachusetts 01731**

## Surface Acoustic Wave Frequency Synthesizer For JTIDS

### Abstract

Fast-hopping frequency synthesizers are essential to a variety of communication and data-link applications. A frequency synthesizer built as a feasibility demonstration for the Joint Tactical Information Distribution System (JTIDS) is described. Surface Acoustic Wave (SAW) technology was utilized to yield a design amenable to a compact, reliable, low cost final product. Although any of the standard approaches to frequency synthesis, i.e., phase-locked-loop oscillators, digital synthesis, and direct synthesis, may benefit from SAW components to reduce the size and cost, the direct synthesizer is the most appropriate for achieving fast frequency-hopping. The JTIDS terminals require sub-microsecond hopping. A mixing approach, in which the outputs of three direct synthesizers are mixed, was chosen to reduce the number of filters required. Advanced state-of-the-art UHF SAW filters were developed and combined with low loss multiplexing techniques and switches into high performance miniature SAW filterbanks. Design, fabrication and testing are described. Data from the prototype frequency synthesizer is presented.



## Introduction

The purpose of this work was to develop new technology for a low cost, compact frequency synthesizer for integrated terminals for the Joint Tactical Information Distribution System (JTIDS) and Tactical Air Navigation System (TACAN). Such terminals require at least 2 simultaneous independent tones chosen from among 252 frequencies. This is particularly applicable to fighter aircraft, where size, weight, and cost savings are highly significant. Based on a total of 5,000 units, savings on the order of \$20 million (unit cost reduced from \$6000 to \$2000) could be realized. This cost reduction, along with achieving a size of 60 cubic inches or less, are the expected results of a recently awarded Manufacturing Technology (ManTech) contract based on the present work.

## Design Approach

Fractional microsecond frequency-hopping is required for JTIDS. Frequency synthesizers based on retuning phase-locked loops are inherently much too slow for this requirement. The rapid hopping must be obtained without sacrificing quality, i.e., the output tones must be locked to the system clock and of low noise and spurious content. At the same time, the intended airborne and manpack uses dictate that size, weight, and power consumption be minimized. The unit to be described here is a prototype breadboard designed to demonstrate feasibility by synthesizing 219 of the tones. The ManTech contract will improve the synthesizer to achieve 2 simultaneous outputs, all 252 tones, and a compact, readily manufacturable unit.

The concept of the surface acoustic wave (SAW) direct synthesizer is illustrated in Figure 1. A comb generator, or source of multiple frequencies as indicated in the spectrum analyzer display in the upper left-hand corner, is locked to a stable clock. The stability and accuracy of the tones is that of the clock. The comb spectrum is simultaneously fed to the 9 channels of the SAW filterbank, which sorts them according to frequency, so that each input to the 9 X 1 switch carries a single but different tone. The desired tone is then selected by the 9 X 1 switch as indicated.

The basic direct synthesizer architecture of Figure 1 could be realized with any type of filter. It is this design, in which the tones present at the output of each filter are continuous waves (CW), and therefore capable of being switched as fast as the switches themselves,

that yields the high inherent speed of frequency-hopping. However, most filter technologies would lead to a bulky filterbank. SAW filterbanks, on the other hand, are compact, as well as being capable of manufacture by a single photolithographic step. This useful combination of the direct synthesizer approach with SAW technology was the subject of Patent no. 3,891,929 awarded to Carr and Budreau in 1975.

The compactness of SAW devices derives from the velocity of the surface wave being typically  $1/100,000$  that of the speed of light. Dimensions of resonant structures scale in the same ratio. Thus, at 300 MHz, the wavelength of an electromagnetic wave is 1 meter; the corresponding SAW has a wavelength of 0.01 millimeter. Nine SAW filters may be seen as the dark rectangle on the left end of the package of Figure 2. Even though they were not packaged for minimal size, they only occupy a space of 1.6 X 2.7 cm.

Let us consider the operation of a single SAW filter. It is shown schematically in Figure 3. The electromagnetic input signal excites an electric field between the conducting grids of the transducer and is converted, due to the piezoelectric nature of the substrate, to mechanical strain of the surface. This strain then propagates in opposite directions (i.e., in both directions along the long axis of the substrate). The waves propagating to the left from the input transducer are absorbed by the acoustic absorber placed there for just this purpose. The desired waves are those shown propagating between the transducers, which, when they reach the output transducer, generate an electrical signal across the load " $R_0$ ", through the piezoelectric effect. The portion of the waves which pass beyond the output transducer are eliminated by the absorber placed at that end. The center frequency to which the transducers are resonant is determined by the line spacing of the transducers, while the shape of the frequency response curve is determined by their detailed structure.

Shaping of the frequency response, or "weighting", may be accomplished in a number of ways. Two of the most satisfactory forms of weighting, withdrawal weighting and finger overlap weighting (apodization), are shown in the figure, as they were the techniques used for the filters in the synthesizer.

The output of the comb generator, containing all of the desired tones, must be distributed to all 9 SAW filters.

Power dividers are bulky and expensive. At the RADC Deputy for Electronic Technology, we have developed a technique for using a minimum of matching elements in combination with appropriate choice of series and parallel interconnections of the transducers to accomplish the power division in a compact, efficient, yet inexpensive way. This approach was awarded Patent no. 3,942,140 issued to Laker, Carr, and Budreau in 1976, as well as a Proceedings of the IEEE paper by the same authors in May 1976. For the current synthesizer design, we incorporated an improved version of this multiplexing, to be discussed in the SAW and switch section later on.

The requirement for the generation of 219 tones dictated a more efficient system than could have been achieved by directly using the scheme of Figure 1 with 219 filters (252 tones is the appropriate number for an integrated JTIDS/TACAN terminal, but specification changes and a tight schedule dictated the demonstration with only 219). Furthermore, such a "brute force" approach would have had other problems, including the wide bandwidth and close relative spacing of the required frequencies. By starting with three direct synthesizers, and mixing together two sets of 9 tones and one set of 3 tones, we have achieved a capability of  $9 \times 9 \times 3 = 243$  tones. A simplified block diagram of the direct SAW synthesizer using mixing is presented as Figure 4. The mixer synthesizer consists of two 9-tone direct SAW synthesizers of the type in Figure 1, plus a three tone direct synthesizer using three phase-locked loops. For convenience in design, fabrication, and packaging, the synthesizer is divided into three sections. The source section contains comb generators covering 321-345 MHz in 3 MHz increments and 360-468 MHz in 12 MHz increments, plus multipliers and phase-locked loops which produce 1984, 1985, and 1986 MHz tones. In addition, it has the 3 X 1 switch which chooses among the latter sources. The SAW and switch section includes the two 9-tone SAW filterbanks, each of which is connected to a 9 X 1 switch, just as in Figure 1. The output or mixer section contains amplifiers, filters, two mixers, and a frequency doubler.

Let us examine the hardware required in more detail, as shown in Figure 5. Note that 219 tones are obtained by the use of only 18 SAW filters plus the 5 frequency sources. Use of the mixing scheme, plus frequency doubling to achieve the high frequency set of tones, allows the filters to operate in the 321-468 MHz range. Since the line widths and spacings of the SAW transducers are proportional to the wavelengths of the signals to be passed, keeping the frequencies below

500 MHz allows fabrication of the SAW transducers by an extension of conventional optical photolithography.

The overall system design was optimized by choosing the frequencies to be mixed in such a way as to minimize the problems with spurious signals. This was done in collaboration with our colleagues W. M. Bridge and N. Houlding at MITRE Corporation, as we described at the 1976 Ultrasonics Symposium. The problems of the spurious signals produced and the filtering required to get rid of them were crucial, as we were working to satisfy the restrictive specifications shown by the lower curve of Figure 6.

Let us examine Figure 5 more carefully. The synthesizer consists of the three blocks shown. The system clock (1 MHz in our current experiments) provides the reference signal to all five phase-locked loop oscillators (PLLs) of the source package. Each of the sets of 9 tones is used to generate a single signal, as described in connection with Figure 1. These signals are amplified, then the 360-468 MHz tone is doubled to yield a 720-936 MHz tone. The 321-345 MHz tone and the 720-936 MHz tone are mixed to yield a difference in the 378-615 MHz range. This difference frequency is again mixed with the 1984-1986 MHz tone to yield a difference frequency in the desired frequency range. Appropriate amplification and limiting are used to obtain a leveled output. The three blocks will now be described in detail.

#### Source Section

All the signals which appear at the output of the frequency synthesizer arise from combining tones which originate in the source section; these are as stable and accurate as the clock. This stability and accuracy is carried through the synthesizer and is reflected in the high quality of the output signal. On the other hand, any noise or close-in spurious signals present in the source section will also be present in the output, putting very tough specifications on this circuitry. A source package consisting of the two comb generators and a 1984 MHz source was obtained under AF contract from Zeta Laboratories, Santa Clara, CA. The approach was to multiply up from 1 MHz, use crystal filters to select the appropriate harmonic, and use this to drive a step recovery diode. The step recovery diode transforms the input waveform into very narrow pulses which are rich in harmonics. RF filtering of the output comb spectrum was required to meet the specifications. The 1984 MHz was obtained by using a phase-locked oscillator at 99.2 MHz locked to the 1 MHz clock,

followed by a X 20 stage. This was accomplished in a package of 99 cu. in., which could be engineered down to include the 1985 and 1986 MHz sources in the same package. As with other forms of frequency multiplication the step recovery diode approach has relatively high power requirements.

A new and exciting approach for the source section is the mode-locked SAW oscillator (MLSO) developed at United Technologies Research Center, E. Hartford, CT under AF contract. It was described at the 1977 IEEE Ultrasonics Symposium, and also in the final report under the contract, "High Frequency Signal Sources Using Surface Acoustic (SAW) Technology," by Dr. M. Gilden, Report RADC-TR-399, 1977. The operation is shown in the block diagram, Figure 7. A recirculating loop including a SAW delay line, amplifier (AMP 1), and a non-linear element (AMP 2 with low supply voltage) was used to directly produce a stable comb spectrum. While a simple delay loop will generally "lock on" to a single frequency of oscillation, design of a delay path which allows gain greater than unity at the desired frequencies, plus the appropriate non-linear element will yield the comb spectrum. Further, this multi-frequency oscillator can be locked to an external clock. As this SAW-based comb generator has been shown to be smaller, lighter, and to consume less power than the more conventional electronic approach described above, it was our preferred implementation. It yielded the two comb spectra plus the 1984 (but not 1985 or 1986) MHz signals in a package of just under 50 cu. in. This approach will require a temperature compensation scheme which is being implemented under a subsequent contract.

### SAW and Switch Section

In this section, the design, fabrication and testing of the two high performance 9-channel switchable SAW filterbanks on temperature compensated quartz will be described. As depicted in Figure 5, these filterbanks consist of 9 individual SAW filter channels interconnected to operate as a single input, single switch-selected output, device. Each filter consists of a length weighted transducer and a withdrawal weighted transducer as illustrated in Figure 3.

The frequency response of a single high frequency filter shown in Figure 8 demonstrates the extremely high out-of-band rejection of these SAW filters. In order to achieve these results many factors must be optimized and second-order effects controlled. For example, diffraction correction

(to compensate for the spreading of the acoustic beam) is used in the overlap weighted transducer; velocity correction (for the differing acoustic velocities on the bare substrate and those portions covered with metal) is used on the withdrawal weighted transducer; tapered, notched substrates are used to suppress bulk mode spurious (a SAW transducer generates and receives volume waves as well as SAWs); and careful packaging is used to minimize electromagnetic feedthrough.

As mentioned, the individual transducers must be interconnected in order to achieve the desired operation. The goals of any interconnection or multiplexing technique are as follows: 1) insertion loss minimization, 2) insertion loss uniformity among channels, and 3) small size and low cost. Results of our studies have shown that the proper choice of a series-parallel interconnection scheme can achieve each of these goals.

In particular, input multiplexing is achieved here by the parallel interconnection of three inductively tuned sets of three series connected transducers. This multiple-inductor scheme results in both low and uniform insertion loss among channels as illustrated in Figure 9. This efficient scheme is especially necessary in the wide percentage bandwidth (26%), high frequency case. Here a mean insertion loss of 25.8 dB with a standard deviation of only 0.75 dB was attained. The strongest spurious tone for the high frequency bank was 57.5 dB below the desired tone, with only about 10% of the spurious tones worse than 63 dB below the carrier. Excellent results were also achieved for the low frequency bank. The average insertion loss of 19.8 dB (including 1.5 dB due to the switch) can be compared to the individual filter loss of 14 dB. A 5 dB improvement over direct power division is achieved. In addition, for the low frequency bank, the worst case spurious was 61.5 dB below the carrier with only about 3% of the spurious tones stronger than 63 dB down.

Some comments on these spurious levels are in order. The SAW filters are in fact capable of suppressing the spurious signals 63-65 dB as shown, for example, in Figure 8. In addition, under ideal conditions, the switches can achieve 70 dB isolation, particularly for non-adjacent channels. (Note that two switches were investigated: an approximately 2 nanosecond switch having an insertion loss of 16.5 dB, and a 250-400 nanosecond switch having an insertion loss of 1.5 dB). However, in the finished filterbanks, packaging and adjacent channel switch leakage (possibly also due to packaging) resulted in the levels quoted.

Achieving high performance with the SAW filters requires not only proper design but also careful fabrication. Although the transducers require lines and spaces as narrow as 0.8 micrometer together with precise placement, they can be fabricated with straightforward techniques. Such fine structures do require a clean room environment and careful work and attention to cleanliness. Optical photoreduction from masters which are 10 times the final transducer dimensions has several advantages, including the relative low cost of the 10X masters compared to masters with 0.8 micrometer lines and spaces, and the very long mask life due to lack of direct contact. As with any very high resolution technique, monochromatic light of the shortest wavelength compatible with the optics and photoresist must be used. The stripping method, in which the area which is to be metallized, is exposed, developed and stripped, before the evaporation of the desired metal, is essential for such high resolution. Using adjustable magnification with direct projection fabrication reduced the mean deviation from design center frequencies to 0.06 MHz and 0.01 MHz for the high frequency and low frequency filterbanks respectively.

It can be concluded that SAW filters offer outstanding performance in compact, contiguous filterbank devices and that series-parallel interconnection is the preferred manner of achieving the multiplexing function.

### Output Section

The output or mixer section is the right-hand block of Figures 4 and 5 (labeled MIXER PACKAGE). The high performance in spurious rejection and low noise outlined in Figure 6 requires that the output section, like the rest of the synthesizer, be carefully designed. Therefore, it is necessary to use high quality doubled-balanced mixers, filters with high out-of-band rejection, and careful attention to power levels. Fortunately, these components are not major factors in the synthesizer cost.

Whenever two different frequencies are mixed, sum and difference signals plus the input signals, multiples of the input signals, and sums and differences of one input signal with multiples of the other input, all are present. The original choice of the frequencies to be generated and mixed was made using standard techniques for calculating and minimizing the mixer-generated spurious signals. While it is not possible to shift the frequencies so that all possible spurious tones are outside the desired band, it is feasible

to place one of the input signals so that its higher order undesired products are all outside the band of interest, and set this input approximately 20 dB stronger than the other input. The weaker input can then have its higher-order spurious fall in-band, but, as they will be extremely weak, they will be adequately rejected by a balanced mixer. This was the technique followed here. It is illustrated in Figure 10, which shows the most significant spurious frequencies at the doubler and each of the two mixers. The input(s) and the desired output for each stage is given by the solid blocks, and the spurious signals by the dashed ones.

We set up breadboard output section experiments in-house, as well as obtaining a unit made to our specifications under AF contract by Communitronics Ltd., Hauppauge, NY. Low to moderate-priced doublers and mixers were found to have adequate performance provided that power levels were optimized. As in any case where doublers or mixers are used, filtering is required. The stringent requirement to maintain low spurious levels means that the filters must be correspondingly highly selective. SAW filters would have the advantage of extreme compactness, but at the cost of increased insertion loss. A number of low-loss electromagnetic filters are available commercially. Tubular filters, although somewhat bulky and expensive for a final engineered version, have proved valuable for breadboard use in both the in-house experiments and the version built by Communitronics.

The output frequencies obtained by mixing the 1984 MHz tone with all allowed combinations of the two sets of nine tones are given in Table I. The other frequencies are readily obtained by adding 1 and 2 MHz to the given values corresponding to the use of the 1985 and 1986 MHz tones, respectively. In the actual system hardware, logic circuits will choose the proper combination of three tones when a given output frequency is called up.

### Summary and Conclusions

The advantages of the SAW direct frequency synthesizer have been described. A Manufacturing Technology contract to reduce the size of the present laboratory breadboard to less than 60 cubic inches has been awarded. This contract will draw upon the experience of the RADC model as well as two previous ManTech contracts which improved the manufacturability of SAW components, and develop a reasonably priced 252 frequency integrated JTIDS/TACAN synthesizer.



The RADC Deputy for Electronic Technology held a Workshop on SAW Frequency Synthesizers in May 1978 to brief industry on the results of our work and to demonstrate the operation of the breadboard model.

TABLE I

Generation of required frequencies by mixing

high freq bank		360	372	384	396	408	432	444	456	468
high freqs doubled		720	744	768	792	816	864	888	912	936
low freq bank	321	1585	1561	1537	1513	1489	1441	1417	1393	1369
	324	1588	1564	1540	1516	1492	1444	1420	1396	1372
	327	1591	1567	1543	1519	1495	1447	1423	1399	1375
	330	1594	1570	1546	1522	1498	1450	1426	1402	1378
	333	1597	1573	1549	1525	1501	1453	1429	1405	1381
	336	1600	1576	1552	1528	1504	1456	1432	1408	1384
	339	1603	1579	1555	1531	1507	1459	1435	1411	1387
	342	1606	1582	1558	1534	1510	1462	1438	1414	1390
	345	—	—	—	—	—	1465	—	—	—

The above output frequencies are 1984 - (2 X high freq - low freq)

Add one MHz for output with 1985 MHz at the second mixer.

Add 2 MHz for output with 1986 MHz at the second mixer.

Dashed output frequencies are not desired.

## FIGURES

- Figure 1 Single Channel Synthesizer
- Figure 2 Photograph of a bank of 9 SAW filters (left) and a 9 x 1 switch (right) for selecting the output frequency.
- Figure 3 SAW Filter Structure
- Figure 4 Frequency Synthesizer, Simple Block Diagram
- Figure 5 Frequency Synthesizer, Detailed Block Diagram
- Figure 6 Spurious and Noise Specification Curves
- Figure 7 Block Diagram of Mode Locked SAW Oscillator
- Figure 8 Insertion Loss Versus Frequency for Single SAW Filter
- Figure 9 Insertion Loss Versus Frequency for SAW Filterbank
- Figure 10 Spurious Signal Diagram

# 9 TONE DIRECT SAW SYNTHESIZER

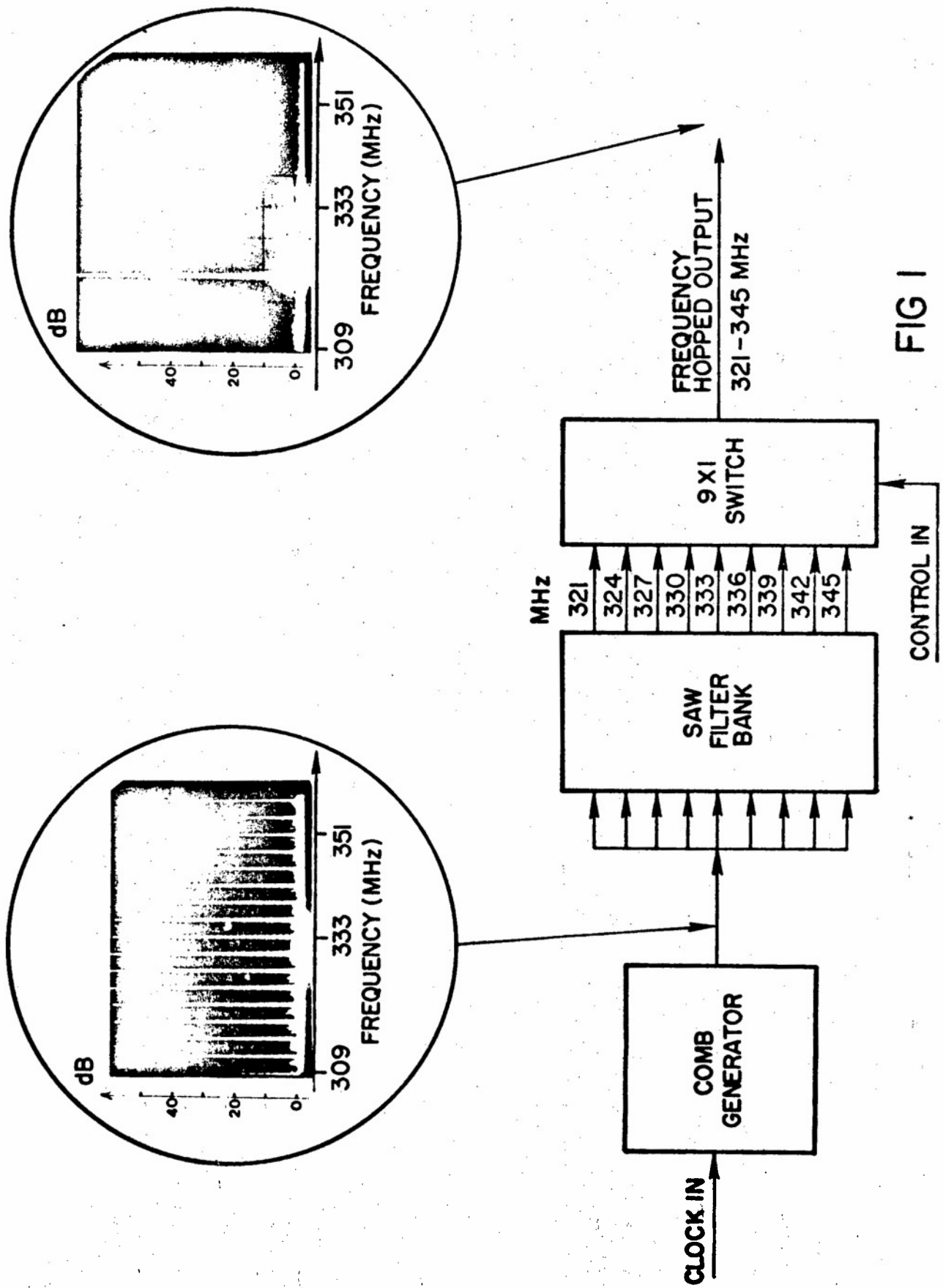
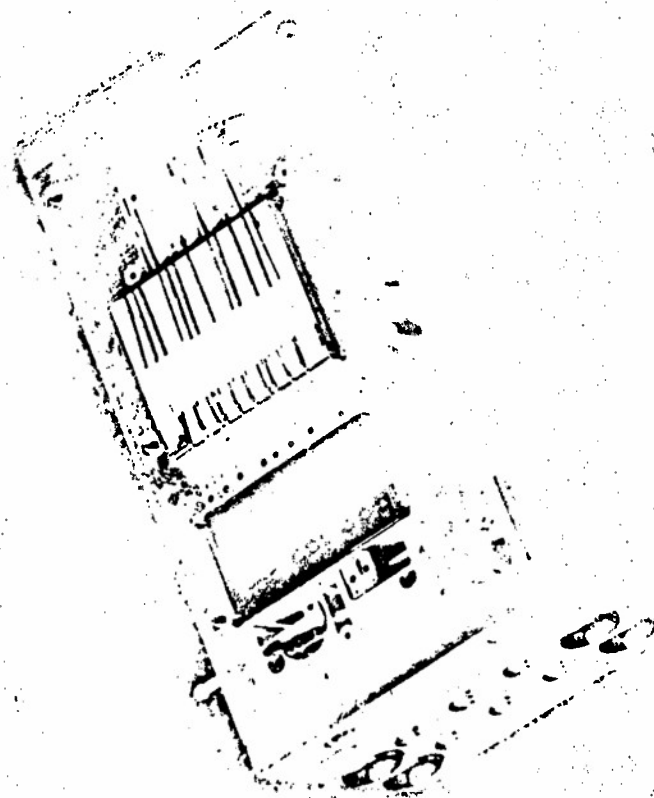
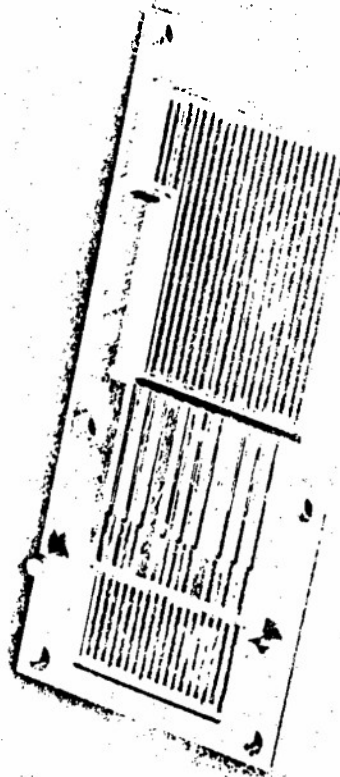
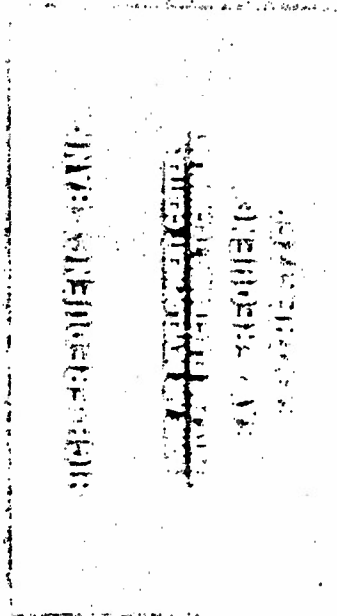
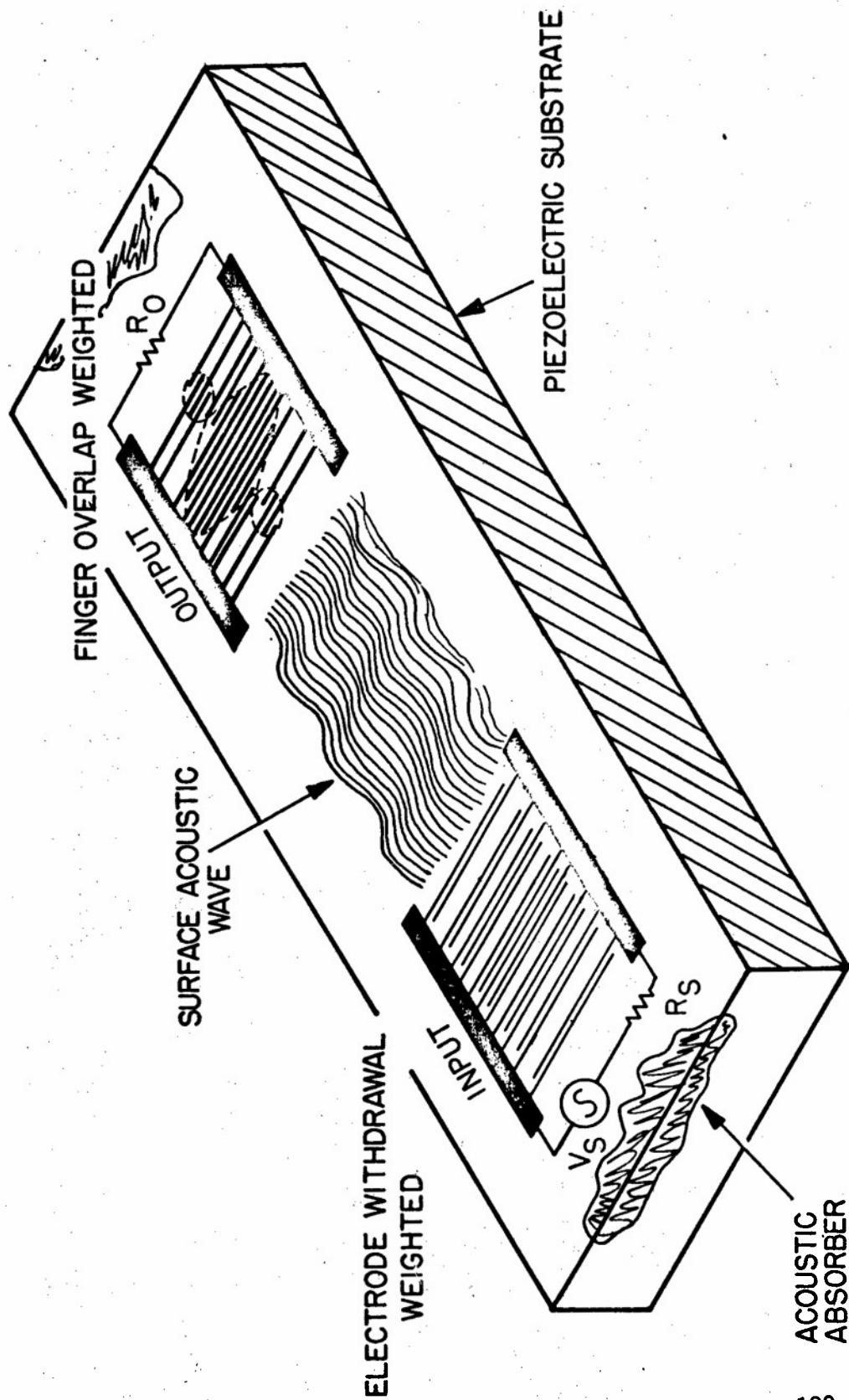


FIG 1



NOT FOR RELEASE  
UNLESS SPECIALLY  
AUTHORIZED

FIG 2



# DIRECT SAW MIXER SYTHESIZER

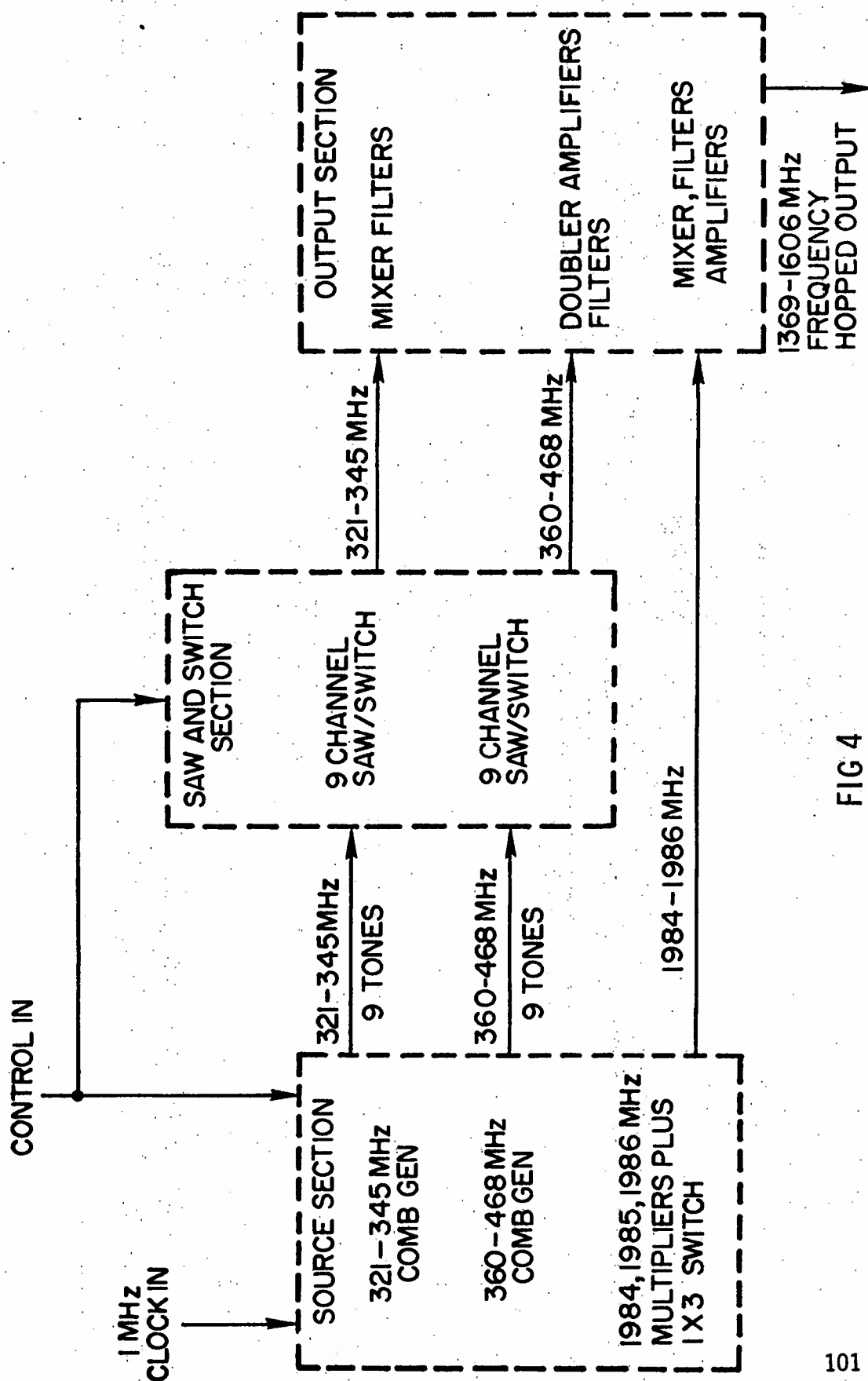
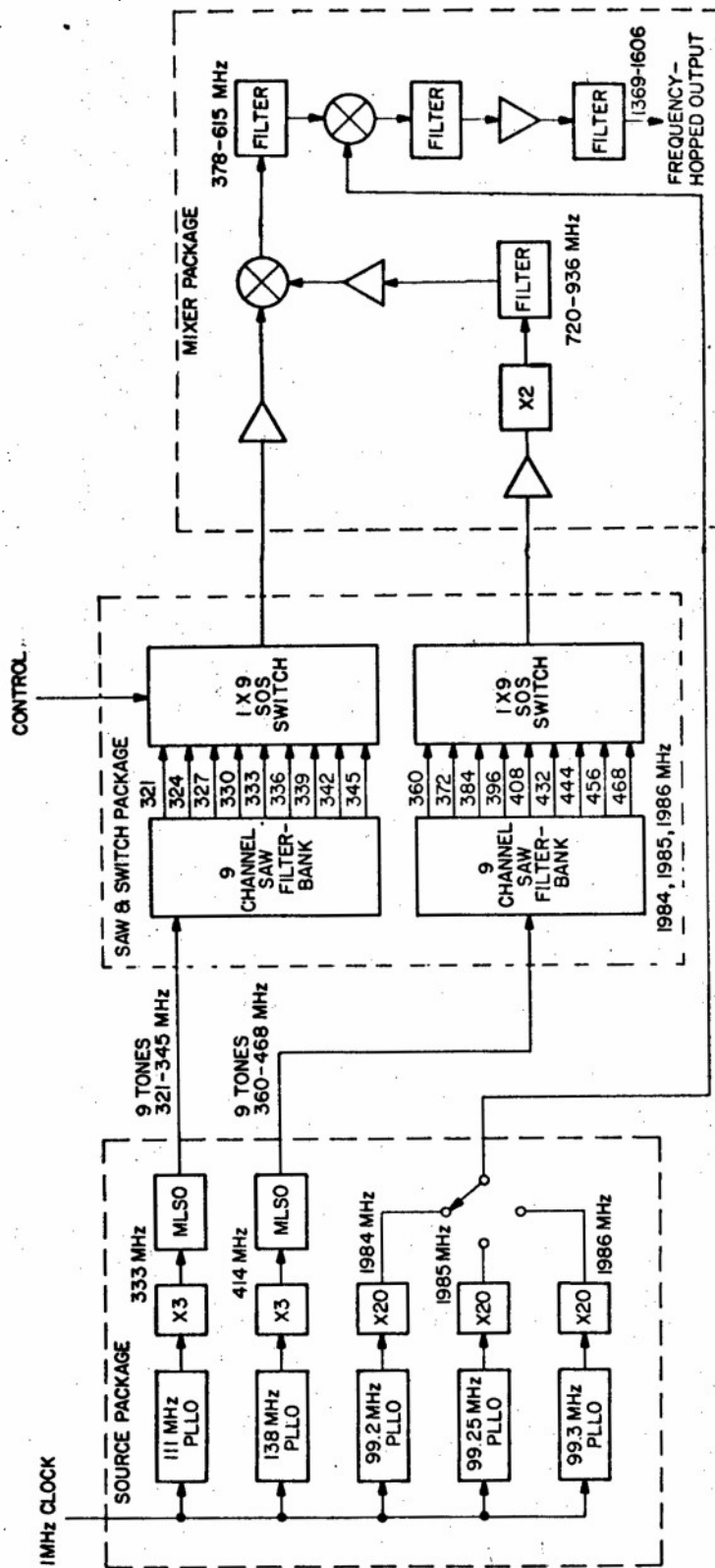


FIG 4



SAW FAST FREQUENCY SYNTHESIZER

FIG 5



# SYNTHESIZER NOISE AND SPURIOUS SPECIFICATION

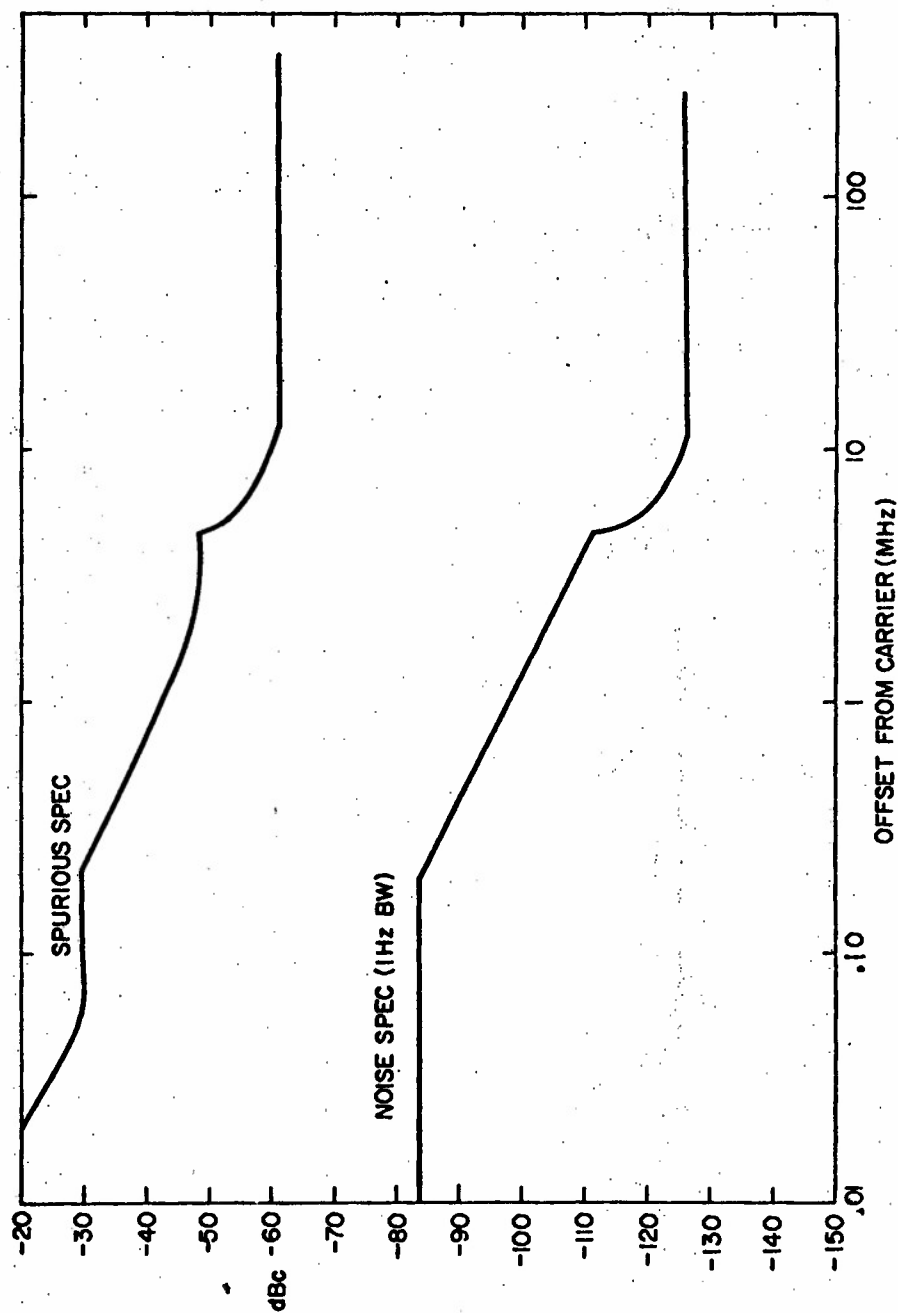


FIG. 6

FINAL VERSION OF MLSO

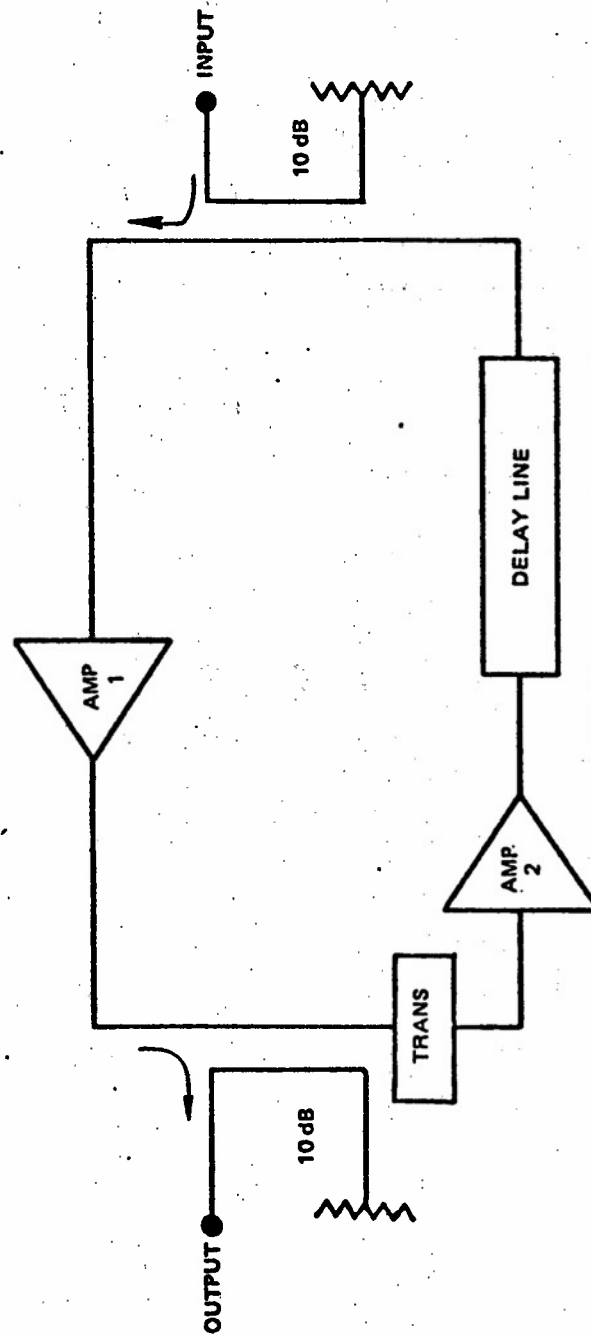


FIG 7

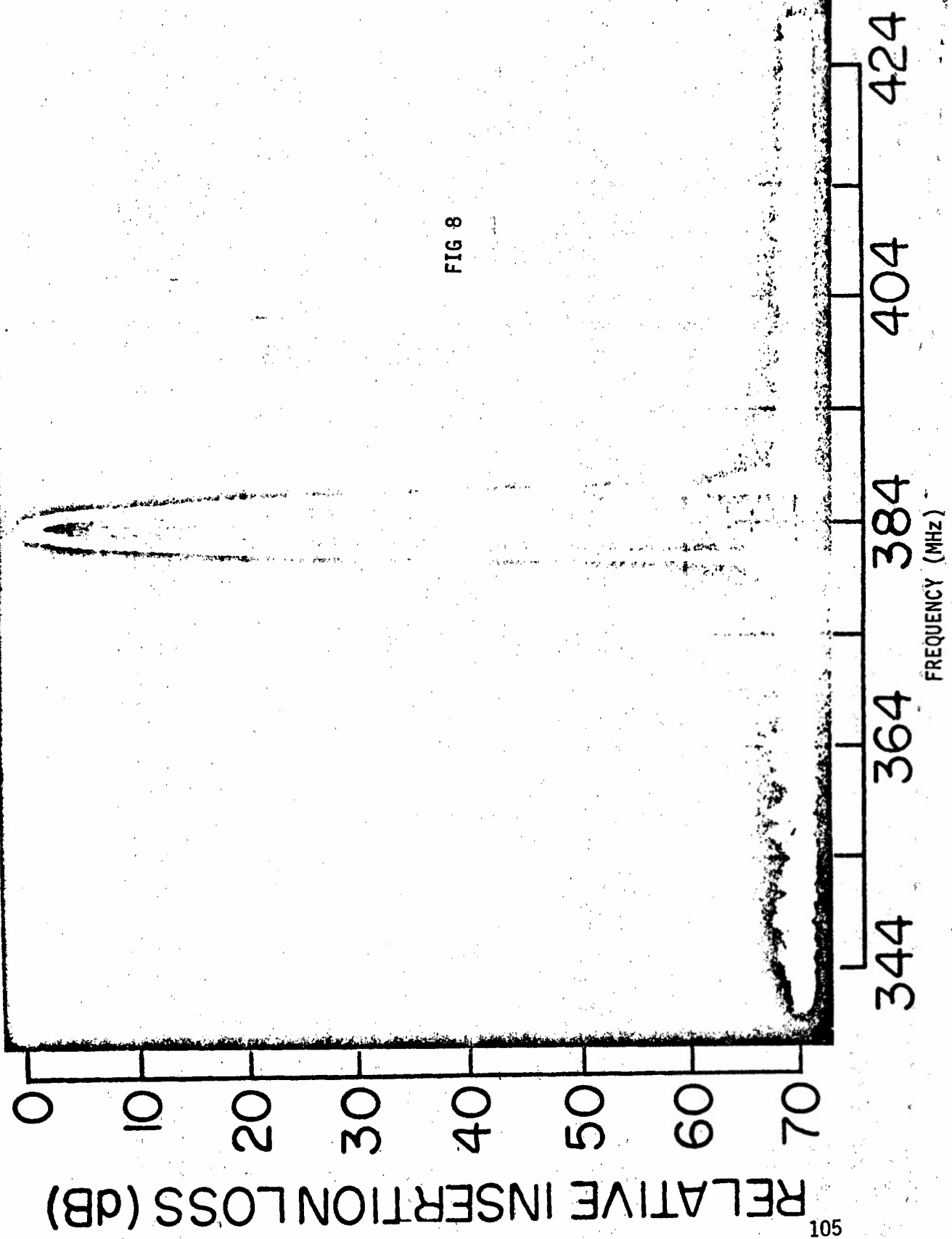


FIG 8

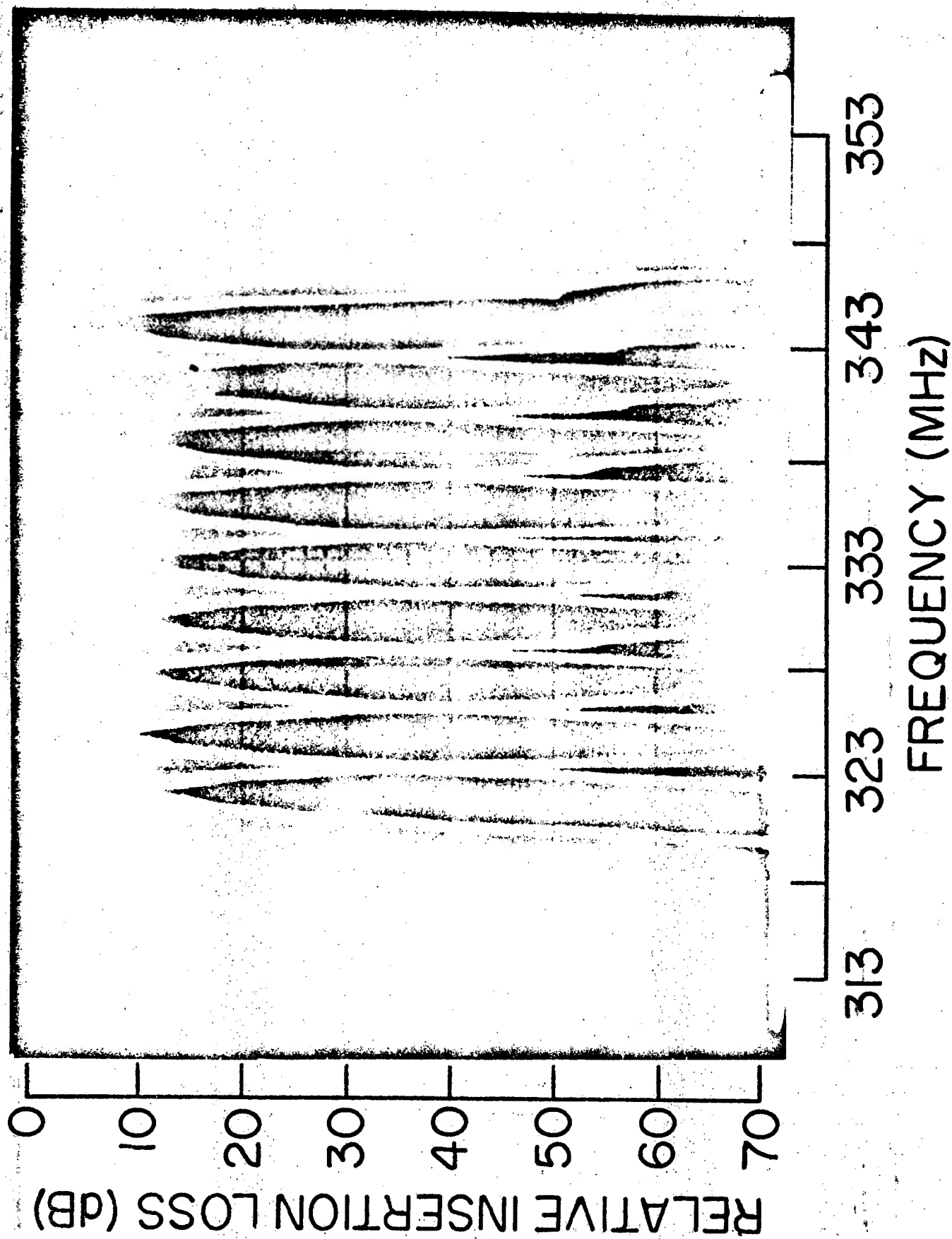


FIG 9

# SIGNIFICANT SPURIOUS SIGNALS

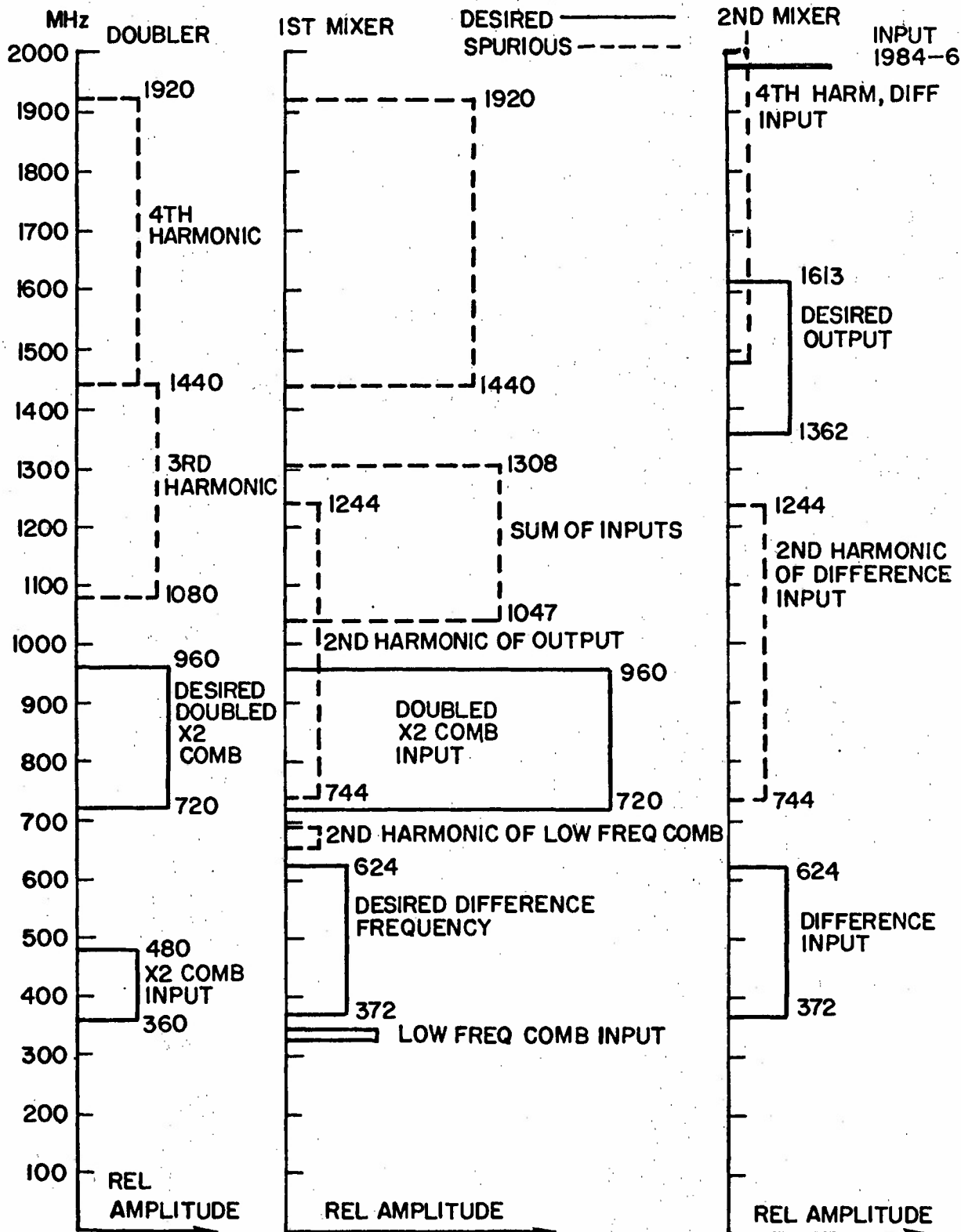


FIG 10

### Biographical Sketches

Alan J. Budreau was born in Miami, Florida. He received the B.S. degree in Physics from the Massachusetts Institute of Technology in 1957, and the M.A. degree in Medical Sciences from Harvard University in 1959. He also carried out research in Microwave Physics at Duke University. He is currently a physicist in the Antennas and RF Components Branch of the Electromagnetic Sciences Division, Rome Air Development Center's Deputy for Electronic Technology (formerly Air Force Cambridge Research Laboratories), Hanscom Air Force Base, MA. He is a Work Unit Scientist for the development of a prototype frequency synthesizer using surface acoustic wave technology. His awards include the Air Force Systems Command Monthly Technical Achievement Award in 1973, and a number of suggestion and invention awards. He has published over 30 papers and is the holder of three patents. Mr. Budreau is serving on the Technical Program Committee of the 1978 IEEE Ultrasonics Symposium. He is a member of Sigma Xi, the IEEE, and the Undersea Medical Society.

Andrew J. Slobodnik, Jr. was born in Lowell, Massachusetts on March 3, 1944. He received the B.S. and M.S. degrees in electrical engineering from the Massachusetts Institute of Technology in 1966. After an additional year of graduate study at the University of California, Berkeley, he began working for the Antenna and RF Components Branch, where he has been employed to the present time. He is currently working in the area of microwave acoustic surface wave research and development. Mr. Slobodnik has received numerous invention awards. He is a member of the IEEE.

Paul H. Carr received the B.S. and M.S. degrees in Physics from the Massachusetts Institute of Technology in 1957 and 1961, respectively, and the Ph. D. degree in Physics from Brandeis University, Waltham, MA in 1966. He is currently Assistant Chief of the Antennas and RF Components Branch. Dr. Carr directs in-house and contractual research and development of RF on surface acoustic wave components. Dr. Carr was co-winner with A. Slobodnik of the Marcus D. O'Day Memorial Award for the best AFCRL paper published in a scientific journal in 1967. Dr. Carr also received the 1973 Guenter Loeser Memorial Award for sustained scientific achievement at AFCRL. In 1976 he won an Air Force Systems Command Outstanding Technical Achievement of the Quarter Award for the development of a low spurious delay line which solved a "false target" problem in operational Air Force radar. He has published over fifty

papers and is the holder of seven patents including a delay line with quarter-wave taps. Dr. Carr has been active in the IEEE (Institute of Electrical and Electronic Engineers) serving as chairman of the Boston Section on Sonics and Ultrasonics in 1973-1974 and on the Technical Program Committees of the 1971-1975 Ultrasonics Symposia, of which he was Chairman in 1976. He is a member of the American Physical Society, and the DDR&E Advisory Group on Electron Devices Working Group on Microwave Devices.

ENHANCED MEASUREMENT CAPABILITY USING  
A BACKGROUND SUPPRESSION SCHEME

BY

Ernest R. Huppi, M.S., USAF  
and  
George A. Vanasse, Ph.D., USAF

Optical Physics Division

Air Force Geophysics Laboratory  
Hanscom AFB, Massachusetts



Enhanced Measurement Capability Using  
A Background Suppression Scheme

Abstract

A brief description of Fourier Spectroscopy will be presented as an introduction to the description of a novel technique of potential application to military surveillance, strategic and tactical missions. The AFGL Background Optical Suppression Scheme (BOSS) will be described in detail and its potential for target detection in the presence of interfering background radiation will become evident. Experimental studies of the principle of the technique will be shown where background suppressions of two orders of magnitude have been obtained. Modifications of the implementation of the technique will be briefly presented. These modifications allow background suppression to be effective even for structured background as seen by an IR sensor system. The technique allows spatial, spectral and temporal discrimination to be accomplished in one sensor for enhanced mission performance. A simple implementation of the technique will be described for the specific application of auroral measurements from an aircraft when the measurement constraints are that the sensor must look at the target through a warm window. Consequences of the use of the BOSS technique for this particular application will be discussed.

## Introduction

The essence of the technique of Fourier Spectroscopy<sup>1-3</sup> is to take radiation of large spectral bandwidth and sinusoidally modulate the intensity of each spectral component (of wavelength  $\lambda_n$ , or wavenumber  $\sigma_n = 1/\lambda_n$ ) of the band at a frequency proportional to  $\sigma_n$ , and of amplitude proportional to its intensity  $I(\sigma_n)$ . The radiation from all of the spectral components are simultaneously detected by a single detector whose output is called an interferogram.

The instrument which is used to produce this selective modulation is an ordinary Michelson interferometer (or some of its modifications) as shown in Figure 1. The radiation under study is amplitude divided into two identical beams by the beamsplitter and recombined into one beam after one beam has traveled a distance  $x$  greater than the other. As the optical path difference  $x$  between the beams is increased (by moving mirror  $M_1$ ) the detector output yields the autocorrelation function  $F(x)$  of the input electromagnetic field. The detector output (neglecting constants and numerical factors) is given by

$$F(x) = \int_{\sigma_1}^{\sigma_2} I(\sigma) \cos 2\pi\sigma x \, d\sigma \quad (1)$$

where  $(\sigma_2 - \sigma_1)$  represents the radiation spectral band width  $\Delta\sigma$ . The spectral power density of the radiation  $I(\sigma)$  is thus seen to be given by the inverse transform

$$I(\sigma) = \int_0^X F(x) \cos 2\pi\sigma x \, dx \quad (2)$$

where  $X$  represents the maximum path difference, produced by the interferometer, between the two interfering beams. The value  $X$  determines the spectral resolution  $\delta\sigma = 1/2X$ .

The interferometer is used for spectral measurements because of its manifold advantages over conventional grating

or prism techniques\*. However, it also turns out that it lends itself easily to a technique of background suppression<sup>4</sup> which we shall now describe.

### Background Optical Suppression Scheme

Let us consider the two interferometers shown in Figure 2 with their corresponding interferograms shown on their right. We notice immediately that the interferograms are complementary, while the only change as regards the interferometers, is that the input radiation enters the interferometer through the upper face of the beamsplitter for the upper case, but the lower face of the beamsplitter for the lower case. It should be evident, that, if the radiation is allowed to enter a single interferometer simultaneously through the upper and lower faces of the beamsplitter, (which would correspond to adjacent fields-of-view of the interferometer) the two interferograms at the right in Figure 2 would be simultaneously generated and, upon falling onto one detector, would yield an interferogram which has no structure. This is tantamount to saying that no spectral information about the radiation is contained in the output interferogram function.

Let us assume that the input radiation is sky background radiation which is reasonably<sup>+</sup> uniform and enters the interferometer through the upper and lower faces simultaneously. Because of the complementary characteristics of their interferograms, the resultant detector output shows no modulation. Imagine now that a target appears in one field-of-view but not the other; the signal generated by the background is a constant but now the interferogram has structure which is due to the target only. A Fourier transformation of this interferogram yields the spectral signature of the target with no spectral content due to the background.

### Demonstration and Application

Figure 3 shows experimental results<sup>++</sup> obtained under conditions of uniform background and adjacent fields-of-view.

\*The interested reader can refer to the references for a more rigorous and complete description of Fourier Spectroscopy.

+This suppression technique can also be implemented to suppress structured background, but this will not be discussed here due to lack of space; see reference 5.

++Work accomplished under contract with Visidyne, Inc., and funded by the AFGL Laboratory Director's Fund.

The upper left trace shows the background radiation coming from one field-of-view only, while the upper right trace is from the other field-of-view only. The bottom trace is the resultant interferogram when the background enters the two fields-of-view simultaneously. The background suppression was measured to be about two orders of magnitude; which implies that the target could be fainter than the background by about 100 and still generate detectable structure in the interferogram.

We have mentioned above that structured backgrounds can be treated as well as uniform backgrounds (although as must be noted with increased complexity). Here we propose using the technique for the case when the interferometer must view a faint or distant target through a warm window, where the emission from the window is significantly greater than that from the target.<sup>6</sup> The obvious approach to suppressing the window spectral emission is to operate the interferometer in the dual-beam mode where the window emission enters simultaneously the two fields-of-view of the interferometer, while the target is seen through only one field-of-view.

One example involving the use of a dual beam interferometer is the spectral measurement of infrared auroral emission from an aircraft as illustrated in Figure 4. The aircraft can be flown at sufficiently high altitude to avoid much of the absorption and emission of the lower atmosphere, but even at high altitudes the emission of the atmosphere in the infrared is significant. A further complication is added by the emission of the window through which the interferometer views the aurora. The interferometer operating dual beam only measures the difference between what is viewed by the two beams. Since both beams view the window and the atmosphere, the resultant interferogram contains no modulation. When an auroral arc enters one beam there is a difference and the interferometer signal is an interferogram of only the auroral emissions.

The measurement of auroral emission is just one example of the potential uses of the dual beam background suppression interferometer. In general, the technique can be used anytime a target can be spatially isolated against a uniform background and could certainly be used to measure aircraft and rocket emissions against warm backgrounds.

### References

1. "Aspen International Conference on Fourier Spectroscopy", 1970 (G.A. Vanasse, A.T. Stair and D. Baker, Eds.), AFCRL-71-0019, 5 Jan 1971, Spec. Rep. No. 114.
2. G.A. Vanasse and H. Sakai, Fourier Spectroscopy, in "Progress in Optics" (E. Wolf, Ed.), Vol. 6, pp 261, North-Holland Publ., Amsterdam, 1967.
3. "Introductory Fourier Transform Spectroscopy", by Robert Bell, Academic Press Publ., New York, 1972.
4. G.A. Vanasse, R.E. Murphy and F.H. Cook, "Double-Beaming in Fourier Spectroscopy", Appl. Opt. 15, p 240, Feb 1976.
5. "Background Optical Suppression Scheme (BOSS)", G.A. Vanasse, A.T. Stair, O.W. Shephard, and W. Reidy, Report AFGL-TR-77-0135.
6. E.R. Huppi, "Cryogenic Instrumentation", in Spectrometric Techniques, (G.A. Vanasse, Ed.) Vol. I, pp 153, Academic Press, New York, 1977.

MICHELSON INTERFEROMETER

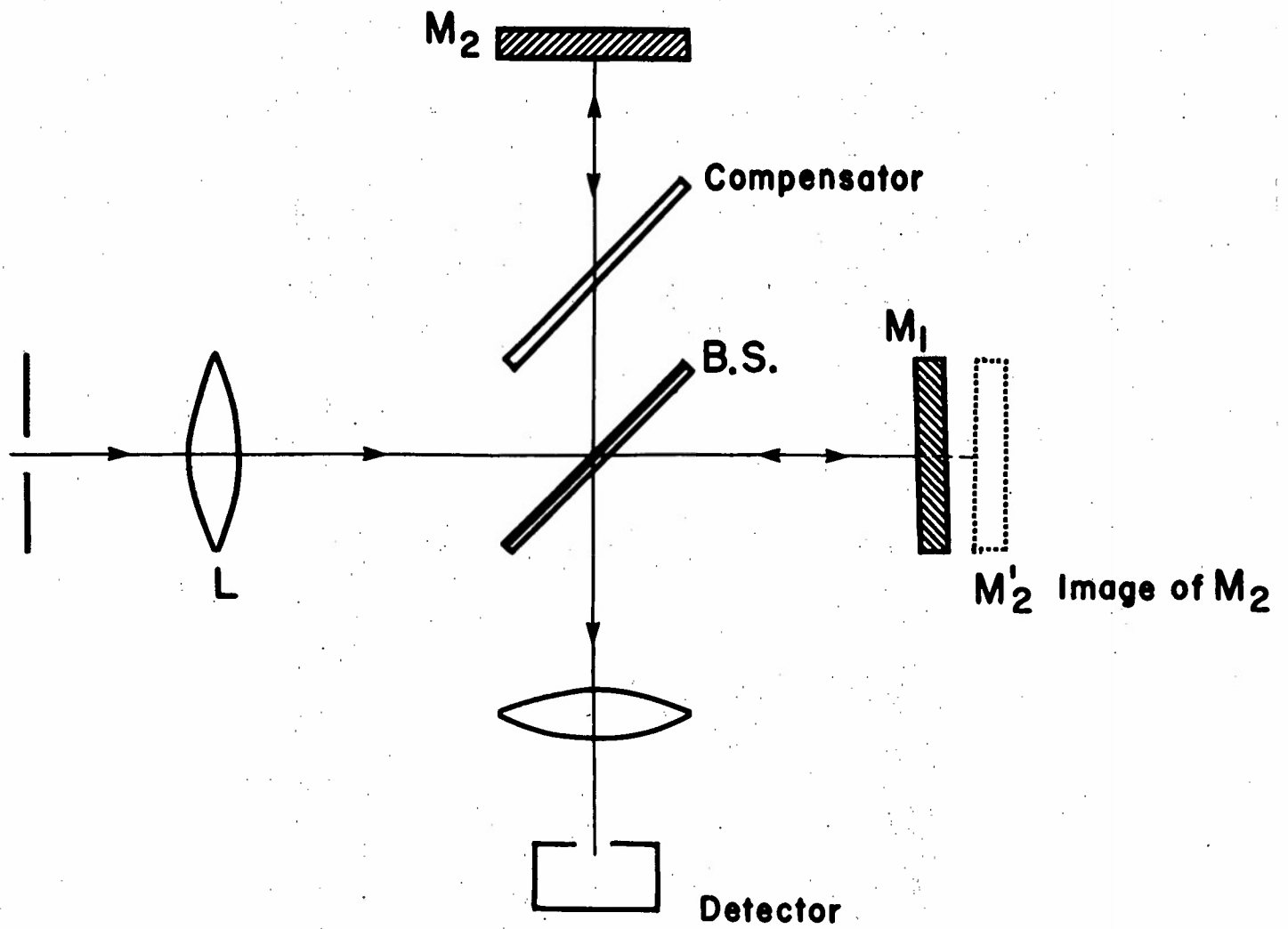


FIGURE 1

MICHELSON INTERFEROMETERS WITH THEIR CORRESPONDING INTERFEROGRAMS  
OBTAINED BY MOVING ONE OF THE MIRRORS

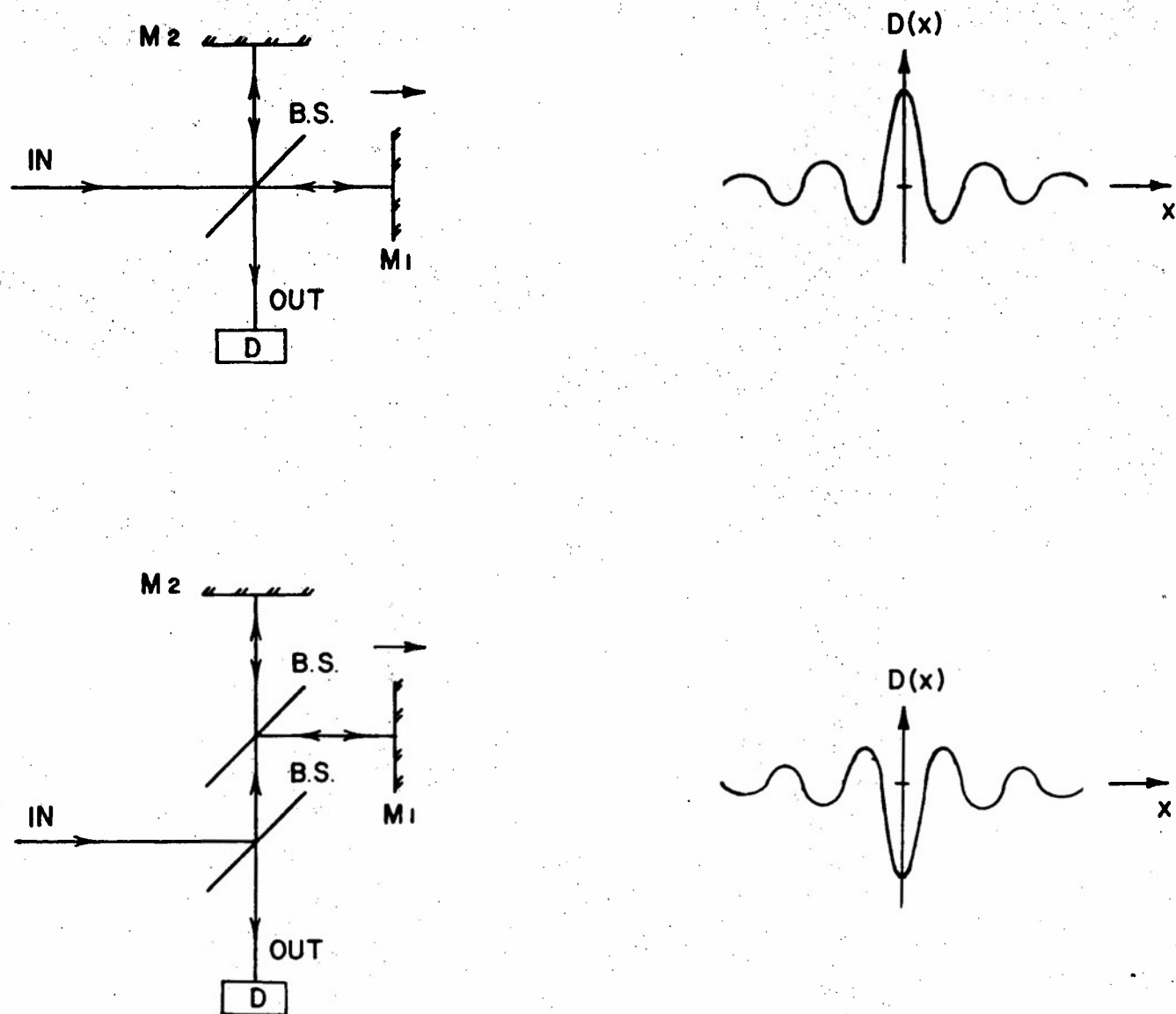
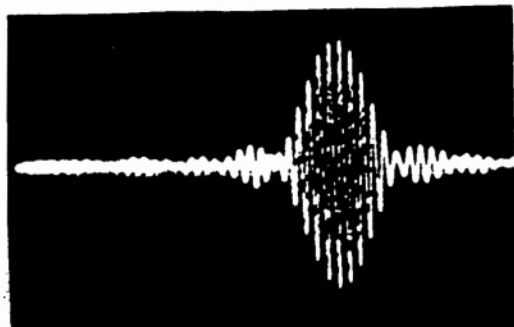


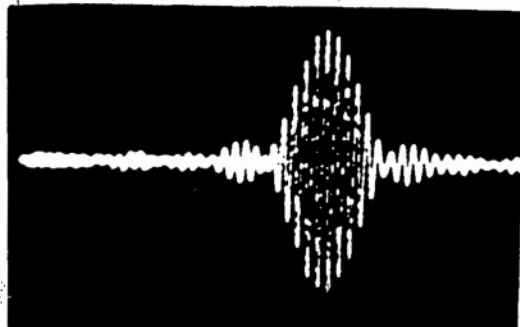
FIGURE 2

EXPERIMENTAL RESULTS ILLUSTRATING THE EFFECTIVENESS OF THE AFGL  
BACKGROUND SUPPRESSION SCHEME  
(Photograph Courtesy of Visidyne)

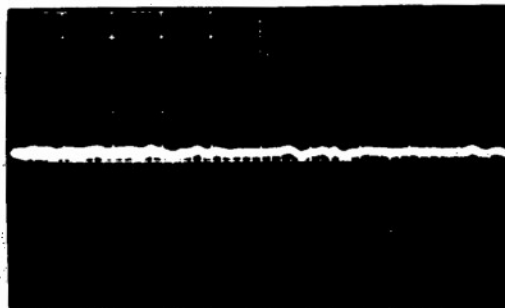
DOUBLE-BEAM INTERFEROMETER LABORATORY TEST RESULTS



SINGLE-BEAM BACKGROUND  
INTERFEROGRAM



SINGLE-BEAM COMPLEMENTARY  
BACKGROUND INTERFEROGRAM



DOUBLE-BEAM BACKGROUND  
INTERFEROGRAM

FIGURE 3



SPECTRAL MEASUREMENT OF INFRARED AURORAL EMISSION USING A  
DUAL-BEAM BACKGROUND SUPPRESSION INTERFEROMETER

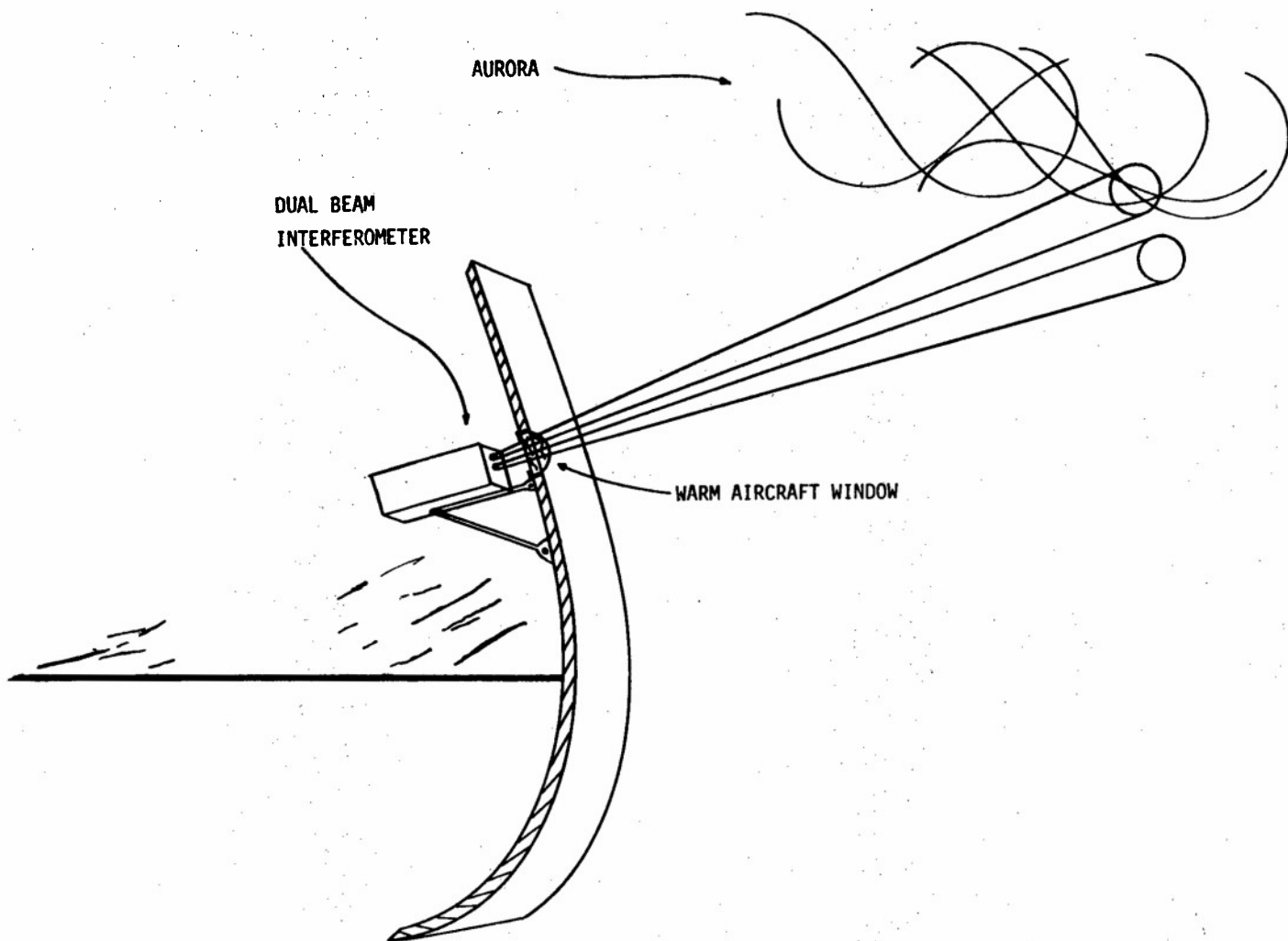


FIGURE 4

### Biographical Sketch

Ernest Ray Huppi was born in Logan, Utah on February 18, 1939. He graduated from Utah State University at the top of his class with a B.S. in Electrical Engineering in 1962. He worked briefly for the Aerospace Division of the Boeing Aircraft in Seattle, Washington before coming to the Stewart Radiance Laboratory of Utah State University located in Bedford, Massachusetts. He received his Master's Degree in Electrical Engineering from Utah State University in 1966, shortly after which he became director of the Stewart Radiance Laboratory.

Mr. Huppi joined the Air Force Cambridge Research Laboratories (now Air Force Geophysics Laboratory) in 1968. His interests have been primarily in the field of advanced infrared instrumentation for use on aircraft and rocket platforms. He has pioneered the field of cryogenic infrared sensors for the measurement of airglow and auroral emissions. He is a recognized expert in Fourier transform spectroscopy - having written the chapter on cryogenic spectroscopy, including interferometric techniques for a recent book - the only published treatise on this subject. He is a project leader on a major measurement program using a KC-135 jet aircraft for the Defense Nuclear Agency and consults with NASA on their major cryogenic shuttle experiments, CLIR (Cryogenic Limb Interferometer Radiometer) and COBE (Cosmic Origin Background Experiment).

### Biographical Sketch

Dr. George A. Vanasse was born in Woonsocket, Rhode Island on October 8, 1924. After having served nearly three years in the European Theater of Operations, as an interpreter, from 1943 to 1946, he entered the University of Rhode Island where he obtained a B.S. degree in Engineering Physics in 1950. From 1950 to 1952 he taught at Boston College, worked temporarily for AFCRL and obtained a M.S. degree in Physics from Boston College. From there Dr. Vanasse went to The Johns Hopkins University studying and teaching there and, temporarily, at Goucher College.

After receiving his Ph.D. degree in Physics, with a minor in mathematics and a field of competence in Greek Philosophy, (from The Johns Hopkins University), he became a staff research assistant in the Astrophysics Department at The Johns Hopkins University until October 1959 when he joined AFCRL. His interests have always been directed toward the advancement of the state of the art of spectrometric techniques; mainly high-throughput multiplex systems. He is a member and fellow of the Optical Society of America, Phi Kappa Phi and Sigma Mu and his work has resulted in the publication of over thirty scientific papers and his becoming an Editor of a Series entitled, "Spectrometric Techniques" published by Academic Press.

SPECTRUM ESTIMATION AND ADAPTIVE CONTROLLER  
FOR  
LONG RANGE, COMPLEX SCATTERING TARGETS

by  
ROBERT F. OGRODNIK

9 AUGUST 1978

AIR FORCE SYSTEMS COMMAND  
ROME AIR DEVELOPMENT CENTER  
GRIFFISS AIR FORCE BASE, NY 13441

### ABSTRACT

An adaptive control methodology is developed based on optimal principles using spectrum estimation procedures of complex, scatterer resolved, long range target returns for purposes of precision pointing control and selected target scatterer illumination. Aim point selection of scatterers would assist in target identification and discrimination operations. It is the intent of the adaptive controller/spectrum estimator, developed here, to assist in such operations in such a manner that range transit time does not ultimately limit adaptive pointing control and scatterer selection on target, and that the scattering spectrum inherent in complex structured targets are fully used as a new dimension of information for pointing system control purposes. The approach incorporates autoregressive spectrum estimations algorithm techniques for scatterer induced spectrum resolution and coherent spectrum detection. Adaptive principles are based on scatterer spectrum selection criteria with spectrum width convergence serving as target loop closure logic. The control algorithm is modeled in an optimal sense through the selection of spectrum and motion observables which demonstrate enhanced sensitivity to scatterer convergence and spectrum noise discrimination. An adaptive optics,

complex structure target example is considered with energy convergence as a performance figure-of-merit at a selected scatter. This example will use experimentally obtained scatterer data, and an assumed target structure and active pointing system parameter set which is representative of current long range identification/discrimination mission operations of interest to the Air Force.

## 1. OVERVIEW OF APPROACH AND DEVELOPMENT

This analysis addresses active illuminating systems and complex targets. That is, targets characterized as having structure larger than the beam size in the target space and scattering surface texture which is varied in nature locally across the target, with variations which include specular and diffuse textures relative to the illuminating wavelength and correlation length. The illuminating system is assumed to be adaptive both in transmitter wavefront phasing and in pointing. That is, wavefront focusing or phasing and energy centroid steering or positioning are assumed to be available in real time for control in the target space. Control criteria is energy maximization at a resolvable target scatterer, with scatterer being both identifiable and selectable by the system controller. The study results will show that backscatter field spectrum narrowing provides a good convergent criteria which inherently leads to energy maximization, and that spectrum correlation can aid in scatterer selection for aimpoint control.

Because complex target returns behave randomly at the receiver (random in regards to their point of origin and intensity due to constructive interaction between specular and diffuse returns) an entirely random active system is

considered<sup>(1,2)</sup>, that is a random pulse transmitter is part of the modeled active system with spatial coherence and adaptation being the system control parameters. The adaptive controller is based on spectrum estimation via autoregressive methods<sup>(3)</sup>, with spectrum frequency narrowing as the prime loop closure logic for energy convergence on a selected target specular locality, or on a finite extent target diffuse region. A second motivation for selecting a random signal system approach is the freedom from range and frequency ambiguity due to the random waveform. This inherently will allow the adaptively controlled system to achieve maximum target scatterer resolution and energy maximization without waveform ambiguity limitations. This feature optimizes the employment of the super resolution properties of autoregressive spectrum estimation techniques<sup>(4)</sup>.

We will first develop the received signal scattering model, the system correlation processor, and the controller architecture applicable to adaptively phase driven random pulsed coherent systems. This will be followed by a performance assessment of super resolution techniques simultaneously being employed as adaptive controller and signal parameter estimation.



## 2. MODELING - SIGNAL, SYSTEM, CONTROLLER, ADAPTIVE CRITERIA

Since the goal of this development is high resolution of target structure and scattering centers as well as adaptive illumination (with maximum energy convergence) of a selected scattering center, the illuminating system chosen is a pseudo random waveform pulsed radar with wavefront phase control implemented on a pulse-to-pulse basis. The random radar is selected due to its freedom from range and velocity ambiguities<sup>(2)</sup>, permitting maximization of target resolution both in range (slant range) and velocity (cross range). Pulse-to-pulse wavefront phasing is selected for energy convergence to a single target region or scattering center for enhanced target resolution in support of high resolution identification missions.

A received pulse  $x(t')$  at time  $t'$  can be related to a family of preceeding pulses  $x(t' - kT)$ ,  $k = 1, \dots, L$  (defined as the pulse sequence  $\{x(t')\}_{k,L}$ ), all having a random waveform but a specified wavefront phase distribution, by an  $L$ th order autoregressive process given by the following difference equation,

$$x(t') = \sum_{k=1}^L a_k^{(L)} x(t' - kT) + n(t') \quad (1)$$

where  $T$  is the pulse period,  $n(t')$  is a stationary Gaussian white noise process with zero mean and variance  $\sigma_n^2$  associated with the signal sample  $x(t')$ . The digitized version of this form, assuming sample time spacing  $T$ , sequence of available time samples  $\{x_{k_L}\}$  and current time signal sample  $x_i$ , becomes

$$x_i = \sum_{k=1}^L a_k^{(L)} x_{i-k} + n_i \quad (2)$$

which defines the current signal sample in terms of the  $L$  former samples ( $L$  lags for the autoregressive process).

Coefficients  $\{a_{k_L}\}$  will be defined later in terms of the receiver structure as a sampled sequence correlator.

That is, for enhanced resolution and sensitivity, the receiver will be modeled as a pulse correlator which references a sample of  $x(t)$  that has been stored by the system at the time of transmission for purposes of coherent detection. Returning to the time analog format (Eq (1)), each pulse experiences a transit time lag  $T_k(t) = T_k - C_k t$ , where  $C_k$  is the lag rate at  $t$ , the time referenced to pulse transmission which is related to the pulse arrival time  $t'$  as,

$$t' = t - T_k(t) = (1 + C_k) t - T_k \quad (3)$$

giving,

$$x(t) = \sum_k^L a_k x((1 + C_k)t - T_k - kT) + n(t) \quad (4)$$

noting the initial incremental range of  $k = 1, \dots, L$ . The correlator will reference some  $j$ th pulse in the stored sequence  $\{x(t)_{jL}\}$  yielding the following reference sequence

$$[\text{stored sample of } x(t)] \rightarrow r(t), \text{ where} \quad (5)$$

$$r(t) = \{x(t - T_j(t))\}_L = \{x(1 - C_j)t - T_{jL}\}$$

#### A. CORRELATOR-COHERENT DETECTION:

The correlator output can be modeled as a low pass filtered output (the expected value of the product  $x(t) r(t)$ ) having the form,

$$E [x(t) r(t)] = R_{xr}(t)$$

$$\begin{aligned}
&= \sum_{k,j}^{L,L} a_k^{(L)} R_{xx}[(C_k - C_j)t - (T_k - T_j)] \\
&\quad + E [n(t) r(t)] \quad (6)
\end{aligned}$$

where  $R_{xx}$  is the autocorrelation of  $x(t)$ . In the sampled system where both signal and reference have been digitized as a binary data set with sample intervals of length  $T$  and where reference signal correlation with transmitted waveform noise ( $n(t)$ ) gives a non zero value only for the data sample occurring at time  $t$ , the correlator output can be modeled as,

$$\begin{aligned}
E [x(t) r(t)] = E (x_i r_i) &= \sum_i^L a_i^{(L)} R_{xx} (iT) \\
&\quad + E [n_i r_i] \quad (7)
\end{aligned}$$

#### B. RECEIVED NOISE ENERGY-MAXIMIZATION CRITERIA

If we return to Eq (2), the digitized  $L$  lag format for current time sample  $x_i$  (at  $t - t' = i T$ ), we can define  $a_0 = -1$ , giving for the received noise energy at current time increment  $i$ ,

$$n_i = \sum_{k=1}^L a_k^{(L)} x_{i-k} - x_i = \sum_{k=0}^L a_k^{(L)} x_{i-k} =$$

$$FN \left( \left\{ x_i \right\}_L, x_i \right) \quad (8)$$

Thus noise energy conservation demonstrated by the random waveform radar can be defined by the correlator stored reference sample set  $\left\{ x_i \right\}_L$  plus the current time sample  $x_i$  in terms of total noise at the current time  $t$  by Eq. (7).

A condition of phasing the signal pulses at the target which maximizes the pulse summing in Eq. (8) can readily serve as a target illumination control criterion for energy maximization at a single target scattering point. Thus phasing adaptation is based on

$$n_i]_{\text{maximization}} = \sum_{k=0}^L a_k^{(L)} x_{i-k} \quad (9)$$

for a random waveform radar using coherent pulse detection based on the sequence  $[ \left\{ x_i \right\}_L, x_i ]$ .

C. COMPUTATION RELATIONS AND NOISE VARIANCE:

Since  $n_i$  correlates only with  $x_i$  (current time sample), multiplying Eq. (8) by  $n_i$  and taking the expected value gives,

$$E [ n_i^2 ] = E [ n_i x_i ] = \sigma_n^2 \quad (10)$$

This allows us to define, in a mean squared error sense, from Eq. (7),

$$\begin{aligned} \sigma_n^2 &= E [ x(t) r(t) ] - \sum_{i=1}^L a_i^{(L)} R_{xx}(i) \\ &= R_{xx}(0) - \sum_{i=1}^L a_i^{(L)} R_{xx}(i) \\ &= - \sum_{i=0}^L a_i^{(L)} R_{xx}(i) \end{aligned} \quad (11)$$

where the coefficients  $\{a_i^{(L)}\}$  (noting  $a_0^{(L)} = -1$ ) can now be defined in terms of the sample correlation (5,6),

$$R_{xx}(i) = \frac{1}{N} \sum_{k=1}^{N-i} x(k) x(k-1) \quad (12)$$

and the following recursion relationships, bearing in mind that  $a_i^{(L)}$  denotes the  $i$ th autoregressive coefficient of an  $L$ th order autoregressive process,  $i \leq L$ ,

RECURSION RELATIONSHIP:

$$a_i^{(L)} = a_i^{(L-1)} - a_L^{(L)} a_i^{(L-1)} ; i = 1, \dots, L-1 \quad (13)$$

with the final coefficient  $a_L^{(L)}$  satisfying

FINAL COEFFICIENT:

$$a_L^{(L)} = \frac{R(L) - \sum_{i=1}^{L-1} a_i^{(L-1)} R(L-i)}{R(0) - \sum_{i=1}^{L-1} a_i^{(L-1)} R(i)} \quad (14)$$

This sequence is worked out in Section 3 of this paper where a performance assessment of the spectrum estimator/controller is made. Now that we have the noise variance  $\sigma_n^2$  and control criterion  $n_i]_{\max}$  (Eqs. (11) and (9), respectively) modeled in terms of the sequence correlator, we can define the target scattering spectrum in terms of  $\sigma_n^2$  and a scattering

correlation time  $b^{-1}$ , relatable to the coherent integration interval  $NT$ , or the number of total scattered pulse sequences which can be coherently summed<sup>(1,2)</sup>.  $b^{-1}$  is driven by the doppler spread in the backscattered return, being different for glint, diffuse and self convolved adaptive control spectral scattering regions. An examination of the spectrum profile in Figure 1 should clarify this point. Glint (see Note 1) or specular returns generally originate from discontinuous and/or smooth (in terms of the transmitting wavelength) target regions, where the latter case involves target geometry in terms of the directionality (towards to receiver line-of-sight) of the local surface normal. These returns generally remain coherent with system stored transmitter references, demonstrating large  $b_g^{-1}$  magnitudes (or narrow spectral peaks. Thus the glint scattering spectrum can be modeled<sup>(1)</sup> as,

$$S_{gg} = 2 b_g \sigma_n^2 / (w^2 + b_g^2) \quad (15)$$

---

Note 1. The definition of specular or glint as used here is based on the optical or near-optical region of the spectrum where returns from wavelength smooth surfaces preserve illuminating spatial coherence.



The diffuse (surface texture regions rough or on a comparable scale to the illuminating wavelength) generally represent extended target regions of the dimensions of the illuminating beam size in the target space. The backscatter correlation time  $b_d^{-1}$  is generally quite short, giving a much broader, reduced magnitude spectrum for the diffuse returns, with typically<sup>(1)</sup>

$$b_d > 10 b_g ; \text{ thus,}$$

$$|S_{dd}(o)| \leq |S_{gg}(o)| / 10 \quad (16)$$

The self convolved generated spectrum emanates from spectrum modulation due to adaptively driven illumination of selected target localized regions convolved with the target illuminated silhouette which is represented by the sampled signal sequence, that is, the time history of illumination covered by the system for the L history samples. The control algorithm which was found adequate was based on a simple monotonic stepping routine, where wavefront convergence or phase tapering implemented a series of corrections in one directional sense, then returned to a nominal profile (contained within or at the start of this sequence) in anticipation of

adaptive performance assessment. This assessment was based on Eq. (9) criteria, that is maximization of the received random (noise) transmitter energy, for a trial sequence of wavefront profile changes. Performance assessment involved the simple test of  $n_i$  increase trend sensing over a L-N trial sequence, where N approached L-1 when energy increase trends were confirmed. Wavefront profile stepping rates were fixed, being nominally less than  $(10 T)^{-1}$  for stable control performance.

$$\text{Thus } f_{\text{control}} \lesssim 1/10 T \quad (17)$$

The self convolved spectrum was adequately modeled as

$$S_{cc} = \sigma_n^2 / [ (w^2 - w_c^2) - b_c^2 w^2 ], \quad (18)$$

$$w_c = 2\pi f_{\text{control}}$$

and  $b_c \simeq b_g$ , since stepping control preserves the spatial coherence with the transmitted pulse train, and convergence generally hunts target regions which are specular in nature, that is preserves the spatial phase of the return. The above spectral modeling is analogous to a Markov first order random process for the specular ( $S_{gg}$ ) and diffuse ( $S_{dd}$ )

spectral regions, and a Markov second order process for the self convolved region.

The estimator/controller approach modeled above, namely (a) Spectrum Estimator, Eqs. (11), (13) through (16), and (18); (b) Controller and Criteria, Eqs. (8), (9) and (17), are tested in a system example in Section 4.

### 3. PERFORMANCE ASSESSMENT OF SPECTRUM ESTIMATOR/ADAPTIVE CONTROLLER APPROACH

We shall assess the performance of the autoregressive spectrum estimator/adaptive controller modeling approach by considering a high resolution system example. We select a laser radar system candidate for this demonstration since such systems inherently support high resolution capabilities but also suffer from good control procedures and criteria due to target backscatter interaction with beam convergence controllers.

The candidate system is a random waveform pulsed radar, nominal pulse repetition and digital sampling rates of 1 MHz, operating wavelength in the near infrared at 10.6 micrometers. Adaptive control involves phasing the outgoing wavefront of a sequence of pulses to maximize illumination at a selected target scattering point and to converge the beam size in the target space such that a reduced target region is illuminated,

the reduction primarily limited by the corrected diffraction performance of the system antenna (Cassegrain beam expander) plus propagation path anomalies (atmospheric turbulence and beam disturbance inducing factors). Corrected near-diffraction performance is experience here because only focus control (outgoing wavefront phase profile on a pulse-to-pulse basis) is implemented. High order wavefront correction would demonstrate close to vacuum diffraction beam convergence in the target space. The system parameters are given in Table 1. The autoregressive computing relations are listed in Table 2 for the first 3 orders. System convergence is displayed in Figure 2. The convergence time profile is compared with an earlier reported estimation technique<sup>(1)</sup>. The same intensity maximum is reached at the target normal glint point for both the autoregressive approach and the maximization estimation approach (described in Reference 1) but the former is at least faster by a factor of 100. Indicated convergence time is less than 1 millisecond for the autoregressive method. This is primarily attributable to the non periodic nature of the pulsed radar system configured here as well as the random phase stepping method. Random stepping is not limited to any system carrier frequency and can exhibit rapid control convergence, providing the convergence trends are established early in loop closure execution.

#### 4. CONCLUSION

Spectrum estimation and system convergence can be achieved based on pulse sequence energy maximization logic and autoregressive estimation methods for non periodic control procedure systems. The pulsed radar example considered here has verified this point. Random stepping and random signal radar systems using these principles potentially can demonstrate enhanced target irradiance and potential resolution increases over non adaptive or periodic controlled system concepts.

## REFERENCES

1. Ogrodnik, R.F., Asher, R.B., "Estimation and Control in Multidither Adaptive Optics", JOSA, Vol 67, pp 350-359, Mar 77
2. Chadwick, R.B., Cooper, G.R., "Measurements of Distributed Targets With the Random Signal Radar", IEEE Trans. on Aerospace and Electronic Sys, Vol AES-8, pp 743-750, Nov 72
3. Kavek, M., Cooper, G.R., "An Empirical Investigation of the Properties of the Autoregressive Spectral Estimator", IEEE Trans. on Information Theory, Vol 1T-22, pp 313-323, May 76
4. Proceedings of the RADC Spectrum Estimation Workshop, RADC/OCTS, Griffiss AFB, NY 13441, 24 May 78
5. Post Doctorate Studies, University of Vermont, Consultant Dr. D.C. Lai Memo dated 5 Jun 78
6. Durbin, J., "The Fitting of Time-Series Models", Rev. Inst. Int. Statistics, Vol 28, No. 3, p233-243, 1960.

TABLE 1.

## SYSTEM PARAMETERS

## Target Parameters

range 1.1 km

apparent angular rate 10-100 millrad./sec

apparent beam sizes on target 1-5 meters

## System Parameters

Antenna (optical telescope - cassegrain)

Primary diameter 60 cm.

Secondary diameter 12 cm.

Nominal focus distance 0.8 km

starting mirror spacing 0.7912 m

finishing mirror spacing 0.7911 m  
for  $I_{max}$ ,  $n_{max}$ 

## Waveform

random pulse shape,

Pulse rate 1 MHz.

Nominal pulse width 50-150 nanosec.

Pulse-to-Pulse phase control.

## Control

Pulse sequence phasing (focusing).

Random grouping (pulse sequence)  
from 3 to 12 pulses.Monotonic phase stepping in single  
direction, with return to original  
step position

## Criteria

Maximization of  $M_i$  for a given  
phasing sequence.

TABLE 1. SYSTEM PARAMETERS (cont)

Target scattering spectrum

$$b_g = 5 \text{ Hz}$$

$$b_d = 100 \text{ Hz}$$

$$b_c = 5 \text{ Hz}$$

$$\sigma_m^2 = 2.5 S_{gg}$$

$$|S_{gg}/S_{dd}|_{\omega=0} \sim 10$$

$$\omega_c/2\pi = 100 \text{ kHz}$$

$$|S_{gg}/S_{cc}|_{\omega_c} \sim 10''$$

OPTIMUM WAVEFRONT STEPPING

5 SEQUENTIAL STEPS  
+ 20° PHASE ADVANCE



TABLE 2. COMPUTATION RELATIONSHIPS

AUTOREGRESSIVE COEFFICIENTS:

first order,  $L=0$

$$a_1^{(1)} = R(1)/R(0)$$

$$R(0) = \frac{1}{N} \sum_{i=1}^N x^2(i)$$

$$R(1) = \frac{1}{N} \sum_{i=1}^{N-1} x(i)x(i+1)$$

second order,  $L=1$

$$a_1^{(2)} = a_1^{(1)} - a_2^{(2)} a_1^{(1)}$$

$$= [1 - a_2^{(2)}] R(1)/R(0)$$

$$a_2^{(2)} = \frac{R(2) - R^2(1)/R(0)}{R(0) - R^2(1)/R(0)}$$

$$R(2) = \frac{1}{N} \sum_{i=1}^{N-2} x(i)x(i+2)$$

third order,  $L=2$

$$a_1^{(3)} = [1 - a_3^{(3)}][1 - a_2^{(2)}] R(1)/R(0)$$

$$a_2^{(3)} = [1 - a_3^{(3)}] a_2^{(2)}$$

$$a_3^{(3)} = \frac{R(3) - a_1^{(2)} R(2) - a_2^{(2)} R(1)}{R(0) - a_1^{(2)} R(1) - a_2^{(2)} R(2)}$$

$$R(3) = \frac{1}{N} \sum_{i=1}^{N-3} x(i)x(i+3)$$

TABLE 2. COMPUTATION RELATIONSHIPS (cont)

CONTROL RELATIONS :

$$\text{Eq. 8: } m_i = \sum_{k=0}^L a_k^{(L)} x_{i-k} = \text{FN}(\{x_i\}_L, x_i)$$

$$\text{Eq. 9: } m_i]_{\text{MAX}} \quad \text{CONTROL CRITERIA}$$

$$\text{Eq. 17: } f_{\text{CONTROL}} \leq 1/10 T$$

SPECTRUM ESTIMATION:

$$\text{Eq. 11: } \sigma_m^2 = -\sum_{i=0}^L a_i^{(L)} R_{xx}(i); a_0^{(L)} = -1$$

$$\text{Eq. 12: } R_{xx}(i) = \frac{1}{N} \sum_{k=1}^{N-i} x(k)x(k-i)$$

$$\text{Eq. 13: } a_i^{(L)} = a_i^{(L-1)} - a_L^{(L)} a_i^{(L-1)}; i=1, \dots, L-1$$

$$\text{Eq. 14: } a_L^{(L)} = \frac{R(L) - \sum_{i=1}^{L-1} a_i^{(L-1)} R(L-i)}{R(0) - \sum_{i=1}^{L-1} a_i^{(L-1)} R(i)}$$

$$\text{Eq. 15: } S_{gg} = 2b_g \sigma_m^2 / (\omega^2 + b_g^2)$$

$$\text{Eq. 16: } b_d > 10 b_g; |S_{dd}(0)| < |S_{gg}(0)|/10$$

$$\text{Eq. 18: } S_{cc} = \sigma_m^2 / [(\omega^2 - \omega_c^2) - b_c^2 \omega^2]$$

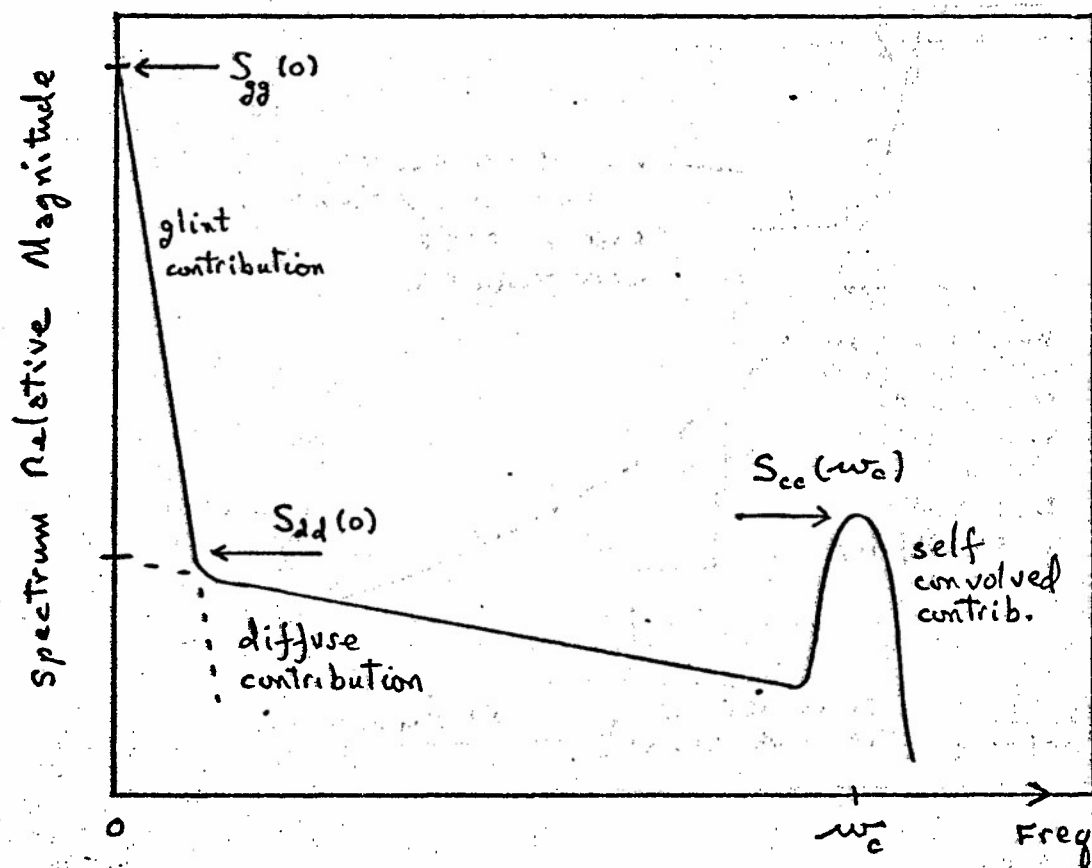


FIGURE 1. NOMINAL TARGET SCATTERING SPECTRUM

Note contributions from specular (glint),  
diffuse and adaptive self convolved  
scattering phenomena

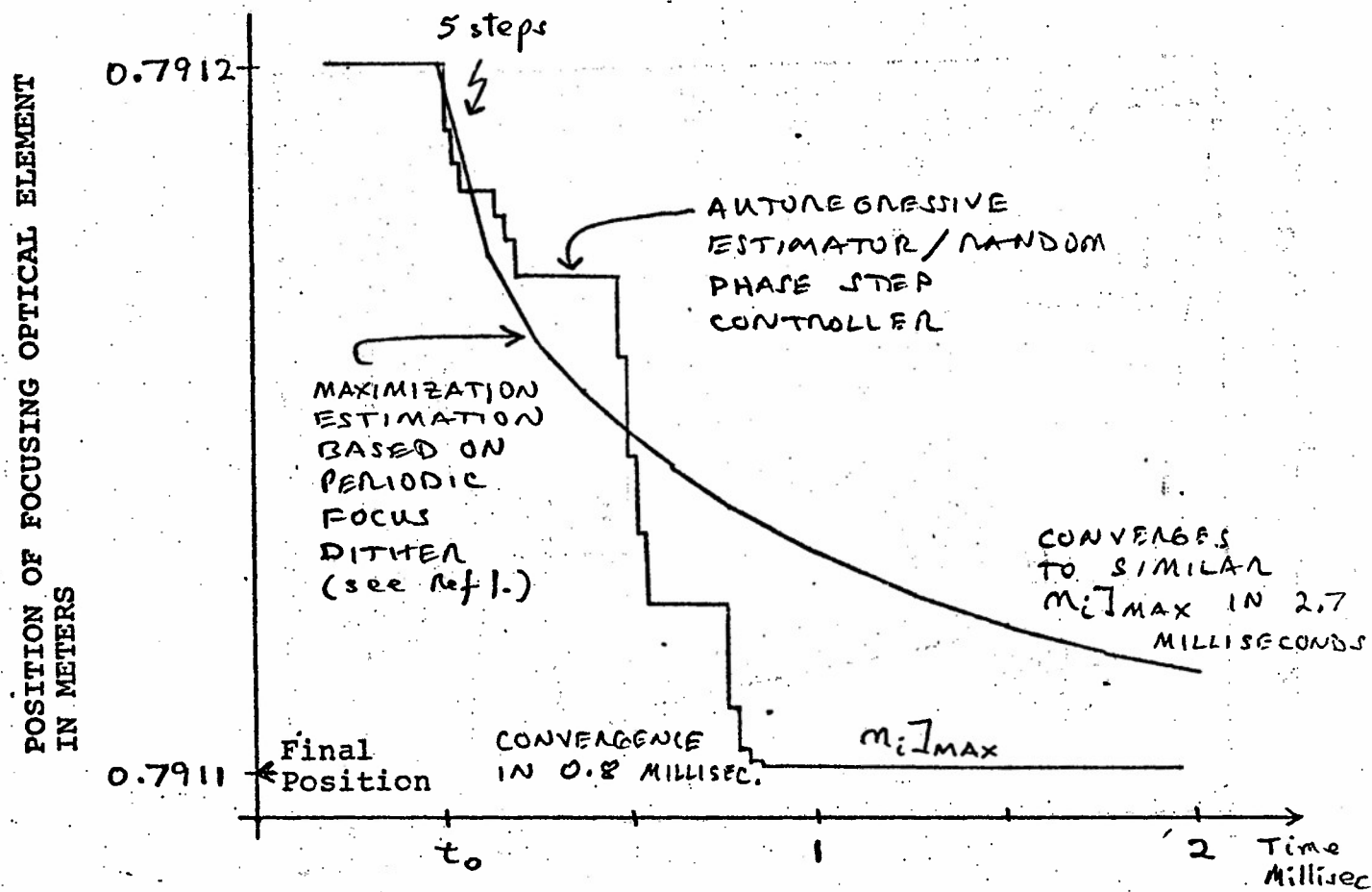


FIGURE 2. FOCUS CONTROL CONVERGENCE

Note the comparison of the autoregressive approach (the stepped curves) versus an earlier modeling of a estimator/controller based on energy maximization techniques (see Reference 1)

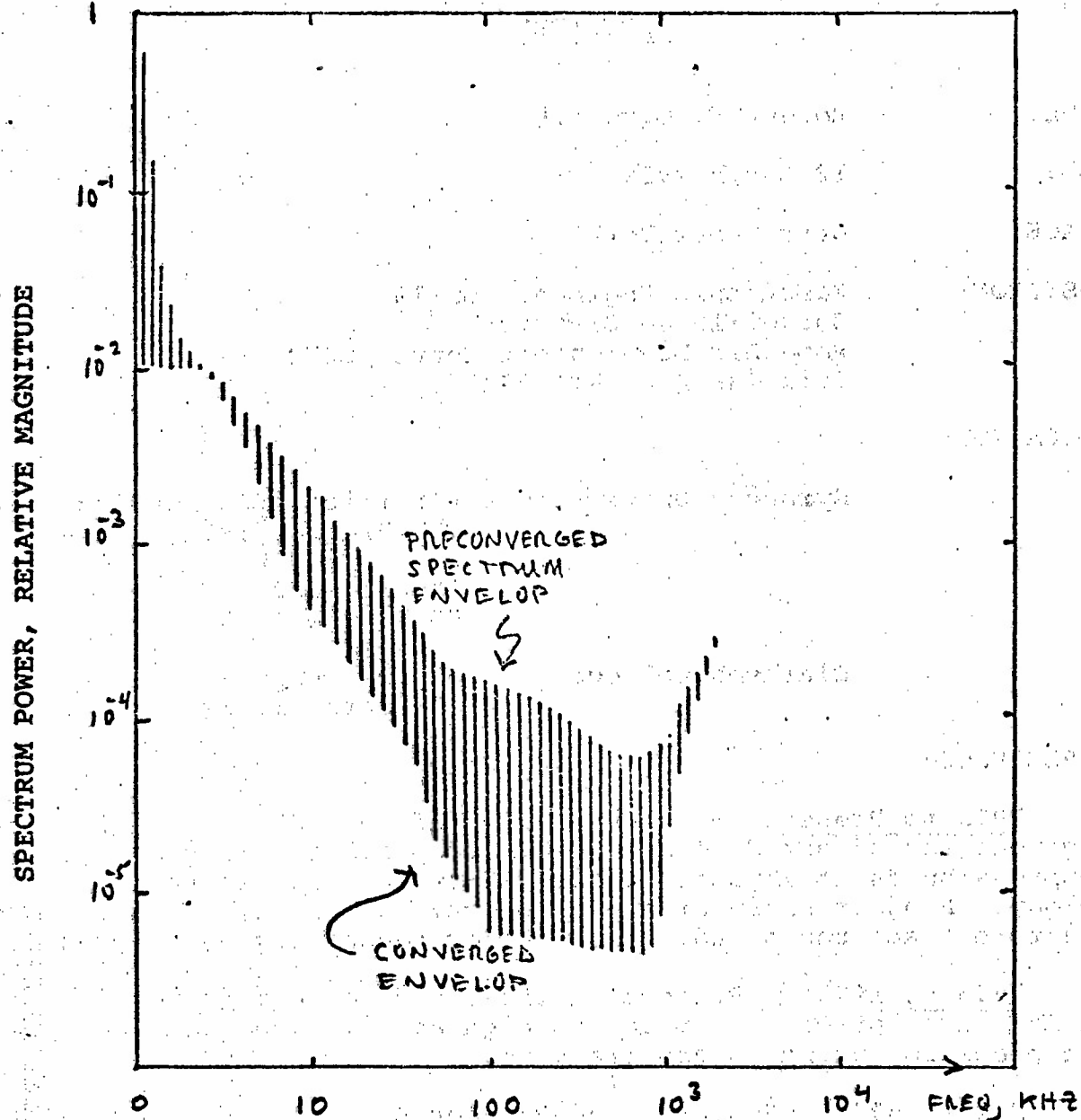


FIGURE 3. SPECTRUM CONVERGENCE

Note spectrum convergence as beam phases to single target scatterer.

Selected scatter was geometrically normal for this example.

## BIOGRAPHY

NAME: Robert F. Ogrodnik  
DOB: 18 March 1939  
PLACE: Utica, New York  
POSITION: Electronic Engineer, GS-13  
Surveillance Division  
Rome Air Development Center/OCTM  
Griffiss AFB, NY 13441

### EDUCATION:

Syracuse University - Electrical Engineering Dept  
PhD Program 1975 to present  
- Physics Dept  
MS Degree 1969  
Clarkson College - Physics Dept  
BS Degree 1961

### EXPERIENCE:

1975 to Present - Technically define and serve as Project Engineer for advanced techniques in adaptive tracking and glint suppression as it impacts Advanced Tactical Surveillance Technology. Project Engineer and technical consultant on DARPA large aperture space based radiometer sensor technology developments.

1973 to 1975 - Project Engineer and technology focal point in Adaptive Optics as applied to high energy laser beam control and precision pointing and tracking

Prior 1973 - Research and Project Engineer on Laser Radar technology.

**SPATIAL AND TEMPORAL CODING OF GaAS LASERS FOR  
A LASER LINE SCAN SENSOR**

**BY**

**Reese S. Shinkle, Captain, USAF**

**Aeronautical Systems Division  
Directorate of Avionics Engineering  
Laser/Electro-Optical Branch  
Wright-Patterson AFB, Ohio 45433**

Spatial and Temporal Coding of GaAs Lasers for  
a Laser Line Scan Sensor

Abstract

Line scanning laser sensors which measure range and reflectance are currently being developed to be used as the front end of real-time image processors. This paper establishes the space-time combination of intensity modulation and scan pattern for N GaAs laser sources which results in optimum system performance. A noise model based upon the Poisson point process behavior of a direct (optical intensity) detector is developed. Estimation theory, based upon the Poisson statistics of the detector, is used to develop the maximum-likelihood processor for both range and reflectance. Performance expressions are presented to relate the variance of the range and the reflectance estimates to the line scan system parameters; and the variance of both is shown to be proportional to the detected signal energy. Various combinations of spatial and temporal coding of the N laser sources to separate the return signal energy from each ground resolution cell while increasing the returned energy per cell are evaluated. Based upon the variance of the range and reflectance estimates, the optimum spatial-temporal coding combination is chosen. It is shown that if a large maximum unambiguous range is not required, the best performance possible is achieved with N sources scanned in parallel, each source being sinusoidally modulated. If a large maximum unambiguous range is required, however, the best performance is achieved with N sources scanned in parallel, each source using sinusoidal modulation which is On-Off-Keyed by a pseudo-noise (PN) code.



## Introduction

Line scanning laser sensors are currently being developed to be used as the front end of real-time image processors. Properly coded intensity modulation of the active illumination (scanning laser beam) provides the capability to record both images (reflectance data) and three dimensional characteristics (slant range data). Range gating might be used in the classical radar sense for clutter rejection in order to increase the signal return from a particular target in the scene or to produce height profiles (cross-sectional boundaries). The target height and reflectance data could then be processed by pattern recognition algorithms for target cueing and threat assessment.

Future operational constraints require small, light, efficient, and rugged laser line scanners. A very favorable source candidate is the semiconductor GaAs laser diode which is very small and lightweight. Unfortunately, the GaAs laser is also a low power device, thus requiring the use of many laser diodes to produce the same performance achievable with a larger, more powerful solid state or gas laser.

The problem is to determine an efficient way to combine  $N$  (an integer number) GaAs laser beams for estimating range  $\hat{r}$  and reflectance  $\hat{\rho}$ . Unfortunately it is impractical to combine  $N$  GaAs laser beams into one beam; the optical problems involved are many and complex, and large single substrate arrays of GaAs diode sources are not yet within the current state-of-the-art.

The use of  $N$  separate beams appears to be the best approach. However, in order to keep from blurring the image and from smoothing the three-dimensional surface, it is necessary to separate the reflected energy from each ground resolution cell, or pixel. Hence, coding the modulation of the  $N$  laser beams is necessary.

In order to gain the full advantage of the multiple source system, the  $N$  transmitter-receiver pairs (or channels) must not interfere with each other. Interpixel or interchannel isolation may be achieved by making the transmitter-receiver pair fields-of-view (FOV) spatially orthogonal, i.e., the pixel subtended by the FOV of transmitter-receiver pair ' $m$ ' cannot overlap the FOV of transmitter-receiver pair ' $j$ '. Interchannel crosstalk may also be minimized by constraining adjacent source modulating signals,  $s_m(t)$  and  $s_j(t)$ , to be temporally orthogonal, i.e., have zero cross-correlation. It will be shown that the optimum spatial-temporal coding combination utilizes both spatially and temporally orthogonal signals.

In the sections to follow, a brief summary of the statistical model for optical detectors which operate in the quantum limited regime is presented. This model is then used to obtain near-optimum estimators (post detection processors) of both pixel reflectivity and

slant range from the aircraft. The Cramer-Rao bound is included as an indication of estimation performance for the various modulation candidates. A number of laser modulation formats are presented and their relative performance compared.

### System Model

This section develops the mathematical tools necessary to compare the performance of the various laser modulation formats. To begin with, a noise model based upon the Poisson point process behavior of a direct (optical intensity) detector is developed. Estimation theory, based upon the Poisson statistics of the detector, is then used to develop the maximum-likelihood processor for both range and reflectance. In the final part of this section, performance expressions are developed to relate the variance of the range and the reflectance estimates, and other performance criterion, to the laser line scan system parameters.

Optical Detector Statistical Model. Due to the uncertainty in photon arrival times, the quantum nature of the photoelectron generation process, and the random nature of background noise and dark current, the output of an optical detector is a stochastic process. Conditioned on knowing the signal component of the complex envelope of the incident optical field, the detector output is conditionally an inhomogeneous filtered Poisson point process with the rate function [1],

$$\lambda(t) = \beta \int_A |U_s(\vec{r}, t)|^2 d\vec{r} + \beta \int_A E[|U_b(\vec{r}, t)|^2] d\vec{r} + \lambda_D \quad (1)$$

where:

- $\beta$  = average number of electrons generated per unit of incident optical energy
- $A$  = detector area
- $U_s$  = complex envelope of the incident electromagnetic field due to a known optical signal
- $U_b$  = complex envelope of the electromagnetic background noise field
- $\lambda_D$  = dark current rate function
- $E$  = expected value (ensemble average) operator

It is well known that the probability of detecting  $m$  photons in the time interval  $[0, T]$ , that is  $N(T) = m$ , is given by

$$P[N(T) = m] = \frac{(\mu)^m}{m!} e^{-\mu}; m = 0, 1, 2, \dots$$

where

$$\mu = \int_0^T \lambda(\alpha) d\alpha$$

In addition, conditioned on knowing  $U_s$ , the joint probability density of the ordered event times  $\{t_i\}$  and the number of events  $N(T)$  in an interval  $[0, T]$  is given by,

$$\begin{aligned} f_{\{t_i\}, N(T) | U_s} [\{t_i\}, N(T) = m | U_s] \\ = e^{-\mu} \prod_{i=1}^m \lambda(t_i) \end{aligned} \quad (2)$$

This is a complete statistical characterization of the photo-detector output. The joint probability density function (pdf) given in Eq (2) will be the basis for the parameter estimation which follows.

**Parameter Estimation.** The principle behind the measurement of range and reflectance by the laser line scan system is very similar to that of a classical radar. As with a radar, the time delay (or phase difference) between a transmitted signal and its return is proportional to the target range. In addition, the return signal amplitude is proportional to the target reflectance.

All measurements of the actual values of the delay  $\tau$  and the reflectance  $\rho$  will be degraded by system noise, and thus will only be estimates of the true values. These estimates, denoted  $\hat{\tau}$  and  $\hat{\rho}$ , are based upon the measurements made. In the case of well designed optical detector, the observations are the ordered event times  $\{t_i\}$  of detector output and the number of events  $N(T)$  in an interval  $[0, T]$ . The desire is to use statistical tools available to derive a signal processor such that  $E[\hat{\tau}] = \tau$  (the estimate has zero bias) and  $\text{var} [\tau - \hat{\tau}]$  (a measure of how close the estimate  $\hat{\tau}$  is to the real value  $\tau$ ) is small, with similar expressions for  $\hat{\rho}$  and  $\rho$ . Since no a priori information about the random parameters  $\tau$  and  $\rho$  is known, maximum likelihood (ML) estimation is used.

Given the observation  $Z$ , the ML estimate of the random parameter  $A$ , is defined by

$$\begin{array}{l} \text{Maximize} \\ \text{by Choice} \\ \text{of } A \end{array} \left[ \ln f_{Z|A}(Z|A) \right]_{A=\hat{a}_{ML}(Z)} \quad (3)$$

[2,p.6] where  $f_{Z|A}(Z|A)$  is the conditional pdf of the observation  $Z$ , conditioned on knowing the parameter  $A$ . For convenience, the subscripts will be dropped from the traditional notation for pdf's and  $N_T$  will be used to represent  $N(T) = m$ . From Eq (3) it follows that a sufficient, though not necessary, condition for the ML estimate can be found from

$$\frac{\partial \ln[f(Z|A)]}{\partial A} \bigg|_{A=\hat{a}_{ML}(Z)} = 0 \quad (4)$$

If the signal dependent portion of Eq (1) is replaced by  $\rho s(t)$  and the remaining portion is replaced by  $\lambda_n$ , then Eq (1) becomes

$$\lambda(t) = \rho s(t) + \lambda_n \quad (5)$$

where  $s(t)$  is a function of the intensity modulation impressed upon the transmitted laser beam. The simultaneous estimators  $\hat{\tau}$  and  $\hat{\rho}$  may be found by substituting Eqs (2) and (5) into the simultaneous equations

$$\frac{\partial \ln[f(\{t_i\}, N_T | \tau, \rho)]}{\partial \tau} \bigg|_{\tau=\hat{\tau}} = 0 \quad (6)$$

$$\frac{\partial \ln[f(\{t_i\}, N_T | \tau, \rho)]}{\partial \rho} \bigg|_{\rho=\hat{\rho}} = 0 \quad (7)$$

Unhappily, the simultaneous solutions of Eqs (6) and (7) are inseparable and there is no solution for  $\hat{\tau}$  independent of  $\hat{\rho}$  and visa-versa [3,pp.14-15].

However, substituting Eqs (2) and (5) into Eq (3) yields

$$\begin{aligned} \text{Maximize} \quad & \left[ \ln[f(\{t_i\}, N_T | \tau, \rho)] = \right. \\ \text{on } \tau, \rho \quad & \sum_{i=1}^m \ln[\rho s(t_i - \tau) + \lambda_n] \\ & \left. - \int_0^T [\rho s(\alpha - \tau) + \lambda_n] d\alpha \right] \end{aligned} \quad (8)$$

The general form of Eq (8) is that of a correlator [3, pp. 15-16] and may be realized approximately by a  $m \times n$  bank of correlators (Fig 1). The "biggest picker" picks the output of the correlator with the largest amplitude, and the  $\rho_i$  and  $\tau_i$  that corresponds to that correlator are the estimates  $\hat{\rho}$  and  $\hat{\tau}$  respectively. The correlator realization shown in Fig. 1 requires  $m \times n$  correlators and is not practical to implement.

It can be shown that in the case of a background noise limited detector, Eq (8) may be approximated by

$$\begin{aligned} \text{Maximize} \quad & \left[ \int_0^T \frac{\rho}{q\lambda_n} i(t)s(t)dt - \int_0^T \rho s(\alpha - \tau) d\alpha \right] \\ \text{on } \rho, \tau \quad & \end{aligned} \quad (9)$$

where  $q$  is the charge of an electron and  $i(t)$  is the output current of the photodetector. The first term in Eq (9) describes a correlator. If the observation interval  $[0, T]$  is much greater than the largest expected delay  $\tau$ , i.e., if end effects can be ignored, then the last term in the brackets may be ignored. Thus in that case the detector current  $i(t)$  is correlated with a linear function of  $s(t)$ , as in familiar radar applications. It can be shown that correlators and matched filters are equivalent methods for synthesizing the same ML estimator [4: pp. 315-317]. An alternate implementation, typically used with sinusoidal signals, is accomplished with a closed-loop estimator known as a phase-locked-loop (PLL).

A practical (suboptimum) estimator realization is shown in Fig. 2. The delay between the transmission of the signal and the occurrence of the peak is equal to  $\hat{\tau}$ . The amplitude of the peak detector output, given the delay estimate  $\hat{\tau}$ , is proportional to the reflectance estimate  $\hat{\rho}$  (this is a suboptimum estimate of  $\hat{\rho}$  because of the requirement for knowing  $\hat{\tau}$ ).

Note that, in general, the detector output is not correlated with  $s(t)$ , as would be done in a conventional radar, but instead is correlated

with the weighted natural log of  $\rho s(t) + \lambda_n$ . Thus it must be stressed that classical radar techniques do not always apply to optical systems involving direct (power) detection. Only in the background noise limited case, or when the signal rate function is so large that the Poisson statistics become Gaussian, may the familiar radar ML estimator, a matched filter, be used optimally.

Performance Evaluation. It was stated earlier that it is desirable that  $\text{var} [\tau - \hat{\tau}]$  and  $\text{var} [\rho - \hat{\rho}]$  be small. These variances are very difficult to compute in general; therefore, a lower bound for the variances will be computed using the Cramer-Rao (CR) lower bound. The CR lower bound for the variances of the estimator errors for  $\tau$  and  $\rho$  may be shown to be,

$$\sigma_{\tau}^2 \geq - E \left[ \frac{\partial^2 \ln f(\{t_i\}, N_T | \tau, \rho)}{\partial \tau^2} \right] = \left[ \int_0^T \frac{\rho^2 \dot{s}^2(t-\tau)}{\rho s(t-\tau) + \lambda_n} dt \right]^{-1} \quad (10)$$

$$\sigma_{\rho}^2 \geq - E \left[ \frac{\partial^2 \ln f(\{t_i\}, N_T | \tau, \rho)}{\partial \rho^2} \right] = \left[ \int_0^T \frac{s^2(t-\tau)}{\rho s(t-\tau) + \lambda_n} dt \right]^{-1} \quad (11)$$

[3:pp. 19-20]. Now let the energy,  $E_s$ , contained in the signal  $s(t)$  and the mean square bandwidth,  $B_s^2$ , of  $s(t)$  be defined as

$$E_s = \int_0^T s^2(t) dt \quad (12)$$

$$B_s^2 = \frac{\int_{-\infty}^{\infty} \omega^2 S(\omega) d\omega}{\int_{-\infty}^{\infty} S(\omega) d\omega} \quad (13)$$

where  $S(\omega)$  is the power spectral density of  $s(t)$ . For the background noise limited case, i.e.,  $\lambda \gg \rho s(t)$ , substituting Eqs (12) and (13) into Eqs (10) and (11) and simplifying yields

$$\sigma_{\tau}^2 \geq \frac{\lambda_n}{\rho^2 E_{S-BPF} B_s^2} \quad (14)$$

$$\sigma_{\rho}^2 \geq \frac{\lambda_n}{E_s} \quad (15)$$

where the subscript BPF denotes "bandpass filtered," i.e., the DC signal component has been removed.

Eqs (14) and (15) are the primary equations used to compare the various spatial and temporal coding combinations in the next section of this paper. For each different spatial-temporal coding scheme, the apparent signal energy and mean square bandwidth is calculated and substituted into Eqs (14) and (15). The exception is, again, purely sinusoidal modulation. In that case,  $s(t) = \frac{B_P d}{2} [1 + \sin(2\pi f_m t)]$  is substituted directly into Eqs (10) and (11) to obtain bounds on  $\sigma_{\tau}^2$  and  $\sigma_{\rho}^2$ . The modulation format with the lowest  $\sigma_{\tau}^2$  and  $\sigma_{\rho}^2$  is designated the optimum modulation from an estimation accuracy point of view. It should be emphasized that the CR lower bound is an optimistic performance measure and may not be achievable in practice. It indicates that, regardless of how good the signal processor, the smallest error possible occurs when Eqs (14) and (15) are achieved with equality. Such a processor is called an efficient estimator. Any suboptimum process will result in error variances larger than the lowest limits given by Eqs (14) and (15).

Another important performance measure is maximum unambiguous range. As stated earlier, the range is derived from the delay estimate. The relationship between range and delay is expressed by  $r = c\tau/2$  where  $c$  is the speed of light. However, since the transmitted signal is periodic with period  $T$ , a signal return for  $s(t-\tau)$  looks just like a return for  $s(t-(\tau+nT))$  where  $n$  is an integer. This implies  $r = c(\tau \text{ modulo } T)/2$ . Thus the maximum unambiguous range that may be measured is given by  $R_{amb} = cT/2$ . It is highly desirable that  $R_{amb}$  is greater than the largest terrain deviation or target height to be measured; this criteria as well as estimation accuracy is used to choose desirable modulation formats.

## Spatial and Temporal Coding Analysis

The performance of the various spatial-temporal coding combinations are expressed in terms of common constraints. It is assumed that, unless so stated, the transmitter and receiver FOVs are matched, i.e., subtend the same ground area (a pixel) and are spatially orthogonal from channel to channel. The number of pixels per scan line and the pixel size are fixed. The beam is modeled as moving discretely from pixel-to-pixel with no spatial filtering. All dwell times are expressed in terms of that for a single source laser line scan system,  $\tau_d$ . The total number of sources will be  $N$ , regardless of the spatial configuration. Noise considerations are limited to background noise and noise associated with the direct detection process. Ideal optics and atmosphere are assumed. And, of most importance, the power incident upon the detector,  $P_d$ , is assumed to be a constant, regardless of the imposed intensity modulation. Finally, the signal processor is always assumed to be the appropriate ML estimator as discussed earlier.

Many combinations of temporal and spatial codes were analyzed and are reported in [3]. The major temporal intensity codes included continuous wave (CW) modulation, sinusoidal modulation, pulse code modulation (PCM), and On-Off-Keyed (OOK) modulation (Fig. 3). As shown in Fig. 3, PCM modulation is merely intensity modulation with a particular pattern of on-off pulses, each of width  $t_o$ . The pulse pattern was chosen for its desirable autocorrelation and crosscorrelation properties; one such well-known pattern is the pseudo-noise (PN) sequence. Finally, OOK modulation is the combination of sinusoidal and PCM modulations, i.e., the envelope of the sinusoid is a PCM pulse sequence. The advantages of each is discussed in a later paragraph.

The spatial codes or scan configurations included staring (non-scanning) systems, serially scanned multiple beams, multiple beams scanned in parallel, overlapping scanning beams, and a staring receiver/scanning multiple sources system. All of the logical spatial-temporal combinations possible with the above codes are too numerous to be reported in this paper. For the sake of brevity, only the four most promising combinations are discussed here.

The four most promising spatial-temporal coding combinations are: (1) Parallel Scan, Sinusoidal Modulation, (2) Parallel Scan, OOK Sinusoidal Modulation, (3) Serial Scan, PCM, and (4) Overlapping Beams, PCM. The first two spatial-temporal coding configurations employ multiple sources scanned in parallel (Fig 4). By scanning  $N$  lines at once, the scan rate may be reduced by a factor of  $N^{-1}$ , thereby increasing the dwell time, and consequently, the reflected energy per pixel by a factor of  $N$ . The third coding configuration employs serially scanned multiple sources (Fig 5). By combining the output of the  $N$  matched filters via a delay line, the effect is the same as looking at a given pixel  $N$  times, thereby



increasing the effective energy reflected by that pixel by a factor of  $N$ . An advantage of the serial scan scheme is that any differences in transmitter-receiver pair responsivities are averaged out by the integrating process. The last coding configuration utilizes  $N$  scanning, broadly overlapping transmit beams partitioned by  $N$  scanning receiver (Fig 6). Once again the effect is to raise to energy reflected per pixel by  $N$ . This scheme also has the advantage of averaging out any differences in the  $N$  transmitter powers as well as alleviating the problem of collimating the relatively broadly diverging GaAs laser beams.

The root mean square (rms) errors of the above systems are compared in Table 1. For each coding scheme,  $E_s$ ,  $E_{s-BPF}$ , and  $B_s^2$  were calculated in terms of the common system parameters. Then, in order to facilitate the system comparisons, the rms range and reflectance performance for each system is expressed in terms of that of the system with the smallest mean square error. The smallest mean square range error occurred for the Parallel Scan, Sinusoidal Modulation case and is given by

$$\sigma_{r-s}^2 \geq \frac{1}{N} \cdot \frac{c^2 \lambda_n}{2\pi^2 f_m^2 \rho^2 \beta^2 p_d^2 \tau_d} \quad (16)$$

where  $c$  is the speed of light,  $f_m$  is the sinusoidal intensity modulation frequency, and  $P_d$  is the signal power incident upon the detector. The smallest mean square reflectance error occurred for the two schemes employing PCM, and is given by

$$\sigma_{\rho-PCM}^2 \geq \frac{1}{N} \cdot \frac{2\lambda_n}{\beta^2 p_d^2 \tau_d} \quad (17)$$

There are several important observations which should be made about the results tabulated in Table 1. First, note that in order for the rms range error for the PCM systems to be lower than that for the sinusoidally modulated system, the PCM pulse width  $t_o$  (Fig 3) must be shorter than the period of  $f_m$ . Thus for a fixed system bandwidth (determined either by detector or laser modulation limitations), the sinusoidal system achieves a finer range accuracy. However, the rms range error and maximum unambiguous range are both inversely proportional to the intensity modulation frequency  $f_m$ . Thus range error performance and unambiguous range are direct trade-offs.

A compromise exists in the OOK technique. The same sinusoidal intensity modulation as used above is coherently keyed on and off by a PCM code. The sinusoidal modulation inside of each burst or envelope may be used for fine grain range measurement, and the PCM envelope may

be used for coarse long range measurement. A small price is paid in range error performance, i.e.,  $\sigma_r$  is increased by  $\sqrt{2}$ , but the unambiguous range capability is significantly increased. There is also a similar degradation of  $\sigma_p$ , but the system will probably be capable of imaging well after the signal-to-noise ratio is too low to make range estimates, so this is not thought to be a serious degradation.

The OOK modulation (and PCM) has one other significant advantage over the sinusoidal modulation. By choosing the proper PCM modulation for each source, all adjacent channels may be made temporally orthogonal as well as spatially orthogonal, thereby assuring that the pixel-to-pixel cross-talk will be an absolute minimum.

### Conclusions

It has been shown that, based upon the quantum statistics of a background noise limited direct detector, the optimum estimator for delay (or range) is a correlator, and a suboptimum estimator for reflectance is an amplitude measurement, given the delay. The best possible range performance is achieved using multiple sources scanned in parallel and sinusoidally intensity modulated. However, if a large unambiguous range capability is important, a good compromise is a system using multiple sources scanned in parallel and intensity modulated by a PCM On-Off-Keyed sinusoid. This modulation format also gives an additional advantage of using PCM pulse sequences for adjacent channels so that they are temporally as well as spatially orthogonal.

### References

1. Hoversten, E. V., "Optical Communication Theory" in Laser Handbook edited by F. T. Arecchi and E. O. Schulz-DuBois. Amsterdam, The Netherlands: North-Holland, 1972.
2. Van Trees, Harry L., Detection, Estimation, and Modulation Theory, Part I: New York: John Wiley & Sons, Inc., 1968.
3. Shinkle, Reese S., Spatial and Temporal Coding of GaAs Lasers for a Laser Line Scan Sensor. Unpublished thesis, Wright-Patterson Air Force Base, Ohio: Air Force Institute of Technology, December 1977.
4. Ziemer, R. E. and W. H. Tranter. Principles of Communications. Boston: Houghton Mifflin Company, 1976.

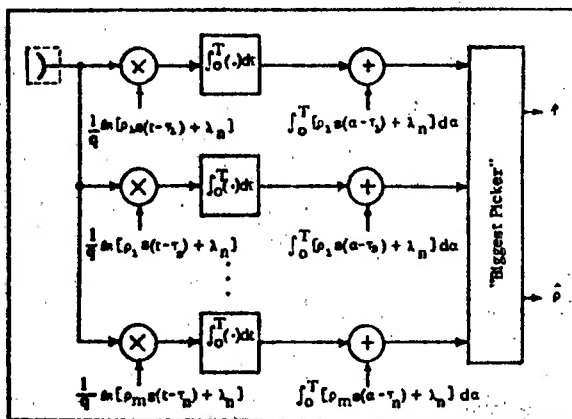


Figure 1  $m \times n$  Bank of Correlators Implementation of ML Estimators

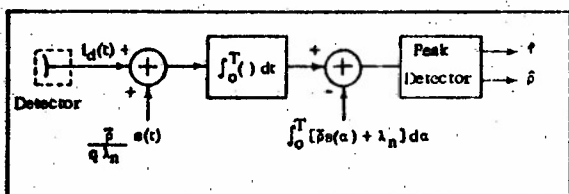


Figure 2 Suboptimum ML Estimators

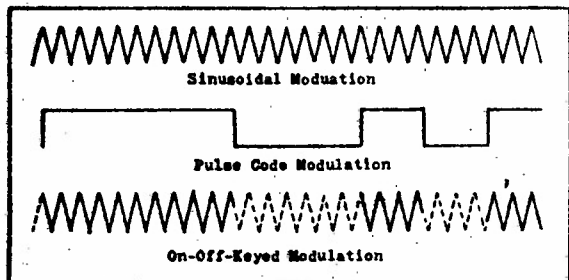


Figure 3 Primary Intensity Modulation Codes

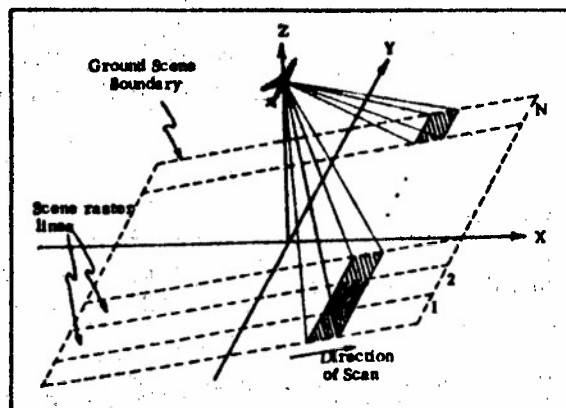


Figure 4  $N$  Sources in Parallel

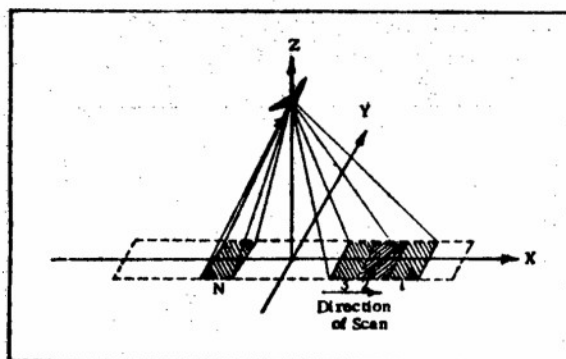


Figure 5  $N$  Sources in Series

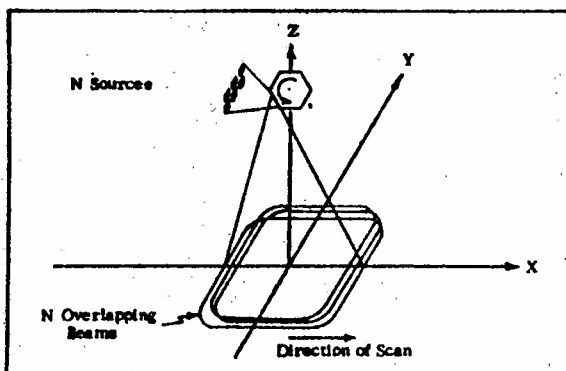


Figure 6  $N$  Overlapping Transmitted Laser Beams

Table I  
Spatial-Temporal Systems Characteristics

System	$\sigma_r$	$\sigma_\rho$	Range Ambiguity Interval	Optics Complexity
Serial Scan, PCM	$\frac{\pi}{2} f_m t_o \sigma_{r-s}$	$\sigma_{\rho-PCM}$	$c\tau_d/2$	
Overlapping Beams, PCM	$\frac{\pi}{2} f_m t_o \sigma_{r-S}$	$\sigma_{\rho-PCM}$	$c\tau_d/2$	Least
Parallel Scan, Single Sinusoidal Modulation	$\sigma_{r-S}$	$1.15\sigma_{\rho-PCM}$	$c/2f_m$	Severe
Parallel Scan, OOK Sinusoidal Modulation	$\sqrt{2} \sigma_{r-s}$	$1.63\sigma_{\rho-PCM}$	$c\tau_d/2$	

### Biographical Sketch

Captain Reese Shinkle was born on 11 October 1948 in Huntsville, Alabama. He graduated from high school as class valedictorian in 1967. He attended Auburn University and participated in the cooperative education program with NASA, George C. Marshall Space Flight Center, Huntsville, Alabama. While working for NASA he worked with analog and digital signal processing for both communications and radar systems, GaAs laser rangefinders, and fiber optic data links. Upon graduation from Auburn (high honors) with the degree of Bachelor of Electrical Engineering in December 1972, he received a commission in the USAF through the AFROTC program. His first assignment was to the 544th Aerospace Reconnaissance Wing, Headquarters, Strategic Air Command, Offutt AFB, Nebraska, where he served as an electronic intelligence and radar analyst. He entered the School of Engineering, Air Force Institute of Technology, in June 1976 and earned a Masters degree in the electro-optics program. Upon graduation from AFIT, he was assigned to the Laser/Electro-Optical Branch, Directorate of Avionics Engineering, Aeronautical Systems Division, Wright-Patterson AFB, Ohio. He is presently working on various electro-optical programs for reconnaissance, target cueing and obstacle avoidance. He is a member of the Institute of Electrical and Electronics Engineers, Eta Kappa Nu, Tau Beta Pi, and Phi Kappa Phi.